Design and Analysis of Beamforming in mmWave Networks

by

Wen Wu

A thesis
presented to the University of Waterloo
in fulfillment of the
thesis requirement for the degree of
Doctor of Philosophy
in
Electrical and Computer Engineering

Waterloo, Ontario, Canada, 2019

Author's Declaration

I hereby declare that I am the sole author of this thesis. This is a true copy of the thesis, including any required final revisions, as accepted by my examiners.

I understand that my thesis may be made electronically available to the public.

Abstract

To support increasing data-intensive wireless applications, millimeter-wave (mmWave) communication emerges as the most promising wireless technology that offers high data rate connections by exploiting a large swath of spectrum. Beamforming (BF) that focuses the radio frequency power in a narrow direction, is adopted in mmWave communication to overcome the hostile path loss. However, the distinct *high directionality* feature caused by BF poses new challenges: 1) *Beam alignment (BA) latency* which is a processing delay that both the transmitter and the receiver align their beams to establish a reliable link. Existing BA methods incur significant BA latency on the order of seconds for a large number of beams; 2) *Medium access control (MAC) degradation*. To coordinate the BF training for multiple users, 802.11ad standard specifies a new MAC protocol in which all the users contend for BF training resources in a distributed manner. Due to the "deafness" problem caused by directional transmission, i.e., a user may not sense the transmission of other users, severe collisions occur in high user density scenarios, which significantly degrades the MAC performance; and 3) *Backhaul congestion*. All the base stations (BSs) in mmWave dense networks are connected to backbone network via backhaul links, in order to access remote content servers. Although BF technology can increase the data rate of the fronthaul links between users and the BS, the congested backhaul link becomes a new bottleneck, since deploying unconstrained wired backhaul links in mmWave dense networks is infeasible due to high costs. In this dissertation, we address each challenge respectively by 1) proposing an efficient BA algorithm; 2) evaluating and enhancing the 802.11ad MAC performance; and 3) designing an effective backhaul alleviation scheme.

Firstly, we propose an efficient BA algorithm to reduce processing latency. The existing BA methods search the entire beam space to identify the optimal transmit-receive beam pair, which leads to significant latency. Thus, an efficient BA algorithm without searching the entire beam space is desired. Accordingly, a *learning-based BA algorithm*, namely hierarchical BA (HBA) algorithm is proposed which takes advantage of the *correlation structure* among beams such that the information from nearby beams is extracted to identify the optimal beam, instead of searching the entire beam space. Furthermore, the *prior knowledge* on the channel fluctuation is incorporated in the proposed algorithm to further accelerate the BA process. Theoretical analysis indicates that the proposed algorithm can effectively identify the optimal beam pair with low latency.

Secondly, we analyze and enhance the performance of BF training MAC (BFT-MAC) in 802.11ad. Existing analytical models for traditional omni-directional systems are unsuitable for BFT-MAC due to the distinct directional transmission feature in mmWave networks. Therefore, a thorough theoretical framework on BFT-MAC is necessary and

significant. To this end, we develop a simple yet accurate *analytical model* to evaluate the performance of BFT-MAC. Based on our analytical model, we derive the closed-form expressions of average successful BF training probability, the normalized throughput, and the BF training latency. Asymptotic analysis indicates that the maximum normalized throughput of BFT-MAC is barely $1/e$. Then, we propose an *enhancement scheme* which adaptively adjusts MAC parameters in tune with user density. The proposed scheme can effectively improve MAC performance in high user density scenarios.

Thirdly, to alleviate backhaul burden in mmWave dense networks, edge caching that proactively caches popular contents at the edge of mmWave networks, is employed. Since the cache resource of an individual BS can only store limited contents, this significantly throttles the caching performance. We propose a *cooperative edge caching policy*, namely device-to-device assisted cooperative edge caching (DCEC), to enlarge cached contents by jointly utilizing cache resources of adjacent users and BSs in proximity. In addition, the proposed caching policy brings an extra advantage that the high directional transmission in mmWave communications can naturally tackle the interference issue in the cooperative caching policy. We theoretically analyze the performance of DCEC scheme taking the network density, the practical directional antenna model and the stochastic information of network topology into consideration. Theoretical results demonstrate that the proposed policy can achieve higher performance in offloading the backhaul traffic and reducing the content retrieval delay, compared with the benchmark policy.

The research outcomes from the dissertation can provide insightful lights on understanding the fundamental performance of the mmWave networks from the perspectives of BA, MAC, and backhaul. The schemes developed in the dissertation should offer practical and efficient solutions to build and optimize the mmWave networks.

Acknowledgements

The past four years of my graduate and research life in Waterloo is truly the most unique, precious and awarding time of mine. Along this way, there are so many people who deserve to be thanked for their friendship, help and supports offered to me. Within this limited space, I cannot hope to thank them properly.

First and foremost, my deepest and sincerest gratitude goes to my supervisor Professor Xuemin Shen for his endless help in my Ph.D. study and life in University of Waterloo. His valuable instructions and patient guides in research, enthusiastic encouragements, and positive philosophy in life have offered me great help and benefits during my program, without which this thesis would not be possible. His enthusiasm and dedication to his work, his students and his family are really inspiring to me. The weekly group meetings coordinated by Professor Shen provided me an excellent opportunity to broaden my knowledge and improve my presentation skills. Professor Shen is and will always be the role model of mine.

I would also like to thank Professor Weihua Zhuang for her kindly support and help, which greatly benefits my research in this thesis. Her invaluable suggestions had significantly improved the quality of my collaborative research. The carefulness, and strong commitment that Professor Zhuang conveyed to me are exactly the essential qualities of an excellent researcher.

I would like to thank Professor Xiaodong Lin, Professor Sagar Naik, Professor Wei-Chau Xie, and Professor Xianbin Wang, for serving my thesis/oral defense committee. Their precious time and efforts devoted to this thesis are highly appreciated.

Doing research and spending day and night in the lab can be boring and daunting. My fellows have made my life at University of Waterloo a colorful and enjoyable experience. I am grateful for time spent with Dr. Qiang Ye, Dr. Jianbing Ni, Dr. Yujie Tang, Dr. Wenchao Xu, Dr. Feng Lyu, Dr. Yang Zhang and many others. I also wish to give my gratitude to Nan Chen, Junling Li, Weisen Shi, Haohao Liao, Ling Lyu, Jiayin Chen, Si Yan, Cheng Huang, Dongxiao Liu, Kaige Qu, Huaqing Wu, Haixia Peng, Meng Qin, Ruijin Sun, Omar Alhussein, Hesham Moussa, Yanpeng Dai, Fei Sun, Wenjuan Tang, Dr. Shan Zhang and Dr. Xiaohui Lin for their advice and help in the Ph.D. pursuit. In particular, I wish to especially thank Dr. Ning Zhang, Dr. Nan Cheng, Dr. Peng Yang, Along Jin, and Khalid Aldubaikhy for their inspiring discussions and invaluable suggestions on my research.

Thanks also go to the artificial intelligence subgroup members: Dr. Nan Cheng, Dr. Wei Wang, Hongli He, Conghao Zhou, Kangjia Lyu, Mushu Li and Liang Xue for their

help on establishing our research team in BBCR Lab. It was a wonderful experience to collaborate with Dr. Nan Cheng on a joint research and project.

Finally, I would like to thank my family for all their constant love, endless support, and encouragement throughout my life.

Wen Wu

July 26, 2019

Waterloo, Ontario, Canada

This PhD thesis is dedicated to my beloved parents, Qinglan Wan and Shuihua Wu.

Table of Contents

List of Tables

List of Figures

List of Abbreviations

5G	Fifth-Generation
A-BFT	Associated Beamforming Training
ADC	Analog-to-Digital Conversion
AOD	Angle of Departure
AOA	Angle of Arrival
AP	Access Point
AR	Augmented Reality
ATI	Announcement Transmission Interval
BF	Beamforming
BFT	Beamforming Training
BFT-MAC	Beamforming Training Medium Access Control
BI	Beacon Interval
BRP	Beam Refinement Protocol
BS	Base Station
BT	Beam Tracking
BTI	Beacon Transmission Interval
CMOS	Complementary Metal-Oxide-Semiconductor
COTS	Commercial-Off-The-Shelf
D2D	Device-to-Device
DAC	Digital-to-Analog Conversion
DCEC	Device-to-device assisted Cooperative Edge Caching
DCF	Distributed Coordinate Function
DFT	Discrete Fourier Transform
DSP	Digital Signal Processing

EIRP	Effective Isotropically Radiated Power
eMBB	Enhanced Mobile BroadBand
FCC	Federal Communications Commission
FWA	Fixed Wireless Access
HBA	Hierarchical Beam Alignment
HOO	Hierarchical Optimistic Optimization
IoT	Internet of Things
LOS	Line-Of-Sight
MAB	Multi-Armed Bandit
MAC	Medium Access Control
MEC	Mobile Edge Computing
MIMO	Multiple Input Multiple Output
mmWave	millimeter-wave
mMTC	Massive Machine Type Communications
MPC	Most Popular Caching
NLOS	Non-Line-Of-Sight
PDF	Probability distribution Function
PPP	Poisson Point Process
QoE	Quality of Experience
QoS	Quality of Service
RF	Radio Frequency
RSS	Received Signal Strength
SBS	Small Base Station
SINR	Signal-to-Interference-plus-Noise-Ratio
SLS	Sector Level Sweep
SNR	Signal-to-Noise Ratio
SSW	Sector Sweep
SSW-FB	Sector Sweep Feedback
STA	Station
TCP	Transmission Control Protocol
TDMA	Time Division Multiple Access
UCB	Upper Confidence Bound
UDN	Ultra Dense Network

URLLC	Ultra Reliable Low Latency Communication
VR	Virtual Reality
WLAN	Wireless Local Area Network
WPAN	Wireless Personal Area Network

Chapter 1

Introduction

1.1 mmWave Communications

Recent advanced technologies in consumer electronic devices and the surge of emerging data-intensive applications, such as panoramic video streaming, big data analytics, wireless fiber-to-home access, cordless virtual reality (VR) and augment reality (AR) gaming, provide people with ubiquitous high quality multimedia content. As reported, more than 15,000 VR headsets have been sold by HTC in ten minutes on its first release. A recent forecast shows that the worldwide shipment of AR/VR devices will reach 9 million in 2019 [1]. These data-intensive applications create a significant growth in data volume in wireless networks. It is predicted that the world monthly mobile data traffic will have a twelve-fold increase in the next five years [2]. Traditional wireless network that operates in microwave bands (below 6 GHz), faces a severe spectrum scarcity issue, especially at peak hours, which cannot satisfy the surging demand of mobile data traffic. In addition, to cater for these data-intensive applications (e.g., high quality VR/AR), wireless network needs to deliver a multiple gigabit data rate [3], which is also beyond the capability of traditional wireless networks even utilizing high spectrum efficiency techniques. Thus, more spectrum is needed in the next generation wireless network.

To obtain more spectrum, higher frequency band communication has recently garnered attention from both academia and industry. Particularly, the communications at 30-300 GHz band where wavelength is 1-10 mm, often referred to as millimeter-wave (mmWave) communications, possesses a large swath of spectrum. mmWave frequency bands can offer more than 20 GHz spectrum, which is 20 times more than that allocated to current WiFi and cellular systems. By utilizing the large chunks of bandwidth, the mmWave

communication solution can provide a multiple gigabit data rate and is expected to be the key evolution of the next generation wireless network.

Owing to the high data rate, mmWave communications can support numerous potential data-hungry applications. One important use case is to support infotainment applications and enhance the quality of experience (QoE) of mobile users. For example, mobile users can enjoy high quality VR/AR gaming, or watch real-time ultra high definition videos through mmWave communications. On the other hand, from the perspective of network operators, mmWave is an enabling technology for wireless backhaul in ultra-dense networks (UDNs) or emerging drone networks. To provide reliable performance in UDNs, backhaul links should deliver a data rate of 1-10 Gbit/s [4]. Considering the expensive deployment cost of high-rate backhaul links, mmWave communication is an efficient yet cost-effective solution for network operators in UDNs. Similarly, drone networks also consider the mmWave communication as the underlying wireless backhaul technology. In addition to the wireless backhaul application, mmWave communications can also be applied to solve the last mile fiber replacement problem. Recently, fixed wireless access (FWA) seems to be a plausible solution which utilizes mmWave technology to provide broadband Internet access to customers, instead of deploying the costly and time-consuming fiber networks [5]. To summarize, the mmWave communication can make the next generation wireless network more efficient and cost-effective while satisfying the surging demand of data traffic.

The earliest concept of mmWave communication can be traced back to over one hundred years ago. Bose has conducted the first mmWave experiment with a wavelength of 5 mm in 1897 [6]. However, in the following century, mmWave technology was deemed unsuitable for mobile communications due to the following reasons. Firstly, the propagation at the mmWave band suffers from significant path loss as compared to that at the microwave band. Secondly, mmWave channel is relatively sparse due to weak reflection characteristics, which limits the coverage of mmWave networks. Lastly, the signal propagation at the mmWave band is extremely sensitive to blockage since mmWave signals suffer from huge penetration loss due to a short signal wavelength. These hostile propagation characteristics significantly hinder the development of mmWave communications.

Nowadays, mmWave communication is no longer conceptual due to the recent progress of hardware circuit, communication and signal processing technology. To compensate the path loss, a large number of antennas (more than 32) are packed into an antenna array of a compact size due to the advanced low-power complementary metal-oxide-semiconductor (CMOS) radio-frequency (RF) circuits technology and the small wavelength of mmWave signal. These small and energy-efficient antenna arrays can be fabricated in a small chip, which facilitate light-weight and long-life mmWave devices. The large-scale antenna array can be used to provide high directional antenna gain, which is the beamforming (BF)

technology. In specific, BF acts as a "focusing lens", which focuses RF energy towards a narrow direction to enhance the signal-to-noise ratio (SNR) of mmWave signals. For example, an antenna array with 32 elements can provide about a 15 dB directional antenna gain. The antenna array at BS can be equipped with an even larger scale (e.g., 256-antenna array) to provide more antenna gain. Thus, the obstacle of the path loss in mmWave communications is surmountable with proper BF technology.

The academia, industry and government institutions have initiated numerous activities in the area of mmWave communications. Firstly, the academia has devoted extensive research efforts in analyzing the performance of mmWave networks [7], designing novel efficient BF techniques [8] [9], and enhancing the performance from the physical layer and medium access control (MAC) layer [10]. Secondly, the industry has performed extensive measurement campaigns to evaluate the effectiveness of the proposed mmWave communication schemes from academia under different scenarios. In addition, to have a better understanding of propagation characteristics, numerous channel measurements are conducted by standard bodies, such as 3GPP and WiFi Alliance. Thirdly, government mandate has put the mmWave communications on the fast track. European union (EU) has initiated multiple projects, such as "MiWEBA"[1], "MiWaves"[2] and "mmMAGIC"[3], which focus on applying mmWave communications in mobile networks and high data rate wireless backhaul. Not surprisingly, Chinese governments have also supported a few projects on mobile mmWave networks and the design of RF chips.

Multiple standardization efforts and commercial-off-the-shelf (COTS) products further pave the road for commercialization of mmWave communications. At the unlicensed 60 GHz band, multiple standards have been specified for diverse applications in recent years, including WirelessHD for video area networks, IEEE 802.11ad [11] (refers to 802.11ad for short hereinafter) for wireless local area networks (WLANs), IEEE 802.15.3c [12] and ECMA-387 for wireless personal area networks (WPAN). As 802.11ad builds on the existing strong market presence of WiFi at 2.4/5 GHz bands, 802.11ad takes significant advantage over other standards, which leads to a booming market on mmWave WLAN. On the other hand, at licensed mmWave bands, mmWave technology is deemed as the most promising technology for the enhanced mobile broadBand (eMBB) use case in the 5G paradigm. Thus, the 3GPP working group has standardized mmWave communication as a 5G new radio interface.

[1]http://www.miweba.eu/
[2]http://www.miwaves.eu/
[3]https://5g-mmmagic.eu/

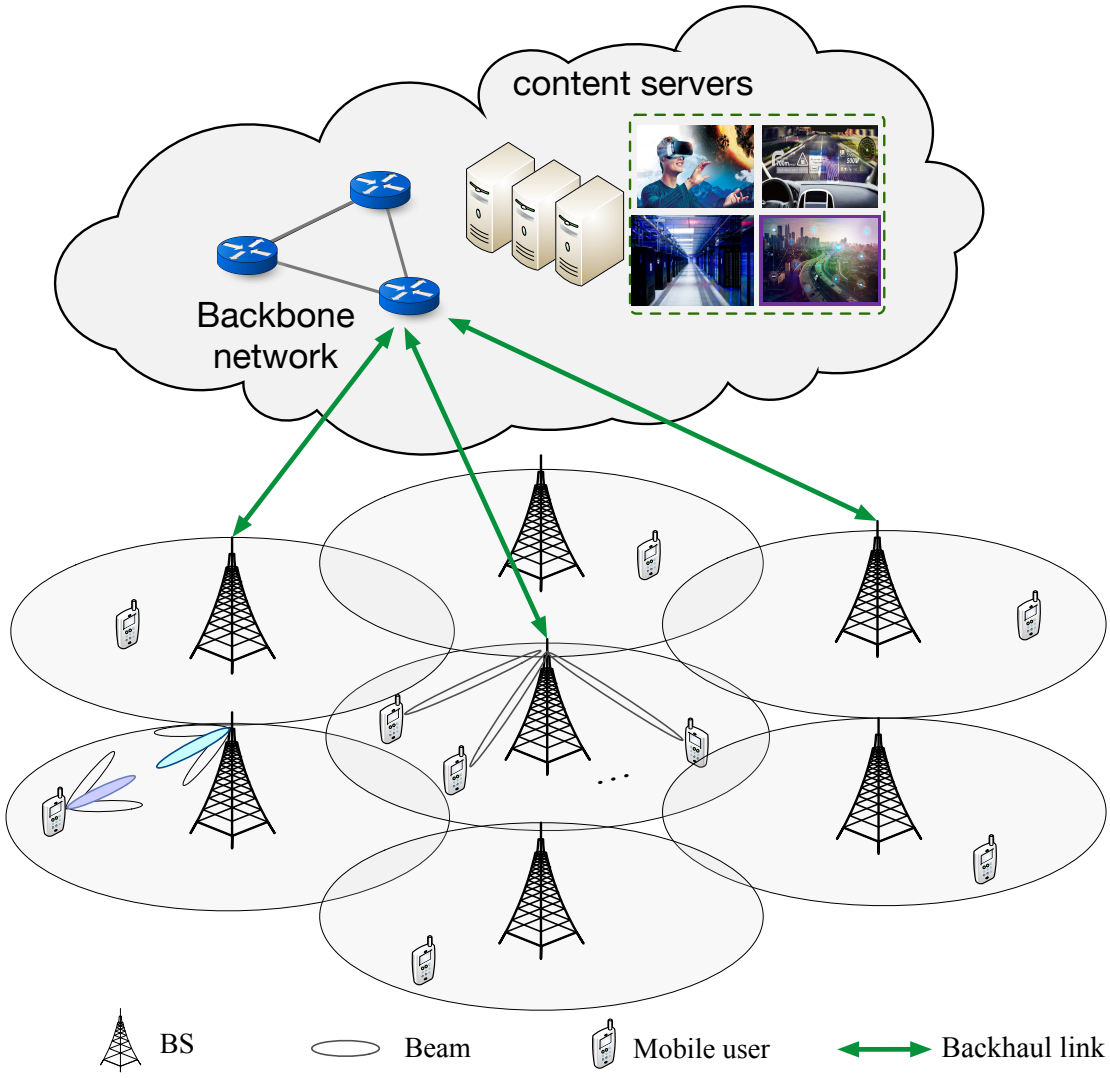

Fig. 1.1: The architecture of mmWave dense networks. All BSs connect to the backbone network via constrained backhaul links in order to access remote content servers.

1.2 Motivation and Research Challenges

mmWave communication has been received a myriad of research attentions, including the BF design and network performance analysis. While being seriously pursued, several fundamental and practical issues remain to be solved. In addition, previous researches

focus on the performance from physical layer's perspective, while ignoring the impacts of other communication layers, such as MAC layer and upper layer. In this dissertation, we target to an in-depth understanding of mmWave network. In particular, our goal is to develop practical and efficient schemes on communication layers to enhance mmWave network performance.

In mmWave systems, the distinct *high directionality* feature caused by BF technology leads to the following fundamental challenges in practice.

- BA latency. Since BF is endowed with the high directionality feature, both the transmitter and the receiver have to align their beams to establish a reliable communication link in the physical layer, i.e., BA or BF training[4]. For example, as shown in Fig. 1.1, each user needs to establish the communication link with the BS via the BA process. Slight beam misalignment can dramatically reduce the link budget and drop the throughput from multiple gigabit to a few hundred megabits [13]. Thus, BA is a key process to achieve high data rate transmission in mmWave communications. In specific, the goal of BA process is to identify the optimal transmit-receive beam pair among all possible beam combinations. However, existing BA methods, such as that in 802.11ad, need to search the entire beam space to identify the optimal transmit-receive beam pair, which incurs significant BA latency on the order of seconds for a large number of beams. Thus, an efficient BA algorithm without searching the entire beam space is required in practical mmWave communications.

- The MAC performance degradation in high user density scenarios. From the perspective of MAC layer, all the users need to perform BF training with the coordinator of the network (e.g., BS or access point (AP)) to access the mmWave network, as shown in Fig. 1.1. To coordinate BF training for multiple users in the mmWave network, 802.11ad specifies a distributed BF training MAC (BFT-MAC) protocol in which each user performs BF training in a contention and backoff manner. The high directionality feature of mmWave communications leads to a "deafness" problem that a user may not sense the transmission of other users, which results in severe transmission collisions in high user density scenarios. Thus, to configure MAC parameters to maximize the performance, the elaborate analysis of BFT-MAC is of paramount importance. Since the BFT-MAC protocol is different from traditional carrier sensing based MAC protocols, a new analytical model is desired. In addition,

[4]In our thesis, we use the terminology "BA" in the point-to-point communication scenario. The terminology "BF training" is used in the MAC layer analysis since "BF training" is adopted in the 802.11ad standard.

since the severe performance degradation occurs in high user density scenarios, how to enhance the MAC performance is imperative.

- Backhaul congestion in mmWave dense networks. Although the fronthaul links between users and the BS can be significantly enhanced via high directional mmWave communications, backhaul links between the BS and backbone networks, as shown in Fig. 1.1, are relatively constrained due to the prohibitive deployment cost of unconstrained wired backhaul links in mmWave dense networks. Thus, from the perspective of network deployment, the constrained backhaul links become new bottleneck of the entire mmWave networks. This backhaul congestion issue will further exacerbate the network performance with the densification of mmWave networks. Therefore, an effective solution to alleviate backhaul congestion is necessary for the practical deployment of mmWave dense networks.

1.3 Our Approach and Contributions

In this dissertation, we present our solutions to enhance the performance of mmWave networks by addressing the aforementioned challenges. We generally divide the enhanced design of mmWave networks into three research topics, i.e., BA algorithm design, MAC performance evaluation and enhancement, and backhaul alleviation scheme design, and address each topic in one chapter as follows.

1.3.1 Efficient BA Design

In the first topic, we develop an efficient BA algorithm to significantly reduce the BA latency, namely hierarchical beam alignment (HBA) algorithm. We first formulate the BA problem as a stochastic multi-armed bandit (MAB) problem with the objective of maximizing the cumulative received signal strength within a certain period. The proposed algorithm takes advantage of the correlation structure among beams such that the information from nearby beams is extracted to identify the optimal beam, instead of searching the entire beam space. Furthermore, the prior knowledge on the channel fluctuation is incorporated in the proposed algorithm to further accelerate the BA process. Theoretical analysis indicates that the proposed algorithm is asymptotically optimal. Extensive simulation results demonstrate that the proposed algorithm can identify the optimal beam with a high probability and reduce the BA latency from hundreds of milliseconds to a few milliseconds in the multipath channel, as compared to the existing BA method in 802.11ad.

Contributions: The main contributions of this research are four-fold. Firstly, we formulate the BA problem as a stochastic MAB problem, in which the objective is to sequentially select beams to maximize cumulative received signal strength (RSS) within a certain period. Secondly, we prove that the mean RSS function over the beam space follows a multimodality structure in the multipath channel, which characterizes the correlation structure among nearby beams. Thirdly, we propose a fast BA algorithm to accelerate beam search by exploiting the correlation structure and the prior knowledge on the channel fluctuation. Fourthly, we derive a sublinear analytical upper bound on the cumulative regret, which indicates that the proposed algorithm is asymptotically optimal.

1.3.2 MAC Performance Evaluation and Enhancement

In the second topic, we investigate the MAC performance of BF training in 802.11ad and then develop an enhancement scheme for high user density scenarios. In this thesis, we first develop a simple yet accurate analytical model to evaluate the performance of BFT-MAC protocol in 802.11ad. Our analytical model incorporates the user density in the modeling of BFT-MAC, which unveils the impact of user density and MAC parameters on the BFT-MAC performance. Based on our analytical model, we derive the closed-form expressions of average successful BF training probability, the normalized throughput, and the BF training latency. Particularly, asymptotic analysis indicates that the maximum normalized throughput of BFT-MAC is barely $1/e$, which is the same as that of slotted ALOHA. Moreover, the throughput greatly degrades in dense user scenarios due to the mismatch between the active users and the BF training resources. Then, we propose an enhancement scheme which adaptively adjusts the MAC parameters in tune with user density, to improve MAC performance in dense user scenarios. Extensive simulation results validate the accuracy of the developed analytical model and the effectiveness of the proposed enhancement scheme.

Contributions: The main contributions of this research are three-fold: 1) We propose an analytical model to evaluate the performance of BFT-MAC. Extensive simulation results validate the accuracy of the proposed analytical model; 2) We derive closed-form expressions of the successful BF training probability, the normalized throughput and average BF training latency based on the proposed analytical model. Asymptotic analysis indicates that the maximum normalized throughput is barely $1/e$; and 3) We propose an enhancement scheme which adjusts MAC parameters in tune with the user density to improve the MAC performance in high user density scenarios.

1.3.3 Backhaul Alleviation Scheme Design

In the third topic, we rely on the edge caching technology which proactive caches popular contents in the small base station (SBS), to alleviate the backhaul congestion in mmWave dense networks. However, constrained cache resource of individual SBSs significantly throttles the performance of edge caching. To address this issue, we propose a device-to-device (D2D) assisted cooperative edge caching (DCEC) policy for mmWave dense networks, which cooperatively utilizes the cache resource of users and SBSs in proximity. In the proposed DCEC policy, a content can be cached in either users' devices or SBSs according to the content popularity, and a user can retrieve the requested content from neighboring users via D2D links or the neighboring SBSs via cellular links to efficiently exploit the cache diversity. Unlike existing cooperative caching policies in the lower frequency bands that require complex interference management techniques to suppress interference, we take advantage of directional antenna in mmWave systems to ensure high transmission rate whereas mitigating interference footprint. Taking the practical directional antenna model and the network density into consideration, we derive closed-form expressions of the backhaul offloading performance and content retrieval delay based on the stochastic information of network topology. In addition, analytical results indicate that, with the increase of the network density, the content retrieval delay via D2D links increases significantly while that via cellular links increases slightly. Comprehensive simulations validate our theoretical analysis and demonstrate that the proposed policy can achieve higher performance in offloading the backhaul traffic and reducing the content retrieval delay compared with the state-of-the-art most popular caching (MPC) policy.

Contributions: The main contributions of this research are three-fold. Firstly, we derive closed-form expressions of the backhaul offloading gain and the content retrieval delay in mmWave dense networks based on stochastic information on network topology. Secondly, we analyze the impacts of the network density and practical directional antennas on caching performance respectively. Thirdly, we show the tradeoff relationship between transmission efficiency and caching diversity in mmWave dense networks.

1.4 Thesis Outline

The rest of this thesis is organized as follows: Chapter 2 presents a comprehensive overview of mmWave communications and the key enabling technologies. Chapter 3 investigates the BA problem and proposes a fast BA algorithm. Chapter 4 develops an analytical model to investigate the BFT-MAC performance. Based on the analytical model, the normalized

throughput and average BF training latency are analyzed. Chapter 5 develops and then analyzes the performance of DCEC policy, considering the impacts of the directional antenna and network density. Finally, Chapter 6 concludes the thesis, and points out the future research directions.

Chapter 2

Background

mmWave communication is considered as the most promising technology to increase data rate and reduce latency in the next generation wireless networks. This chapter first explains the different propagation characteristics at mmWave bands as compared to low-frequency microwave bands. Understanding these characteristics is necessary for the design of suitable signal processing algorithms and network protocols. After that, we introduce different BF technologies, including analog BF and hybrid BF, followed by the introduction of BF training protocol. Then, a comprehensive overview on the commercialization activities of mmWave communications is presented. Finally, the basics of MAB theory is provided to have a better understanding of the MAB problem.

2.1 Propagation Characteristics

The mmWave frequency band, which exists between 30-300 GHz, has attracted the attentions of both industry and academia due to vast amount of unexplored spectrum [14]. In specific, mmWave frequency within 30-100 GHz band occupies more than 20 GHz spectrum (including 1.4 GHz bandwidth at 39 GHz band, 2.1 GHz bandwidth at 37/42 GHz band, 7 GHz bandwidth at 60 GHz band and more than 10 GHz at E band[1], as shown in Fig. 2.1), which is 20 times more than that allocated to today's WiFi and cellular systems. In addition, if we turn to higher frequency bands (more than 100 GHz), there is more

[1]The frequency bands at 71-76 GHz, 81-86 GHz, and 92-95 GHz, collectively referred to as E band, are allocated for ultra-high-speed data communications by federal communications commission (FCC) in October 2003.

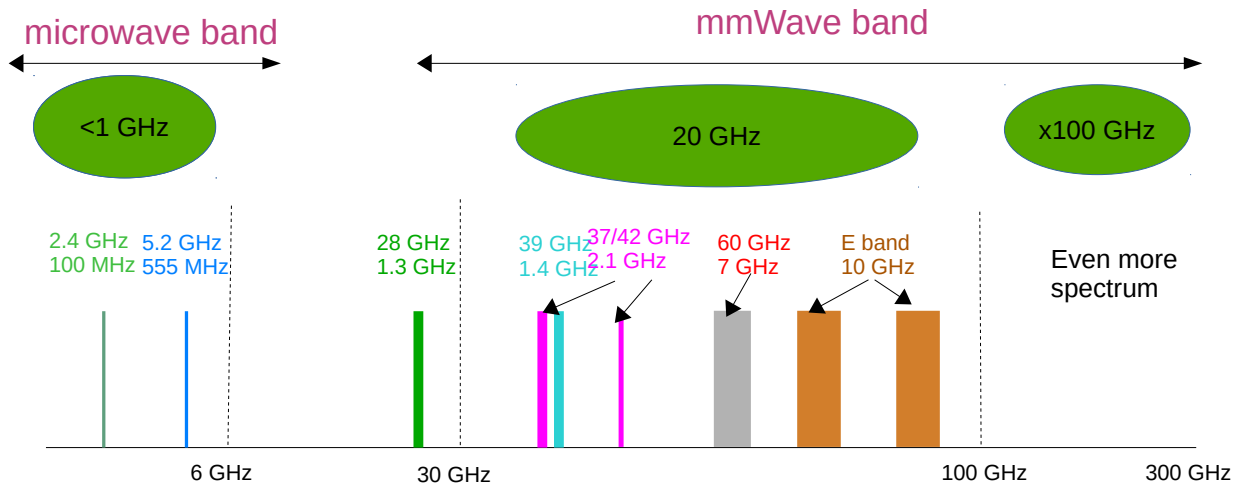

Fig. 2.1: The spectrum in mmWave frequency band.

than 100 GHz unlicensed bandwidth, which is expected to be utilized in the future wireless network (e.g., 6G cellular network).

To efficiently utilize mmWave frequency bands, the first and foremost is to have a better understanding of propagation characteristics in mmWave communications. Compared with the traditional microwave communication, mmWave communication has several unique propagation characteristics due to the small wavelength compared with most of the objects in the environment, including huge path loss, large penetration loss, channel sparsity and narrow beamwidth. These propagation characteristics pose new challenges for mmWave technology to support reliable communications. In the following, these unique propagation characteristics will be introduced in detail.

2.1.1 High Path Loss

In the free space transmission, the received power can be characterized by the celebrated Friis law formula [15], i.e.,

$$P_r = P_t G_t G_r \left(\frac{\lambda}{4\pi}\right)^2 r^{-n} \tag{2.1}$$

where P_t is the transmit power, r is the distance between the transmitter and the receiver, λ is the wavelength of carrier frequency, and n denotes the path loss exponent. Here, G_t and G_r represent the directional antenna gains of the transmitter and the receiver, respectively. Based on the equation, the received power depends on the wavelength of the

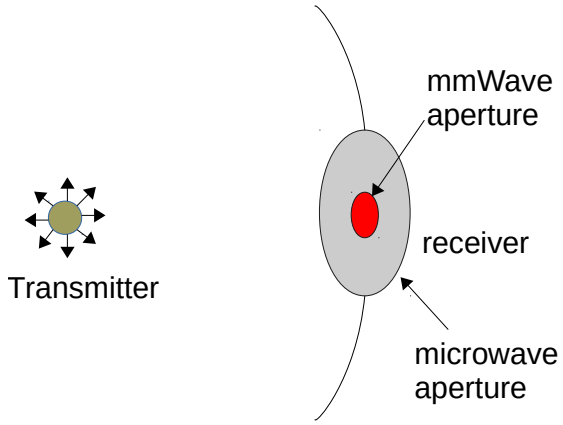

Fig. 2.2: Antenna aperture in mmWave communications. The mmWave antenna element captures less RF energy due to a smaller aperture size.

carrier frequency. Since the wavelength of mmWave signal is much smaller than that of the traditional microwave signal, the mmWave antenna element has a smaller aperture than the microwave antenna element so as to capture less RF power, as shown in Fig. 2.2. Thus, the path loss at mmWave bands is much higher than that at microwave bands. For example, 60 GHz mmWave systems suffer from 28 dB extra path loss compared with that in 2.4 GHz microwave systems based on the above equation. In addition, mmWave systems have a larger bandwidth than microwave systems, which results in higher noise power. For example, 60 GHz mmWave systems (e.g., 802.11ad) that occupy 2.16 GHz bandwidth give 17 dB extra noise power than 2.4 GHz microwave systems (e.g., 802.11n) that only occupy 40 MHz bandwidth. Taking path loss and noise power into consideration, mmWave systems suffer from severe SNR loss (up to 45 dB) compared with traditional microwave systems.

On the other hand, rain attenuation and atmospheric absorption also introduce extra path loss. Based on extensive measurements at 28 GHz band [16], the rain attenuation is around 7 dB/km in heavy rain scenarios, while the atmospheric absorption is about 1 dB/km. Thus, for long-distance mmWave communication (e.g., wireless backhaul application), rain attenuation and atmospheric absorption may exacerbate the path loss. However, for urban mobile scenarios in which the typical radius of mmWave networks is about a few hundred meters, rain attenuation and atmospheric absorption have limited impact on the system performance. Note that rain attenuation and atmospheric absorption vary with different frequency bands. For more details, one can refer to detailed in-field measurement results in [17].

Extensive efforts have been devoted to developing accurate and practical path loss models under various environments, especially at the highly potential bands (e.g., 28, 38, 60, and 82 GHz). Based on abundant measurement data, 3GPP provides new models in dynamic line-of-sight (LoS) and non-line-of-sight (NLoS) blockage. Other measurement campaigns are performed in some specific scenarios, such as airport, high-density stadium [18]. At the unlicensed 60 GHz band, 802.11 consortium performs extensive measurements, and the detailed path loss models in different scenarios can be found in [19].

2.1.2 Penetration Loss

Another salient characteristics of mmWave communication is the high penetration loss. Unlike WiFi signal, mmWave signal could not penetrate many objects since the wavelength of mmWave signal is much smaller than size of objects in the environment. For example, a brick can attenuate mmWave signals as much as 40-80 dB [20] [21]. Similarly, human body may result in an attenuation of 20-35 dB. Foliage also causes a significant penetration loss, which poses significant challenges for outdoor mmWave communications. Due to the high penetration loss, blockage emerges as a thorny issue in mmWave communications. Especially, there are several special blockage forms exist in mmWave communications. For example, hand blocking (mmWave signals are blocked by human hands) may occur with a high probability since phones or other potable digital devices are usually holding in human hands. Additionally, self-body blocking caused by the human gesture and body rotation is common in indoor scenarios. These blockage forms do not occur in traditional microwave communications. Thus, various kinds of blockage forms need to be considered and addressed in practical deployment of mmWave communication systems.

2.1.3 Channel Sparsity

Unlike that diffraction is rich in low-frequency bands, mmWave channel is relatively sparse that there are only a few clustered paths in the channel. Commonly, the clustered paths consist of one dominant LOS path and a few NLOS paths. These NLOS paths are usually generated by some strong reflectors (e.g., human bodies and building materials). Recent extensive experiments and measurements show how sparse the mmWave channel is [22]. In office, corridor and conference room scenarios, there are less than 5 paths on averagely at the unlicensed 60 GHz band. Similar results have been obtained at 28 GHz band. A study in [23] shows that only averagely 2.4 clustered paths exist in mmWave channel. For example, as shown in Fig. 2.3, only two clustered paths exist between the transmitter

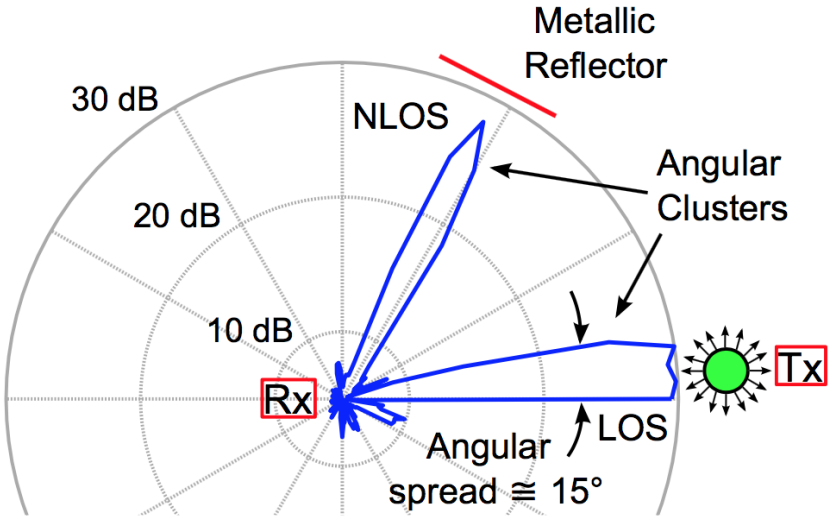

Fig. 2.3: The LOS path and the NLOS path in mmWave communications.

and receiver. One is the LOS path, and another one is the NLOS path which is caused by the strong metallic reflector. The practical performance of the NLOS paths is also widely analyzed via practical experiments. Generally, the NLOS path is expected to suffer extra path loss than the LOS path due to the reflection and longer transmission distance. Measurement results with a ray-tracing method in an office environment show that the first-order reflection NLOS path suffers about 5-10 dB SNR loss compared with the LOS path, and the second-order reflection path is approximately 10-20 dB below the LOS component [24]. As our example shown in Fig. 2.3, the channel gain of the NLOS path suffers from only a few dB SNR loss compared with the LOS path.

2.1.4 Narrow Beamwidth

Unlike the traditional microwave systems which adopt the omni-directional transmission mode, mmWave communications have to be equipped with the directional antennas to compensate the huge path loss. Thus, the beamwidth is usually narrow in order to achieve large antenna gain. For example, 50×50 phased antenna arrays can generate a narrow beam with a 3^o beamwidth, providing a directional antenna gain of 36 dB. The inherent high directionality characteristics is key difference between mmWave communications and traditional microwave transmissions, which results in many challenges in mmWave

communications, such as BA and MAC performance.

2.2 BF Technology

To overcome the huge path loss, BF technology is the key enabling technology in mmWave communications. There are multiple BF technologies in literature. In this section, we first introduce the *analog BF* which is the de-facto BF technology in unlicensed 60 GHz systems, such as 802.11ad. Then, we present the emerging *hybrid BF* technology which can support multiuser transmission. Finally, the BF protocol in 802.11ad is introduced in detail.

2.2.1 Analog BF

Conventional microwave communications below 6 GHz usually adopt the *fully digital BF*, in which BF is performed by the digital baseband processing components, such as digital signal processing (DSP) units. However, the fully digital BF cannot be applied in mmWave communications due to the following two reasons. Firstly, one antenna needs to connect with a RF chain and an analog-to-digital conversion (ADC)/digital-to-analog conversion (DAC) in the fully digital BF architecture. Both RF chain and ADC/DAC are energy-intensive. Since mmWave communication system adopts a large number of antenna elements (more than 32), fully digital BF needs many RF chains and ADCs/DACs, which leads to excessive energy consumption. Secondly, it is difficult to equip many RF chains into the small chip fabrication in mmWave systems due to expensive hardware cost and complexity. Therefore, fully digital BF is unsuitable in mmWave systems considering both energy consumption and hardware cost.

To reduce implementation complexity, an analog BF architecture becomes a de-facto approach in mmWave systems, such as 802.11ad and Wireless HD. As shown in Fig. 2.4, the fully analog BF only employs one RF chain and one DAC/ADC at the transmitter/receiver. The analog BF utilizes analog phase shifters to achieve the directional beam that is generated by giving each antenna a phase shift, i.e., a phase weight vector at the antennas. For low-complexity, the phase weight vectors can be designed based on codebook. A codebook is a matrix, in which each column vector indicates a phase weight vector for the antenna array and forms a specific beam pattern. There are multiple codebook-based analog BF design schemes in literature, which can form various beam patterns. In order to generate uniform antenna gain for different directions, a discrete Fourier transform (DFT) codebook is widely adopted in recent researches [25].

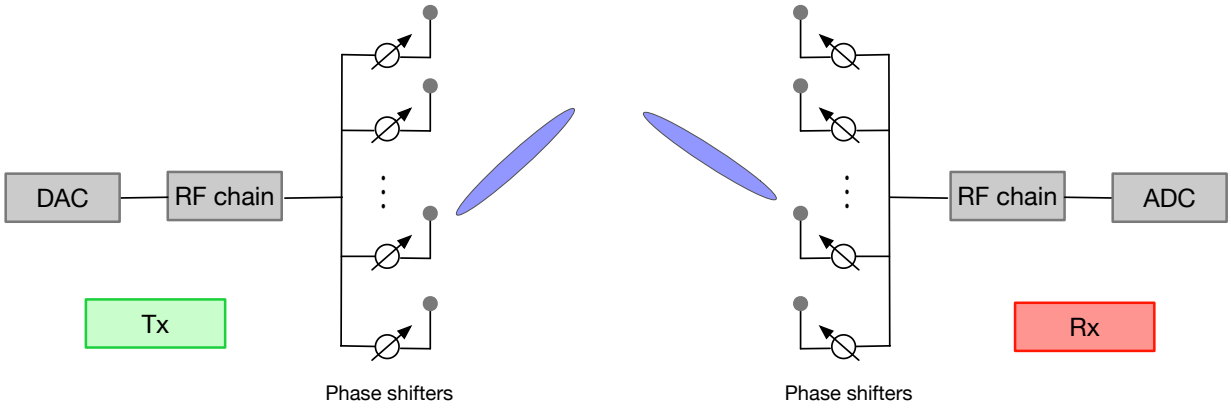

Fig. 2.4: The analog BF architecture in mmWave communications. Analog circuit adjusts the beam direction via shifting phases on the antenna element.

2.2.2 Hybrid BF

Since the analog BF can only support one data stream, extensive researches aim to develop multiuser transmission schemes in mmWave networks. Supporting multiuser transmission can enhance spatial reuse and significantly increase data rate in wireless networks. For example, current 802.11ac standard at lower frequency bands could support up to 4 users. The conventional multiuser transmission in lower frequency bands is implemented by fully digital multiuser BF. As we mentioned before, the fully digital multiuser BF design faces many unique challenges in mmWave systems, such as high hardware complexity, huge overhead in channel estimation and excessive power consumption. These challenges make fully digital multiuser BF are unsuitable in mmWave systems. Developing an energy-efficient yet low-complexity solution for mmWave communication systems is desired.

Hybrid BF that combines analog BF and digital BF, is proposed as the most promising solution to enable multiuser transmission in mmWave systems [26]. In specific, the analog BF controls the signal phase at each antenna element via analog phase shifters to provide sufficient directional antenna gain, and while the digital BF focuses on mitigating the interference in the multiuser transmission. As shown in Fig. 2.5, the hybrid BF architecture needs to be equipped with multiple RF chains to support multiple data streams. Existing literature shows that hybrid BF can achieve a performance that is close to optimal fully digital BF with much lower complexity [27]. Thus, it would be of great benefit if hybrid BF could be applied to mmWave WLAN for multiuser downlink transmission.

A collection of works investigate the performance of hybrid BF in mmWave systems

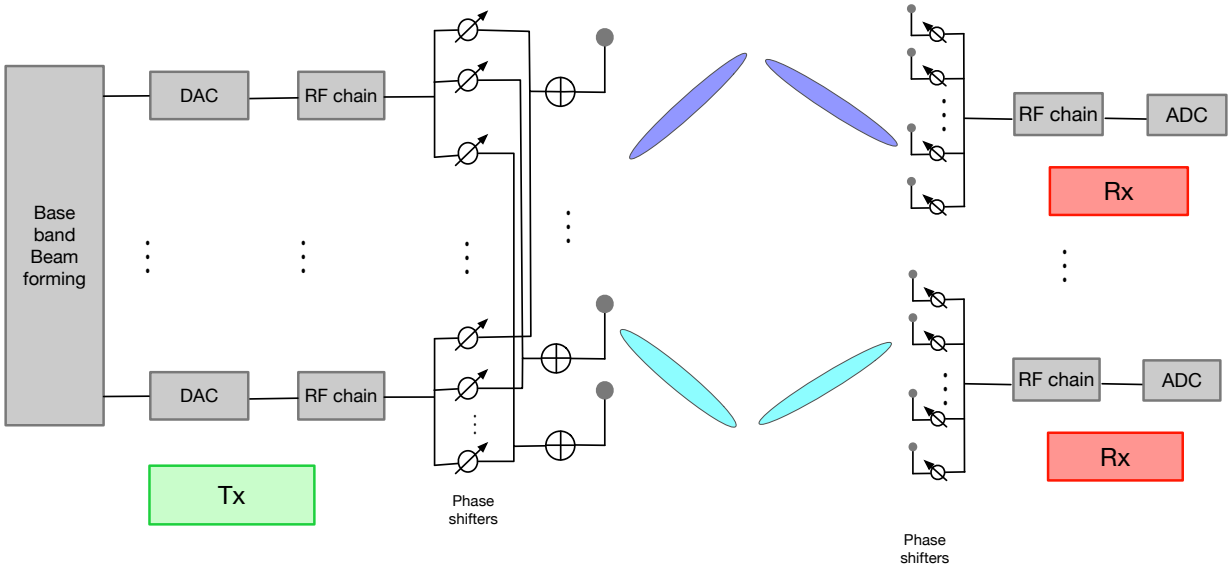

Fig. 2.5: Hybrid BF architecture in mmWave communications.

under different scenarios. A hybrid BF scheme for wideband mmWave communication systems with a feedback between transmitter and receiver is proposed by Alkhateeb *et al.* in [28]. Another work utilized the sparsity of received signal to design hybrid precoding in [29]. An extended work is presented in the mmWave cellular network [30]. Aldubaikhy *et al.* considered the user selection issue in a hybrid BF architecture and then proposed a novel low-complexity hybrid BF scheme which incorporates user selection to enhance the uplink performance in mmWave systems [31]. Wu *et al.* analyzed the protocol overhead of incorporating hybrid BF scheme into current 802.11ad standard [32] and the result indicates huge protocol overhead is incurred by the hybrid BF scheme.

2.2.3 BF Training Protocol

The distinct high directionality feature of BF results in a fundamental challenge in mmWave communications, namely BF training. BF training means that the transmit BF and receive BF must be properly trained to find the optimal transmit-receiver BF pair. BF training is also called beam alignment in the literature. So far, 802.11ad is the most successful standard in mmWave communications. In the following, we will introduce the BF training protocol in 802.11ad. The BF training protocol is made up of three phases: sector level sweep (SLS), beam refinement protocol (BRP) and beam tracking (BT).

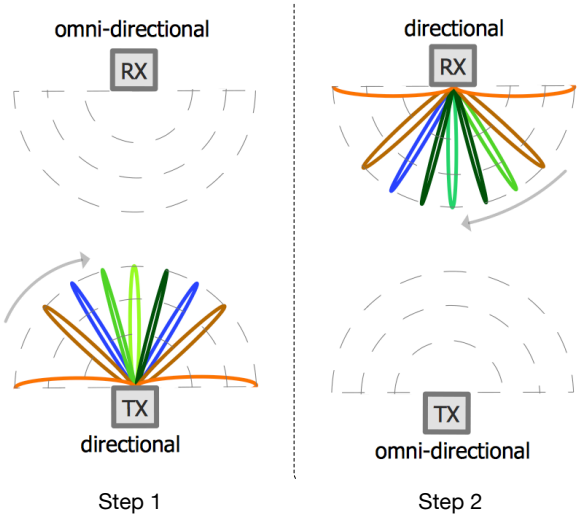

Fig. 2.6: The BF training process in the SLS phase in 802.11ad.

- SLS: In the SLS phase, both the transmitter and the receiver search sector space to obtain the best receive sector and transmit sector. A sector is a coarse-grained beam or a wide beam. Thus, the objective of SLS is to obtain a wide transmit-receive sector beam pair. A detailed process is given in Fig. 2.6, which consists of two steps. In the first step, the transmitter adopts the directional transmission mode (each directional beam will be selected in a sequential manner) while the receiver keeps omni-directional mode. As such, the receiver can obtain the optimal transmit sector ID based on the received signal strength. In the second step, the transmitter keeps omni-directional mode while the receiver adopts the directional mode. Similarly, the best receiver sector ID can be obtained. As such, the optimal transmit-receive sector pair can be obtained. This process is compulsory which must be performed in the A-BFT phase. Since the length of A-BFT phase is limited, the BF training in SLS should be judiciously considered and designed.

- BRP: Note that a sector identified in SLS contains multiple fine-grained beams. Thus, in the BRP phase, both transmitter and receiver search all the fine-grained beams within the identified transmit-receive sector pair to find the best transmit-receive fine-grained beam. In specific, the BRP phase is made up of four sub-phases: BRP setup, multiple sector ID, beam combining and BRP transaction. One can refer to 802.11ad standard for the detailed procedure. The BRP is performed in the data transmission period instead of the limited A-BFT phase.

- BT: BT is an optional phase which is periodically employed during the data transmission period to adjust for the channel variation.

2.3 Commercialization Activities

Although the first attempt of mmWave communications can trace back to more than one hundred years ago by Bose and Lebedew [6], only very recently mmWave communication attracts worldwide attention due to the skyrocketing growth of data traffic in past decade. In industry, many standard bodies and research groups are devoted to standardization and extensive large-scale in-field tests to pave the way for mmWave communications.

2.3.1 Standardization

Multiple working groups have been organized to establish the new standards for mmWave communications. Especially, multiple standards have been ratified by different standardization groups at the unlicensed 60 GHz band.

- **WirelessHD**[2]: WirelessHD is developed by Silicon Image consortium to provide high-definition video transmission via short-range mmWave communications. The achievable data rate is up to 4 Gbit/s which can support common 3D formats and 4K resolution videos.
- **IEEE 802.15.3c [12]**: At the beginning, 802.15.3c is designed to provide an alternative physical layer technology, i.e., mmWave communications, for the existing 802.15.3 WPANs. 802.15.3c operates at 57-64 GHz band (often referred to as the unlicensed 60 GHz band) and can deliver a data rate of more than 2 Gbit/s for simultaneous time dependent applications, such as real time multiple HDTV video stream and wireless data bus for cable replacement.
- **IEEE 802.11ad [11]**: 802.11ad is developed in the former WiGig consortium that was later absorbed into the WiFi Alliance in 2012. 802.11ad leverages nearly 7 GHz spectrum at unlicensed 60 GHz band and provides a data rate up to 6.75 Gbit/s in WLAN with a channel bandwidth of 2.16 GHz. Building on the base of successful 2.4/5 GHz WiFi systems, 802.11ad achieves significant success in the past years. Many COTS products are designed based on 802.11ad. To further promote 802.11ad,

[2]https://en.wikipedia.org/wiki/WirelessHD

Federal Communications Commission (FCC) releases extra 7 GHz unlicensed spectrum at 64-71 GHz band in 2016, which double the amount of available spectrum of 802.11ad. As such, 802.11ad occupies at most six channels, which can support more users or a higher data rate.

- **IEEE 802.11ay [33]**: Observing the great success of 802.11ad, IEEE standardization group is developing the next generation mmWave WLAN based on 802.11ad, named 802.11ay. Compared with 802.11ad, 802.11ay is anticipated to incorporate several distinguished technologies, such as channel bonding and aggregation, multiuser transmission. These new features can significantly enhance data rate which may be up to 40 Gbit/s. The final version of 802.11ay is expected to debut in 2020.

On the other hand, at the licensed band, the standardization activities in mmWave communications are led by 5G-related forums and organizations. The 5G network is expected to support diverse applications, which includes three typical use cases: eMBB that requires extraordinary data rates, massive machine type communications (mMTC) that requires massive connectivity in Internet of things (IoT); and ultra reliable low latency communication (URLLC) that focuses on applications with stringent latency and reliability connection requirement [14]. According to IMT-2020, it is expected that the peak data rate would be 10 Gbit/s in the eMBB use case. Unquestionably, mmWave communication is the most promising technology to satisfy this requirement. To bring mmWave visions to commercialization, 3GPP working group has standardized mmWave communication as a 5G new radio interface in Release 15.

In addition to standardization efforts, many COTS products that support these standards hit the market recently. Products based on WirelessHD have been available for years. Very recently, 802.11ad capable chip set is available from a group of companies, such as Wilocity, Tensorcom, Nitero, etc. [34]. Currently, two 802.11ad capable routers hit the market: Netgear Nighthawk X10 and the TP-Link Talon AD7200 [35]. According to a report from ABI research [36], the market of mmWave WLAN is booming. More than 600 million WiFi chip sets are expected to support 802.11ad in 2020. The on-going standardization of 802.11ay will further catalyze the maturation of mmWave technology in WLAN.

2.3.2 Real-World Evaluation

As mmWave communication is still in the infancy stage, extensive large-scale field-trials by network operators and vendors are performed to evaluate its effectiveness under various

environments. As reported, Samsung conducts the first mmWave mobile communication experiment which achieved a data rate of 1 Gbit/s in 2013[3]. Other network operators, such as T-mobile and Version, have obtained the permission from FCC to test mmWave technology at 28 or 39 GHz band. A joint experiment performed by Nokia and National Instrument which can deliver a data rate up to 15 Gbit/s at 73 GHz band. In China, Huawei performs an experiment at Ka-band (26.5-40 GHz) which demonstrates a 20 Gbit/s access rate for mobile users. Another experiment by DOCOMO and Ericsson at 70 GHz band reaches 4.5 Gbit/s and 2 Gbit/s for outdoor and indoor users, respectively. For the dense urban scenarios, mmWave networks would suffer from significant penetration loss due to the dense buildings which results in a coverage concern of mmWave networks in urban scenarios. To validate the feasibility, NYU WIRELESS research group conducts extensive experiments in New York City at 28 GHz and 38 GHz band, which takes the building penetration and reflection characteristics into consideration. Their results demonstrate that mmWave networks can have a coverage up to 200 meters even in a dense urban environment with a low power base station [37].

To further push the development of mmWave mobile networks, governments all over the world launch multiple research projects on mmWave networks. For example, a joint project by EU and Japan, named "MiWEBA", aims at the mmWave evolution for backhaul and access. Similar projects, "MiWaves" and "mmMAGIC", are also established by EU to push the success of mmWave communications. Not surprisingly, other countries, such as China and America, invest hundreds of millions of dollars in mmWave communications research and implementation. Leading technology companies, such as Google, Facebook, Huawei, also devote extensive research efforts to this topic.

2.4 Multi-armed Bandit Theory

In this section, we introduce the basics of stochastic multi-armed bandit (MAB) theory, which originates from the *exploration* and *exploitation* dilemma. In specific, the exploration means making the best decision given current information, and while the exploration means gathering more information in order to make better decisions. In our daily life, we often face this dilemma. For example, when we play video games, there are two choices. One is to play the move you believe is best, which is exploitation. Another option is to play an experimental move, which is exploration. A similar problem occurs in the optimal online banner adverts placement problem for business groups. You may show the most successful

[3]https://news.samsung.com/global/samsung-announces-worlds-first-5g-mmwave-mobile-technology

advert to users based on their historical records, which is exploitation. On the other hand, you can also show a different advert for users, which is exploration. The best long-term strategy may involve short-term sacrifices. Thus, gathering enough information via exploration to make the best overall decisions is required, and while frequently exploitation may waste constrained resources. How to balance the exploration and exploitation is a challenging issue.

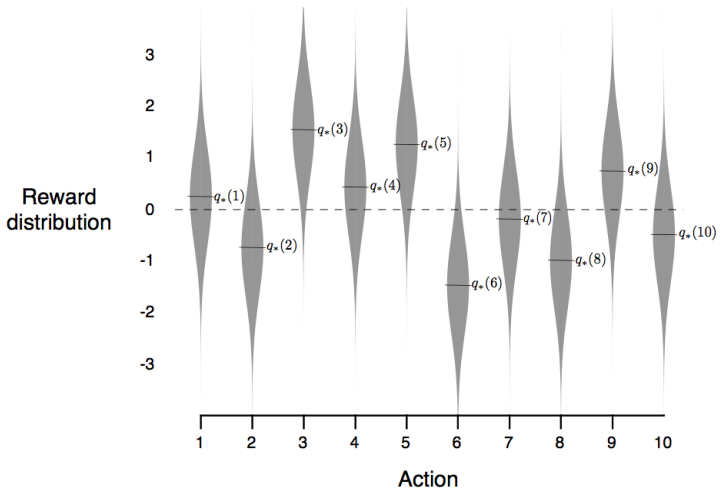

Fig. 2.7: An example of the reward distributions for different actions.

The stochastic MAB learning, which is one of the reinforcement learning methods, can be used to effectively address the exploration and exploitation dilemma. The name of MAB originates from the old-fashioned one-armed bandit machine game in the casino. In this game, there are multiple one-armed bandit machines in front of a gambler. At each time, the gambler pulls an arm of a bandit machine and then gets a reward. The goal of the gambler is to select the arm in a sequential manner to maximize his long-term benefit. This problem is referred to as the stochastic MAB problem. Here, assume that there are N bandit machines, and each bandit machine has independent reward distribution which is unknown to the gambler. For a simple example as shown in Fig. 2.7, there are ten actions and the reward of each action has an independent distribution. As such, the obtained reward at each time is a sample of the reward distribution. In mathematics, stochastic MAB problem can be modeled by a tuple $< A, R >$. Here, A denotes a set of *actions* which is referred to as *arms*, and R represents the set of unknown reward distributions. At each time slot $t = 1, 2, 3...T$, the MAB learning algorithm will select an action a_t and then obtain a reward r_t from the environment. The objective of the MAB problem is to

find a learning algorithm to maximize the cumulative reward.

Previous literature has proposed numerous solutions for MAB problems under different scenarios. For the standard stochastic MAB problem, Lai and Robbins first study the fundamental regret lower bound in [38]. Then, Auer *et. al* proposed the celebrated upper confidence bound (UCB) algorithm to achieve the lower bound [39]. In the literature, many variants based on stochastic MAB problems have been analyzed, including Bayesian bandit problem [40,41] in which some prior knowledge is leveraged to speed up the learning process, combinatorial bandit problem [42] in which the objective is to select the optimal subset of actions instead of a single action, volatile bandit problem [43] in which the set of action varies, the correlated bandit problem [44] in which actions are correlated with each other, and multi-agent bandit problem [45] in which multiple agents independently learn a joint action set. Interested readers are referred to a tutorial survey in [46] and the references therein.

2.5 Summary

This chapter has introduced the distinct propagation characteristics, the BF technology and standardization activities in mmWave communications. The related works on design of mmWave networks have been introduced. By focusing on the related works on mmWave communications, we aim to reach a better understanding of the void and weakness in the current study of this area, and motivate our research works.

Chapter 3

Fast Beam Alignment for mmWave Networks

3.1 Introduction

In mmWave communication systems, narrow directional beams are adopted at both the transmitter and receiver to compensate for the huge attenuation loss. Since beams are narrow, the communication is possible only when the transmitter and receiver beams are properly aligned [47], as shown in Fig. 3.1. BA is such a process to identify the optimal transmit-receive beam pair which attains the maximum received signal strength (RSS). Beam misalignment can dramatically reduce the link budget and drop the throughput from multiple Gbps to a few hundred Mbps [48]. As a key process in mmWave communications, BA is of significance to achieve multi-gigabit wireless transmission. To identify the best beam pair, a naive exhaustive search method scans all the combinations of the transmitter and receiver beams, which results in significant BA latency. Yet, a low-latency BA process is imperative for practical mmWave systems to accommodate real-time applications. Moreover, in mobile scenarios, user mobility changes the beam direction and thus frequently invokes BA, which further exacerbates the latency. To accelerate the beam search, 802.11ad protocol decouples the BA process into two steps. Firstly, the transmitter starts with a quasi-omnidirectional beam and the receiver scans the beam space for the best receiver beam. Secondly, the transmitter scans the beam space for the best transmitter beam while keeping the receiver quasi-omnidirectional. Still, the existing BA method in IEEE 802.11ad may take up to seconds with a large number of candidate beams [49]. To reduce BA latency, can we identify the optimal beam without searching the entire beam

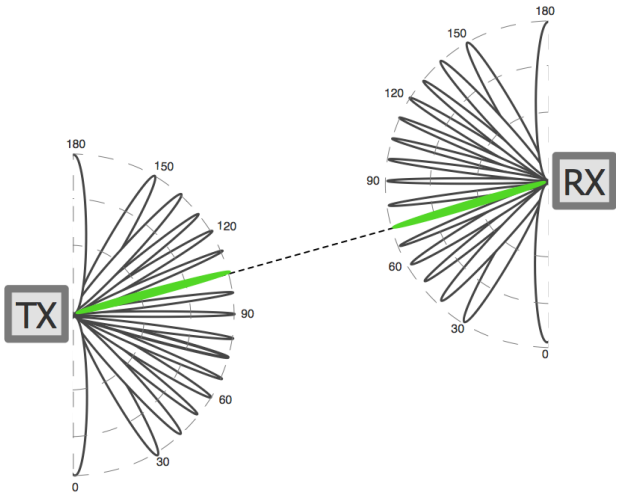

Fig. 3.1: A beam alignment example with 16 beams. The well-aligned transmitter and receiver beams are represented by solid green beams.

space?

In the literature, there are some initial research efforts to address this challenge. Utilizing the sparse characteristic of the mmWave channel, Marzi *et al.* developed a compressed sensing BA method [50]. Some out-of-band information, e.g., the Wi-Fi signal, is exploited to identify the optimal beam in [51]. These works perform BA with the assistance of excessive extra information besides RSS. Surprisingly, a crucial feature, the correlation structure among beams, is ignored in previous works. In fact, the RSS of nearby beams is similar which means nearby beams are highly correlated. In this way, if a beam does not perform well, its nearby beams are highly likely to perform worse either. The measurement of one beam not only reveals information about itself, but also its nearby beams. Hence, the information from nearby beams can be learned to identify the optimal beam without searching the entire beam space.

In this chapter, we propose a fast BA algorithm, named Hierarchical Beam Alignment (HBA), by utilizing the *correlation structure* among beams and the *prior knowledge* on the channel fluctuation. In the BA problem, fast BA means identifying the optimal beam with the minimum latency. This problem boils down to sequentially selecting beams to maximize the cumulative RSS within a certain period, which can be formulated as a stochastic multi-armed bandit (MAB) problem. To solve this problem efficiently, two unique characteristics are incorporated in our proposed algorithm. Firstly, theoretical analysis indicates that the correlation structure among beams in the *multipath* channel can be characterized

by a *multimodal* function. Utilizing this correlation structure, the proposed algorithm intelligently narrows the search space to identify the optimal beam. Secondly, incorporating the prior knowledge on the channel fluctuation to appropriately accommodate reward uncertainty, the proposed algorithm avoids excessive exploration and further accelerates the BA process. Theoretical analysis shows that the regret of HBA is *bounded* and thus the proposed algorithm is asymptotically optimal. Extensive simulation results demonstrate that HBA can identify the optimal beam with a high probability and reduce the number of beam measurements in the multipath channel, even with coarse prior knowledge. Particularly, the proposed algorithm reduces the BA latency by orders of magnitude as compared to the BA method in IEEE 802.11ad.

Our contributions in this work are summarized as follows.

- We formulate the BA problem as a stochastic MAB problem, in which the objective is to sequentially select beams to maximize cumulative RSS within a certain period;
- We prove that the mean RSS function over the beam space follows a multimodality structure in the multipath channel, which characterizes the correlation structure among nearby beams;
- We propose a fast BA algorithm to accelerate beam search by exploiting the correlation structure and the prior knowledge on the channel fluctuation;
- We derive a sublinear analytical upper bound on the cumulative regret, i.e., $O(\sqrt{T \log T})$, indicating the proposed algorithm is asymptotically optimal.

The remainder of this chapter is organized as follows. Section 3.2 reviews related works. The system model and problem formulation are presented in Section 3.3. Section 3.4 proposes a fast BA algorithm. Section 3.5 analyzes the regret performance of the proposed algorithm. Simulation results are given in Section 3.6. Finally, Section 3.7 summarizes this work.

3.2 Literature Review

In this section, we highlight our contributions in the light of previous works. The BA problem in mmWave systems garners much attention recently. Zhou *et al.* elaborated the challenges of the random access protocol in the BA process in dense networks [52]. In addition, the authors developed possible solutions from the MAC perspective. Utilizing the

sparse characteristic that only a few paths exist in the mmwWave channel, a compressed sensing solution can align beams with a low beam measurement complexity of $O(L \log N)$, where L is the number of channel paths and N is the number of beams [50]. The approach suits for mmWave systems where the accurate phase information is available. In another line of research, Wang *et al.* developed a fast-discovery multi-resolution beam search in [53], which probes the wide beam first and continues to narrow beams until identifying the best beam. While feasible, the method needs to adjust the beam resolution at every step. On the other hand, Xiao *et al.* proposed a hierarchical codebook search method to efficiently identify the optimal beam by jointly utilizing sub-array and deactivation techniques [54]. Moreover, they provide the closed-form expression of the hierarchical codebook. Sun *et al.* further developed an orthogonal pilot based low-overhead beam alignment method for the multiuser mmWave systems [55]. Another solution exploits some out-of-band information, i.e., the Wi-Fi signal, to identify the optimal beam [51]. Similar works extract spatial information from sub-6 GHz signals to assist BA as well as boost throughput [56, 57]. Recent efforts leverage the multi-armed beams capability to improve BA performance. Hassanieh *et al.* proposed a fast BA protocol through scanning multiple directions simultaneously [49]. A similar method, which treats the problem of identifying the optimal beam as that of locating the error in linear block codes, is developed to reduce BA complexity [25]. The works in [25, 49–57] provide possible solutions for the BA problem in various scenarios. Different from prior works, our work considers the correlation structure among nearby beams to assist BA process.

MAB theory has been widely applied in wireless networks, such as power allocation in small base stations [41] [44], content placement in edge caching [58, 59], task assignment in mobile crowdsourcing [60] and mobility management in mobile edge computing [61]. Very recently, the BA problem is studied based on MAB theory, which makes online decision to strike the balance between *exploitation* and *exploration*. Gulati *et al.* applied the celebrated upper confidence bound (UCB) algorithm in beam selection in traditional MIMO systems [62]. Sim *et al.* developed an online beam selection algorithm in mmWave vehicular networks based on contextual bandit theory [63]. This work learns information from real-time environment to enhance the throughput of mmWave networks. A pioneering work in [48] exploits a unimodal structure among beams to accelerate the BA process in static environments. This solution focuses on aligning beams in the single-path channel. Another work developed a distributed BA search method based on adversarial bandit theory [64]. These works provide highly relevant insights on the BA problem in mmWave networks via bandit learning theory. However, they do not provide a method to quickly and accurately align beams, especially in complicated multipath channels. Different from existing works, we focus on leveraging the correlation structure and prior knowledge to accelerate the BA

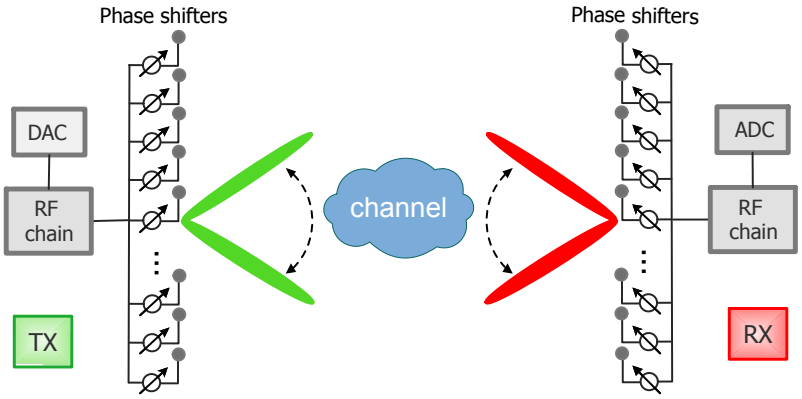

Fig. 3.2: The point-to-point mmWave system.

process in the multipath channel with only RSS.

3.3 System Model and Problem Formulation

3.3.1 Beam Alignment Model

As shown in Fig. 3.2, we consider a static point-to-point mmWave system, where the transmitter is equipped with N antennas. Uniform linear arrays are assumed in both the transmitter and receiver, and each antenna element is connected to a phase shifter to form narrow directional beams [32]. In the BA process, the receiver keeps quasi-omnidirectional while the transmitter scans the beam space to identify the best one. We consider the sparse clustered channel model, i.e., Saleh-Valenzuela model [65]. Suppose that the channel consists of L paths: one dominant LOS path and $L-1$ NLOS paths, due to strong reflections from the ground or side walls. The channel array response between the transmitter and receiver can be represented as a mixture of sinusoids,

$$h_n = g_0 e^{j\frac{2\pi d}{\lambda} n\vartheta_0} + \sum_{l=1}^{L-1} g_l e^{j\frac{2\pi d}{\lambda} n\vartheta_l} \tag{3.1}$$

where $0 \leq n \leq N-1$. Let d and λ denote the array element spacing and carrier wavelength, respectively. Typically, $d = \lambda/2$. Let g_0 and g_l represent the channel gains of the LOS path and the l-th NLOS path, respectively. Note that the channel gain of the NLOS path is around 10 dB weaker than that of the LOS path [24]. Let θ denote the physical angle

of the channel. The corresponding spatial angle of the channel is denoted by $\vartheta = \cos\theta$. We vectorize the sinusoids $e^{j2\pi dn\vartheta/\lambda}, 0 \leq n \leq N-1$ into a vector $\mathbf{x}(\vartheta) \in \mathbb{C}^{N\times 1}$. Thus, the channel vector is given by

$$\mathbf{h} = g_0\mathbf{x}(\vartheta_0) + \sum_{l=1}^{L-1} g_l\mathbf{x}(\vartheta_l) \in \mathbb{C}^{N\times 1}. \tag{3.2}$$

Let $\mathbf{W} = [\mathbf{w}_1, \mathbf{w}_2, ..., \mathbf{w}_N] \in \mathbb{C}^{N\times N}$ denote the unitary Discrete Fourier Transform (DFT) matrix whose columns constitute the transmit beam space, given by

$$\mathbf{W} = \frac{1}{\sqrt{N}}[\mathbf{x}(\omega_1), \mathbf{x}(\omega_2), ..., \mathbf{x}(\omega_N)]. \tag{3.3}$$

In (3.3), $\omega_i = \frac{2i-N}{N}$ represents the spatial angle of the i-th beam [50]. According to the BA method in IEEE 802.11ad, the transmitter scans all the beams in $\mathbf{W}$, while the receiver beam keeps omni-directional. The received signal vector is given by

$$\mathbf{y} = \sqrt{P}\mathbf{h}^H\mathbf{W} + \mathbf{n} \tag{3.4}$$

where $\mathbf{n}$ denotes the additive Gaussian white noise vector. Let N_oW denote the mean noise power, where W is the channel bandwidth and N_o is the noise power density.

The problem of identifying the optimal transmit beam boils down to identifying the element with the maximum magnitude within $\mathbf{y}$. Hence, to identify the optimal beam, the BA method in IEEE 802.11ad protocol needs to measure the RSS of all the transmit beams, leading to a high beam measurement complexity [49]. Searching the entire beam space incurs significant BA latency, especially when the beam space is large.

3.3.2 Problem Formulation

In this subsection, the BA problem is formulated as a stochastic MAB problem for *stationary* environments. Consider a time slotted system with T time slots of equal duration. In time slot $t \in \{1, 2, ..., T\}$, the transmitter selects a beam to transmit data. Let $\mathcal{B} = \{b_1, b_2, ..., b_N\}$ denote the set of candidate beams, which can be considered as *arms* in the bandit theory. At the beginning of time slot t, the transmitter selects a beam denoted by $b^t \in \mathcal{B}$. At the end of time slot t, the transmitter observes noisy RSS from the receiver, i.e., $r\left(b^t\right)$, which is considered as a *reward*. Rigorously, the reward is a random variable due to the channel fluctuation, such as shadow fading and the disturbance effect. For

simplicity, we assume that the reward follows a Gaussian distribution with a variance σ^2. In other words, σ^2 also represents the variance of the channel fluctuation, which is utilized as *prior knowledge* in the following algorithm design. Note that the proposed algorithm can also be applied to non-Gaussian distribution settings, as validated in Section 3.6.

Let $b^{1:t} = \{b^1, b^2, ..., b^t\}$ denote the sequentially selected beams up to time slot t. The set of corresponding sequential rewards is represented by $r^{1:t} = \{r(b^1), r(b^2), ..., r(b^t)\}$. In the MAB setting, a sequential beam selection *policy* is how the transmitter selects the next beam based on previously selected beams $b^{1:t}$ and observed rewards $r^{1:t}$. Let Π be the set of all possible sequential beam selection policies. Our objective is to find a policy, $\pi \in \Pi$, that maximizes the expected cumulative reward (RSS) within a given time horizon of T slots, i.e., $\sum_{t=1}^{T} r(b^t)$. This objective conforms our target since a fast BA algorithm is to identify the optimal beam with the minimum latency.

In the MAB theory, *expected cumulative regret* is commonly adopted to evaluate the performance of a given policy, which denotes the expected cumulative difference between the reward of the selected beam and the maximum reward achieved by the optimal beam. The *expected cumulative regret* is defined as

$$\begin{aligned} R^{\pi}(T) &= \mathbb{E}\left[\sum_{t=1}^{T}\left(r(b^{\star}) - r(b^t)\right)\right] \\ &= T \cdot \mathbb{E}\left[r\left(b^{\star}\right)\right] - \sum_{b_i \in \mathcal{B}} N_{b_i}^{\pi}(T)\mathbb{E}\left[r\left(b_i\right)\right] \end{aligned} \tag{3.5}$$

where $b^{\star}$ represents the optimal beam and $N_{b_i}^{\pi}(T)$ denotes the number of times that b_i has been selected up to time slot T. Hence, maximizing the cumulative reward is equivalent to minimizing the *expected cumulative regret* within T [48], which can be expressed as

$$\begin{aligned} \mathcal{P}1: \min_{\pi \in \Pi} \quad & R^{\pi}(T) \\ \text{s.t.} \quad & \sum_{b_i \in \mathcal{B}} N_{b_i}^{\pi}(T) \leq T & \text{(3.6a)} \\ & N_{b_i}^{\pi}(T) \in \mathbb{Z}, \forall b_i \in \mathcal{B}. & \text{(3.6b)} \end{aligned}$$

The preceding MAB problem $\mathcal{P}1$ can be solved by the celebrated UCB algorithm [39]. However, this problem has two characteristics that were not utilized in the UCB algorithm. Firstly, since the RSS of nearby beams are highly correlated, the correlation information

from nearby beams can be utilized to select the next beam efficiently. Secondly, the prior knowledge on the channel fluctuation reflects the information of environment, which can be exploited to appropriately accommodate reward uncertainty such that the BA process can be further accelerated. In the following, we will leverage these two characteristics to accelerate the convergence speed, and hence reduce BA latency.

3.4 Fast Beam Alignment

In this section, we first analyze and validate that the mean reward (RSS) over the beam space follows a multimodality structure, which characterizes the inherent correlation among beams. Next, by exploiting the correlation structure and the prior knowledge, a fast BA algorithm is proposed to identify the optimal beam.

3.4.1 Correlation Structure

Consider a *cyclic* undirected graph $G = (\mathcal{B}, E)$ whose vertices $\mathcal{B}$ stand for the beams. Let $(b_i, b_{i+1}) \in E$ denote the edge that connects neighboring beams b_i and b_{i+1}. In addition, $(b_N, b_1) \in E$ indicates that the last beam b_N and the first beam b_1 are neighbors since their beam orientations are close to each other. The unimodality structure is defined as follows.

Definition 1 ***(Unimodality)*** *Let $b_{i^\star}$ denote the optimal beam in G. The* unimodality *structure indicates that, $\forall b_i \in \mathcal{B}$, there exist a path, $(b_i, b_{i+1}, ..., b_{i^\star})$, along which the mean reward is strictly increasing.*

In other words, the unimodality structure means that there is no local optimal beam over the beam space. Next, we aim to show that the correlation structure among beams follows above unimodality structure. Consider the single-path channel, where g and ϑ represent the channel gain and channel spatial angle of the path, respectively. With (3.4), the mean RSS is given by

$$
\begin{aligned}
\mathbb{E}\left[r(b_i)\right] &= P\left|\mathbf{h}^H\mathbf{w}_i\right|^2 + N_oW \\
&= \frac{Pg^2}{N}\left|\mathbf{x}^H(\vartheta)\mathbf{x}(\omega_i)\right|^2 + N_oW \\
&= \frac{Pg^2}{N}\left|\sum_{n=0}^{N-1} e^{j\frac{2\pi d}{\lambda}n(\omega_i-\vartheta)}\right|^2 + N_oW \\
&= \frac{Pg^2}{N}D\left(\omega_i-\vartheta\right) + N_oW, \forall b_i \in \mathcal{B}
\end{aligned}
\tag{3.7}
$$

where

$$
D(x) = \frac{\sin^2(N\pi dx/\lambda)}{\sin^2(\pi dx/\lambda)} \tag{3.8}
$$

denotes the antenna directivity function, which depends on the angular misalignment x. Hence, the mean RSS is a function of angular misalignment $\omega_i - \vartheta$.

Theorem 1 *In the single-path channel, the mean reward (RSS) over the beam space is a unimodal function.*

Proof. Proof is provided in Appendix 3.8.1. □

The linear combination of several unimodal functions is a *multimodal* function, which means that there exist several local optimums.

Corollary 1 *In the multipath channel, the mean reward (RSS) over the beam space is a multimodal function. The dominant peak of the multimodal function is caused by the LOS path, while other peaks are caused by NLOS paths.*

Proof. Proof is provided in Appendix 3.8.2. □

For example, Fig. 3.3 shows the RSS function over the beam space in a two-path channel. Even though the practical RSS is noisy due to the channel fluctuation, we observe that the mean RSS function follows the multimodality structure. For a two-path mmWave channel, there exists two peaks in the mean RSS function, where the dominant peak is due to the LOS path and another smaller peak is due to the NLOS path. Furthermore, the multimodality structure has been observed in many in-field measurements in mmWave systems, which further validates our theoretical results.

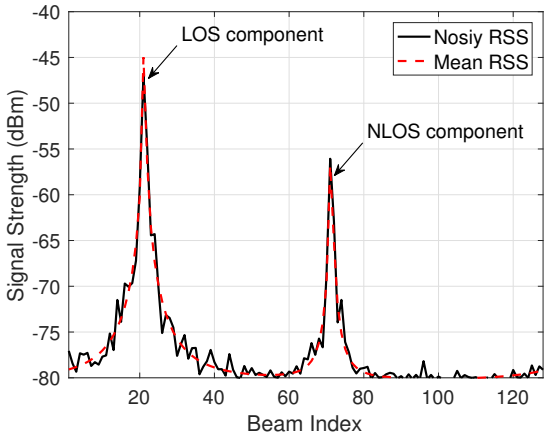

Fig. 3.3: The RSS function over the beam space in a two-path channel with 128 beams. The peak caused by the LOS link is around 10 dB higher than that by the NLOS link.

Remark 1 *Theoretical analysis indicates that the RSS depends on the angular misalignment. As the angular misalignment of nearby beams is close, the RSS of nearby beams is similar such that nearby beams are highly correlated. In addition, due to the multipath nature of channel, the RSS function exhibits the multimodality structure, which can be utilized to accelerate the convergence speed of the BA process.*

3.4.2 Prior Knowledge

In addition to the aforementioned correlation structure, some prior knowledge can be leveraged to further speed up the BA process. As the reward is impacted by wireless environments, channel fluctuation statistics reflects the underlying information of the wireless environments. Leveraging the channel fluctuation statistics can appropriately accommodate the reward uncertainty such that less exploration is required. Specifically, the variance of the channel fluctuation σ^2 is assumed to be known *a priori* to accelerate the BA process. In practice, the prior knowledge can be obtained in the system initialization phase before the BA process is invoked. Practical mmWave systems also collect the variance of channel fluctuation periodically. Besides, since the channel statistical information changes slowly in static environments, there is no need to frequently collect the information. It is worth noting that the proposed algorithm works even with coarse prior knowledge at the expense of slower convergence or lower beam detection accuracy, which is presented in Section 3.6.

3.4.3 Hierarchical Beam Alignment (HBA) Algorithm

As discussed, the mean reward function exhibits the multimodality structure, and hence we adapt and extend the hierarchical optimistic optimization (HOO) algorithm [66] to the BA problem. Due to the lack of prior knowledge, HOO adopts a large confidence margin to accommodate the reward uncertainty, which results in slow convergence. Similar to the well-known Bayesian principles in [40], we leverage the prior knowledge to obtain an appropriate confidence margin, which avoids unnecessary exploration and further accelerates convergence. The proposed HBA algorithm is sketched in Algorithm 1. Specifically, $Ber(p)$ represents a Bernoulli distribution with a parameter p, and $leaf(\mathcal{T})$ represents the leaf node of a tree $\mathcal{T}$ in the algorithm.

The proposed algorithm is designed based on the correlation structure among beams. If a beam performs well, its nearby beams are highly likely to perform well too. Hence, the core idea is to explore intensively around good beams while loosely in others. For this purpose, a search tree is constructed, whose nodes are associated with search regions. A deeper node represents a smaller search region, as an illustrative example shown in Fig. 3.4(a). The algorithm operates in discrete time slots, and the binary tree is constructed in an incremental manner. At each time slot, a new node is selected by a node selection process and added to the search tree. Once selected, the beam located in the selected node is measured, and then the corresponding reward is observed. Then, the attributes of the search tree are updated based on the newly observed reward. In this way, the algorithm intelligently narrows the search region until the optimal beam is identified. It is worth noting that selecting a new node means exploring the region associated to the node, and the search tree explores the region based on previously selected beams and observed rewards.

Next, we elaborate the algorithm in detail. In the initialization phase, the beam space, $\mathcal{B}$, is mapped to a region $\mathcal{X} = [0, 1]$, which is uniformly partitioned by each beam. Similarly, the RSS function, $r(b_i), \forall b_i \in \mathcal{B}$, is mapped to a normalized reward function, $f(x), \forall x \in \mathcal{X}$, within $[0, 1]$. In the beginning, the search tree $\mathcal{T}$ only contains a root node $(0, 1)$. The node in the tree is represented by (h, j), where h denotes the depth from the root node and $j, 1 \leq j \leq 2^h$ denotes the index at depth h. In addition, each node in the tree is associated with a region. Let $C_{h,j}$ represent the region of (h, j). Specifically, the root node represents the entire region, i.e., $C_{0,1} = [0, 1]$. Let $(h+1, 2j-1)$ and $(h+1, 2j)$ denote the left and the right child node of (h, j), respectively. Two child nodes partition the region of their parent node. Consider $C_{h,j} = [x_L, x_H]$, the left child node is associated with a region $C_{h+1,2j-1} = [x_L, x_a]$ and the right child node is associated with a region $C_{h+1,2j} = [x_a, x_H]$, where $x_a = x_L + (x_H - x_L)/2$ is the middle point of $C_{h,j}$. At time slot t, HBA consists of

Algorithm 1: HBA algorithm

Input: ζ, ρ_1, γ and σ^2
Output: $b^\star$

Initialization: Set $\mathcal{T} = \{(0,1)\}$, $Q_{2,1} = Q_{2,2} = +\infty$, $x_L = 0$ and $x_H = 1$;
for *t=1,2,3...* **do**
  $(h,j) \leftarrow (0,1)$, $\mathcal{P} \leftarrow \{(h,j)\}$;
  ▷ New node selection
  while $(h,i) \in \mathcal{T}_t$ **do**
    if $Q_{h+1,2j-1}(t) > Q_{h+1,2j}(t)$ **then**
      $(h,j) \leftarrow (h+1, 2j-1)$, update $x_L = x_a$;
    else if $Q_{h+1,2j-1}(t) < Q_{h+1,2j}(t)$ **then**
      $(h,j) \leftarrow (h+1, 2j)$, update $x_H = x_a$;
    else
      $(h,j) \leftarrow (h+1, 2j - Ber(0.5))$, update the search region;
    end if
    $\mathcal{P} \leftarrow \mathcal{P} \cup \{(h,j)\}$;
  $(H_t, J_t) \leftarrow (h,j)$; $\mathcal{T}_{t+1} = \mathcal{T}_t \cup \{(H_t, J_t)\}$;
  ▷ Attributes update
  Measure the beam located in the center C_{H_t,J_t}, and observe the reward r^t;
  $\forall (h,j) \in \mathcal{P}$, update $N_{h,j}(t)$ and $R_{h,j}(t)$ with (3.9) and (3.10), respectively;
  $\forall (h,j) \in \mathcal{T}_t$, update $E_{h,j}(t)$ with (3.11);
  $Q_{H+1,2J-1}(t) = Q_{H+1,2J}(t) = +\infty$; $\hat{\mathcal{T}} = \mathcal{T}_t$;
  for $(h,j) \in \hat{\mathcal{T}}$ **do**
    $(h,j) \leftarrow leaf(\hat{\mathcal{T}})$, update $Q_{h,j}(t)$ with (3.12), $\hat{\mathcal{T}} \leftarrow \hat{\mathcal{T}} \setminus (h,j)$;
  ▷ Terminating condition
  if $x_H - x_L < \zeta/N$ **then**
    Terminate beam search and select current beam $b^\star$;
  end if

the following three phases:

1. *New node selection.* In this phase, a new node will be selected. Let $\mathcal{T}_t$ denote the tree at time t. At each time slot, starting from the root node, the estimated rewards (denote by Q-values) of two children are compared until a new node $(H_t, J_t) \notin \mathcal{T}_t$ is selected. Specifically, traversing the tree, the child with a higher Q-value is chosen, otherwise breaking ties randomly (lines 5-6). The selected node is added to the tree, i.e., $\mathcal{T}_{t+1} = \mathcal{T}_t \cup \{(H_t, J_t)\}$,

and the path from the root node to the selected node is stored in $\mathcal{P}$.

2. *Attributes update*. In this phase, the attributes of all the nodes in the tree are updated. For the selected node in the previous phase, a beam located in the center of C_{H_t,J_t} is measured and the corresponding reward r_t is obtained. Based on the newly observed reward, the estimated mean reward $Q_{h,j}(t)$ is updated by the following steps.

Firstly, as the new node is the descendant of all the nodes in path $\mathcal{P}$, $N_{h,j}(t)$, which represents the number of times that (h,j) has been selected until time slot t, is updated by

$$N_{h,j}(t) = N_{h,j}(t-1) + 1, \forall (h,j) \in \mathcal{P}. \tag{3.9}$$

Secondly, $R_{h,j}(t)$ represents the mean measured reward of (h,j) up to time slot t, which is updated by

$$R_{h,j}(t) = \frac{(N_{h,j}(t)-1) R_{h,j}(t-1) + r^t}{N_{h,j}(t)}, \forall (h,j) \in \mathcal{P}. \tag{3.10}$$

Thirdly, for each node in the tree, the initial estimated reward $E_{h,j}(t)$ is updated by,

$$E_{h,j}(t) = \begin{cases} R_{h,j}(t) + \sqrt{\frac{2\sigma^2 \log t}{N_{h,j}(t)}} + \rho_1 \gamma^h, & \text{if } N_{h,j}(t) > 0 \\ +\infty, & \text{otherwise} \end{cases} \tag{3.11}$$

where $\sqrt{\frac{2\sigma^2 \log t}{N_{h,j}(t)}}$ is the confidence margin to accommodate for the uncertainty of rewards. As aforementioned, we adopt the Bayesian principle to design the confidence margin by leveraging the prior knowledge on the variance of channel fluctuation. The term $\rho_1 \gamma^h$ accounts for the maximum variation of the mean reward function over $C_{h,j}$, where $\rho_1 > 0$ and $\gamma \in (0,1)$. This term is due to the bounded diameter assumption, which is discussed later in Section 3.5.2. The values of ρ_1 and γ are selected based on extensive simulation trials. For a binary tree case, γ is typically set to 0.5 [66]. Note that E-values of all the unexplored nodes are set to infinity.

Finally, for each node in the tree, the estimated mean reward, $Q_{h,j}(t)$, should be recursively updated through the following bound

$$Q_{h,j}(t) = \begin{cases} \min\{E_{h,j}(t), \max\{Q_{h+1,2j-1}(t), Q_{h+1,2j}(t)\}\}, & \text{if } N_{h,j}(t) > 0 \\ +\infty, & \text{otherwise} \end{cases} \tag{3.12}$$

This bound depends on two terms. The first term, $E_{h,j}(t)$, is an upper bound for $Q_{h,j}(t)$ due to the definition of E-values. The second term, $\max\{Q_{h+1,2j-1}(t), Q_{h+1,2j}(t)\}$,

is another valid upper bound of $Q_{h,j}(t)$. Since $C_{h,j} = C_{h+1,2j-1} \cup C_{h+1,2j-1}$, the maximum value between the Q-values in two subsets is the upper bound of Q-value in the union set. Combining both terms together, a tighter upper bound is obtained via taking the minimum value of these two bounds. Note that Q-values should be updated from the leaf node of the tree because Q-values of child nodes form the upper bound of their parent node (lines 12-15).

3. *Terminating condition.* As the tree is constructed over time, the search region gradually narrows as the depth of the tree increases. When the search region is sufficiently small, i.e., $x_H - x_L < \zeta/N$ where $0 < \zeta < 1$, the BA process is terminated and the beam located in the final region is selected as the optimal beam. The value of ζ should be carefully selected based on extensive simulation trials. Noteworthily, a larger ζ value results in faster convergence while lower beam detection accuracy.

Illustrative example: For better understanding of HBA, we provide two illustrative examples in Fig. 3.4. Firstly, as shown in Fig. 3.4(a), HBA operates similar to a "zooming" process. At the beginning, the search region is the entire region, which is uniformly partitioned by the beams. As time goes by, the search region is adaptively partitioned, and the algorithm gradually zooms to the region that contains the optimal beam. Secondly, sequentially selected beams in the BA process are depicted in Fig. 3.4(b). The selected beams are divided into three batches according to the timeline. The first batch beams locate randomly in the whole region. The second batch beams get closer to the dominant peak. The last batch beams mainly focus around the optimal beam. We observe that the proposed algorithm explores intensively in the regions that contain good beams while loosely on the others.

3.5 Performance Analysis

3.5.1 Complexity Analysis

At time slot T, $\mathcal{T}_t$ contains T nodes as the tree increments by one node at each time slot. Hence, the storage complexity of the proposed algorithm is linear, i.e., $O(T)$. In addition, the attributes of all the nodes in the tree should be updated at each time slot, and hence the running time at each time slot is also linear. As the algorithm runs T time slots, the computational complexity of the HBA algorithm is a quadratic complexity $O(T^2)$. With the terminating condition, the tree is a finite tree and hence both storage complexity and computational complexity are bounded.

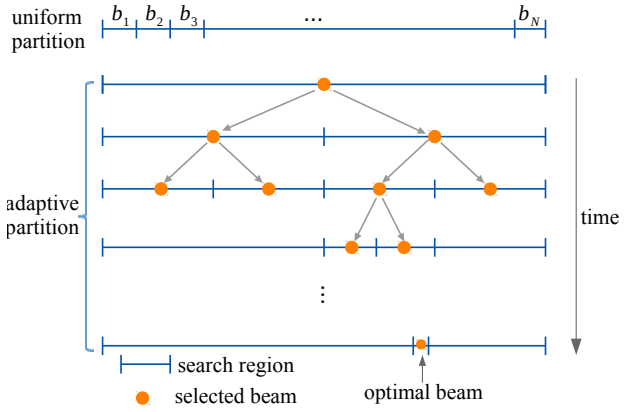

(a) Zooming process

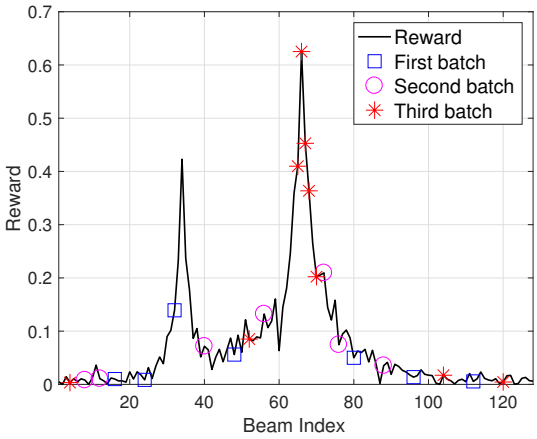

(b) Sequentially selected beams

Fig. 3.4: Illustrative examples of the HBA algorithm. (a) The proposed algorithm operates in a "zooming" manner. (b) The region that contains the dominant peak is explored intensively, while others are explored loosely.

3.5.2 Regret Performance Analysis

In this section, we analyze the upper bound on the cumulative regret for the proposed algorithm. For the tractability of regret analysis, we have the following two assumptions.

Assumption 1 ***(Weak Lipschitz)*** *For any x around the optimal $x^\star$, there exist con-*

stants $c_H > 0$ and $\alpha > 0$ such that

$$f^\star - f(x) \leq c_H \|x^\star - x\|^\alpha. \tag{3.13}$$

This assumption indicates that the reward function satisfies the week Lipschitz condition, which can avoid sharp valleys around the optimal point that induces high regret. Furthermore, the weak Lipschitz condition is mild, which only has the impact on the region in the vicinity of the optimal value. This assumption is well justified in many practical applications [44].

Assumption 2

1. **(Bounded diameter)** For a region, $C_{h,j}$, of depth h, the diameter of the region is defined as $D(C_{h,j}) = \max_{x,y \in C_{h,j}} q(x,y)$, where $q(x,y) = w\|x-y\|^\beta$ represents the dissimilarity between x and y. The diameter of the region is upper bounded by $\rho_1 \gamma^h$ for constants $\rho_1 > 0$ and $0 < \gamma < 1$.
2. **(Well-shaped region)** For a region, $C_{h,j}$, of depth h, the region contains a ball with a radius of $\rho_2 \gamma^h$ which locates in the center of $C_{h,j}$.

The bounded diameter condition is to upper bound the maximum variation of $f(x)$ within the region $C_{h,j}$. In contrast, the well-shaped region condition is to lower bound the minimum variation of $f(x)$ within the region $C_{h,j}$. Note that any region in the reward function satisfies the bounded diameter and well-shaped region conditions [66], which are utilized to bound the cumulative regret in the following analysis.

Definition 2 ***ϵ-optimal****: Let $f^\star_{h,j} = \max_{x \in C_{h,j}} f(x)$ be the optimal reward in $C_{h,j}$. If $f^\star_{h,j} > f^\star - \epsilon_{h,j}$, $C_{h,j}$ is the $\epsilon_{h,j}$-optimal region.*

For example, if $\epsilon_{h,j} = 0$, $C_{h,j}$ is the optimal region where the optimal value $x^\star$ locates. Otherwise, if $\epsilon_{h,j} > 0$, $C_{h,j}$ is a sub-optimal region. Let $\epsilon_{h,j}$ represent the *suboptimality* of (h,j).

To obtain the regret bound, we first provide the following lemma.

Lemma 1 *For any node (h, j) whose suboptimality is larger than $\rho_1\gamma^h$, the expected number of times that (h, j) has been visited until time slot T, is upper bounded by*

$$\mathbb{E}\left[N_{h,j}(T)\right] \leq \frac{8\sigma^2 \log T}{\left(\epsilon_{h,j} - \rho_1\gamma^h\right)^2} + c \tag{3.14}$$

where c is a constant.

Proof. The detailed proof is given in Appendix 3.8.3. □

Remark 2 *From Lemma 1, the number of times that a suboptimal node has been visited logarithmically increases with time, which implies the cumulative regret of the proposed algorithm is sublinear. In addition, the number of times that a suboptimal node has been visited, depends on the variance of the channel fluctuation. A larger variance of the channel fluctuation implies a more noisy wireless environment, which yields more exploration efforts to remove the reward uncertainty.*

Based on above lemma, an upper bound is obtained in the following.

Theorem 2 *The upper bound on the cumulative regret of HBA is*

$$R^{\pi}(T) = O\left(\sqrt{T \log T}\right). \tag{3.15}$$

Proof. The detailed proof is given in Appendix 3.8.4. □

Remark 3 *Theorem 2 indicates the expected cumulative regret of HBA is sublinear in the time horizon T, i.e., $\lim_{T\to\infty} R^{\pi}(T)/T = 0$. Since the per-slot regret diminishes over time, the proposed algorithm is asymptotically optimal. Hence, the proposed algorithm converges to the optimal beam over time. Moreover, for finite time horizon T, the regret bound characterizes the convergence speed of the proposed algorithm.*

3.6 Simulation Results

We simulate an IEEE 802.11ad system, operating at 60 GHz with a bandwidth of 2.16 GHz [67]. Consider an outdoor scenario, such as university campus, where the transmission distance between the transmitter and the receiver is set to 20 m unless otherwise specified. The average effective isotropically radiated power (EIRP) P_e is fixed at 50 dBm[1],

[1]For outdoor applications with the high antenna gain, the average EIRP limit is up to 82 dBm [68].

which is consistent with FCC regulations for 60 GHz unlicensed bands [68, 69]. Taking the directional antenna gain into consideration, the transmit power is $P = P_e - 10\log_{10} N$. For instance, the transmit powers are set to around 32 dBm and 23 dBm for the 64 and 512 antenna arrays, respectively. It is worth noting that the mmWave channel is sparse, and hence we set the maximum number of channel paths to 5, which consists of one dominant LOS path and four NLOS paths. For the LOS path, the path loss is modeled as

$$PL(dB) = 32.5 + 20\log_{10}(f) + 10\xi\log_{10}(d) + \chi \tag{3.16}$$

where f, ξ, d, and χ represent the carrier frequency, path loss exponent, transmission distance, and shadow fading, respectively. The shadow fading follows $N(0, \sigma^2)$ where σ is set to 2 dB [70]. Note that the channel fluctuation in the simulation is mainly caused by the shadow fading. In addition, according to practical in-field measurements, NLOS paths suffer around 10 dB more path loss than the LOS path [24]. We assume that the extra NLOS path loss follows a uniform distribution within $[7, 13]$ dB. Furthermore, for the HBA algorithm, the RSS within $[-80, -20]$ dBm is mapped to a reward within $[0, 1]$. The algorithm parameters, ρ_1, γ, and ζ are set to 3, 0.5, and 0.1, respectively, based on extensive simulation trials. Important simulation parameters are listed in Table 3.1. We evaluate the performance via Monte-Carlo simulations. Simulation results are averaged based on 50000 samples with different channel fading and locations. The proposed HBA algorithm is compared to the following benchmarks:

- **IEEE 802.11ad** [11]: In this industrial method, one side (transmitter or receiver) scans the beam space, while the other side keeps omni-directional.
- **UCB** [39]: The celebrated algorithm selects the beam without exploiting both correlation structure and prior knowledge. The confidence margin is $\eta_u\sqrt{2\log t/N_{b_i}(t)}$, where the learning rate η_u is set to 0.2.
- **Unimodal beam alignment (UBA)** [48]: The algorithm exploits the unimodal structure among beams to perform BA. Hence, it works in a "hill-climbing" manner, which selects the best beam among the neighboring beams at each time slot.
- **HOO** [66]: The algorithm selects the beam by exploiting beam correlation, without the prior knowledge. The confidence margin is $\eta_h\sqrt{2\log t/N_{h,j}(t)} + c_1\gamma^h$, where the learning rate η_h is set to 0.1.

Table 3.1: Simulation parameters in beam alignment.

Parameter	**Value**
Noise spectrum density (N_o)	-174 dBm/Hz
System bandwidth (W)	2.16 GHz
Carrier frequency (f)	60 GHz
Path loss exponent (ξ)	1.74
Shadowing fading variance (σ)	2 dB
Signal range	$[-80, -20]$ dBm
SSW frame duration (T_{SSW})	15.8 us
Beacon interval duration (T_{BI})	100 ms
Number of beams (N)	{8-512}
Effective isotropically radiated power (P_e)	50 dBm
Number of paths (L)	{1-5}
Algorithm parameters (ρ_1, γ)	$(3, 0.5)$
Terminating condition threshold (ζ)	0.1
Time horizon (T)	1000 time slots
Extra NLOS path loss	$U(7, 13)$ dB
Transmission distance (d)	20 m

3.6.1 Regret Performance

Figure 3.5(a) shows the cumulative regret performance in two-path channels. Several important observations can be obtained from simulation results. First of all, HBA significantly outperforms other benchmarks. A "bounded regret" behavior is observed, which complies with the theoretical results in Theorem 2. In addition, HBA converges much faster than other benchmarks. Specifically, HBA only takes around 25 time slots to converge to the optimal beam. This is because HBA exploits both correlation structure and prior information to accelerate the BA process, while other benchmarks only exploit correlation structure or not. It is interesting to note that, as time goes by, the UBA algorithm performs even worse than the BA method in IEEE 802.11ad which does not exploit the correlation structure. The reason is that the UBA algorithm is designed based on the unimodal structure among beams, while the reward function evolves to a multimodal structure in the multipath channel. This model mismatch results in worse performance than not exploiting the correlation structure at all.

We further evaluate the impact of the channel fluctuation distribution on the regret performance in Fig. 3.5(b). To evaluate the dependency of the Gaussian distribution, the performance under Gaussian distribution is compared to that under two well-adopted

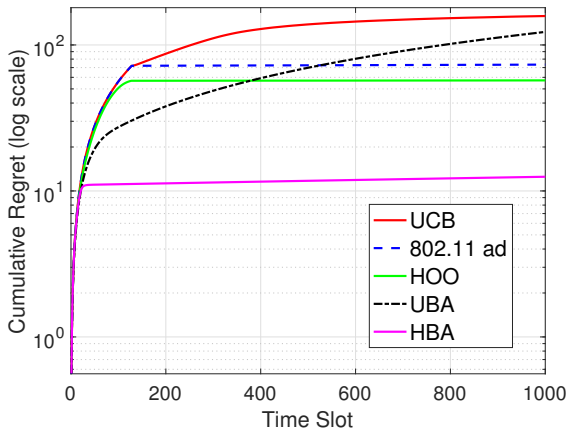

(a) Cumulative regret performance comparison.

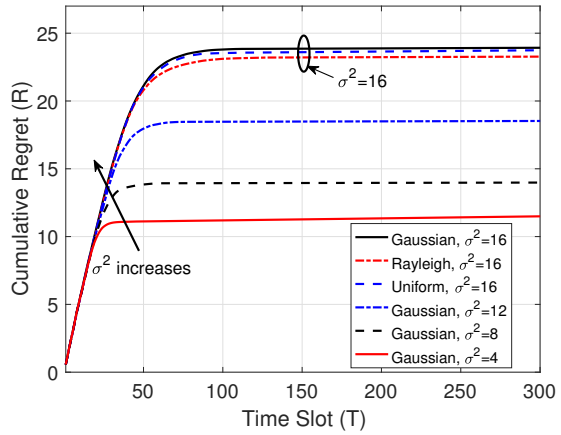

(b) Impact of the channel fluctuation distribution and variance.

Fig. 3.5: Cumulative regret performance in the multipath channel.

non-Gaussian distributions, i.e., uniform distribution and Rayleigh distribution. The performance under non-Gaussian settings is very close to that under the Gaussian distribution, which means that the proposed algorithm can be applied in various settings. Furthermore, the impact of the channel fluctuation variance (σ^2) is studied in Fig. 3.5(b). As expected, the cumulative regret increases as the variance increases, because more exploration efforts are required in highly fluctuated channels.

3.6.2 Measurement Complexity and Beam Detection Accuracy

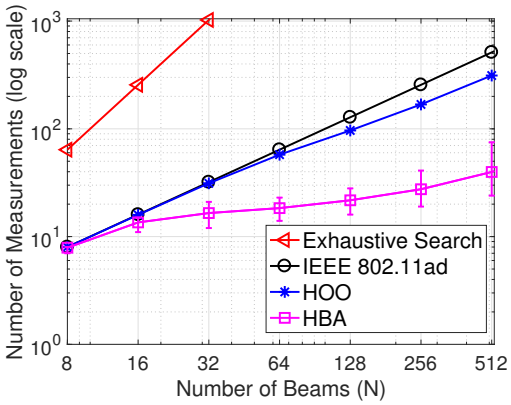

(a) Number of beam measurements in the single-path channel

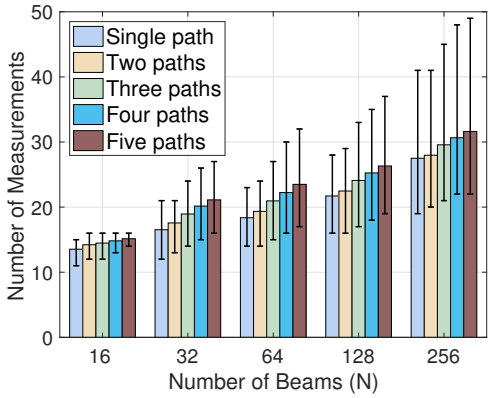

(b) Number of beam measurements in the multipath channel

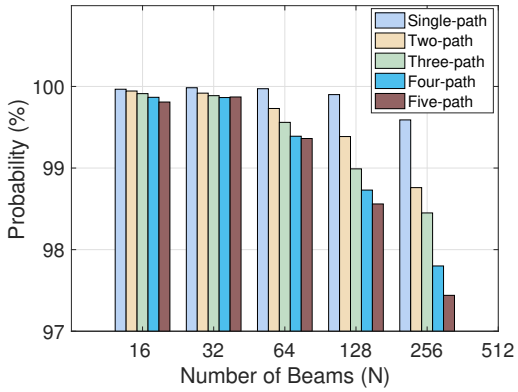

(c) Beam detection accuracy in the multipath channel

Fig. 3.6: Performance comparison with respect to the number of paths. Error bars show the 90 percentile performance.

The regret performance only reflects the bounded fact of regret, not necessarily the actual performance. Next, we evaluate the performance of HBA using following two metrics: the number of measurements and beam detection accuracy.

We first evaluate the scalability of the proposed algorithm with the number of beams, as shown in Fig. 3.6(a). It is evident that the proposed algorithm significantly reduces

the required number of measurements as compared to other benchmarks. For a small number ($N = 32$) of beams, the proposed algorithm reduces the number of measurements by 2 times as compared to the 802.11ad benchmark. Furthermore, the proposed algorithm achieves higher performance gains for larger numbers of beams. For instance, for a large number ($N = 512$) of beams, the proposed algorithm only needs around 40 measurements to identify the optimal beam, which reduces the number of measurements by 12 times as compared to the 802.11ad benchmark. The reason is that, different from the BA method in 802.11ad that explores all the beams, the proposed algorithm only needs to explore a few beams by leveraging the correlation structure and the prior knowledge. The results validate that the proposed algorithm is a scalable solution even with a large number of beams.

As shown in Fig. 3.6, we further study the performance in the multipath channel. Due the inherent sparse characteristics of the mmWave channel, the number of paths is selected from 1 to 5. Firstly, the numbers of measurements in terms of the number of paths are compared in Fig. 3.6(b). It can be seen that the number of measurements increases slightly as the number of paths increases. For example, for a 128-beam case, the number of measurements in the five-path channel increases by 15% as compared to that in the single-path channel. Secondly, beam detection accuracy performance is presented in Fig. 3.6(c). The HBA algorithm detects the optimal beam with a high probability, even in sophisticated multipath channels. Simulation results show that the beam detection accuracy is higher than 97%, even in the worst case. In addition, the beam detection accuracy slightly decreases as the number of paths increases. For a large number ($N = 256$) of beams, the beam detection accuracy decreases from 99.6% in the single-path channel to 97.4% in the five-path channel due to the sophisticated multipath channel.

Figure 3.7 shows the impact of the transmission distance on the performance. We first observe that the number of measurements increases in terms of the transmission distance, as shown in Fig. 3.7(a). Specifically, the number of measurements increases by 32% as distance increases from 5 meters to 50 meters for $N = 128$. Because the RSS is weaker for a longer distance such that limited information can be extracted from nearby beams. Hence, the proposed algorithm needs to explore more beams to identify the optimal beam for remote users. Even for remote users, the proposed BA algorithm performs better than the 802.11ad benchmark. When the distance increases to 50 meters, our algorithm needs about 44 measurements for $N = 256$, which still reduces the number of measurements by 5.8 times as compared to the 802.11ad benchmark. Finally, the beam detection accuracy is presented in Fig. 3.7(b). Even in the low SNR case, the proposed algorithm can detect the optimal beam with a high probability.

For implementation consideration, Fig. 3.8 presents the performance of HBA under

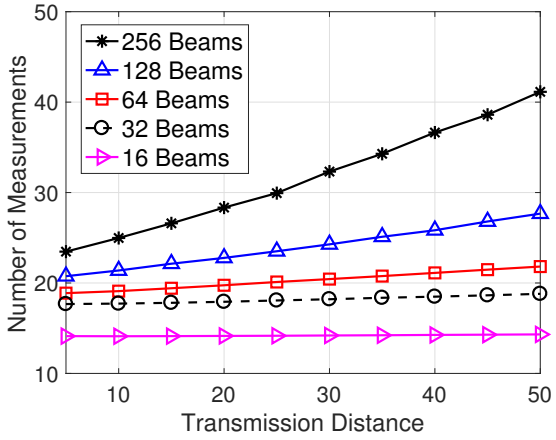

(a) Number of measurements

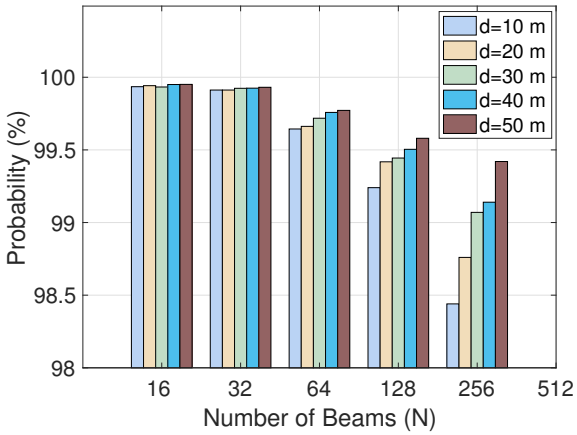

(b) Beam detection accuracy

Fig. 3.7: Performance comparison with respect to transmission distance in two-path channels.

coarse prior knowledge conditions. The metric of the coarse prior knowledge is defined as a ratio between the estimated variance (σ_e^2) and the accurate one, i.e., $\eta = \sigma_e^2/\sigma^2$. Hence, the coarse prior knowledge can be divided into two categories: the underestimated prior knowledge when $\eta < 1$ and the overestimated prior knowledge when $\eta > 1$. We can see from Fig. 3.8(a) that the number of measurements increases as η increases from 0.25 to 4. Specifically, for a 256-beam case, the HBA algorithm with the overestimated prior knowledge for $\eta = 4$ requires more beam measurements as compared to that with

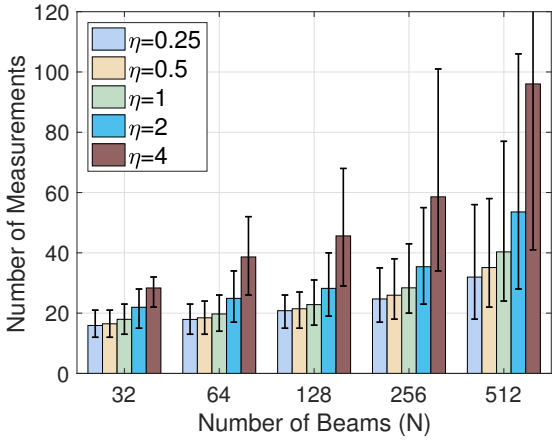

(a) Number of beam measurements

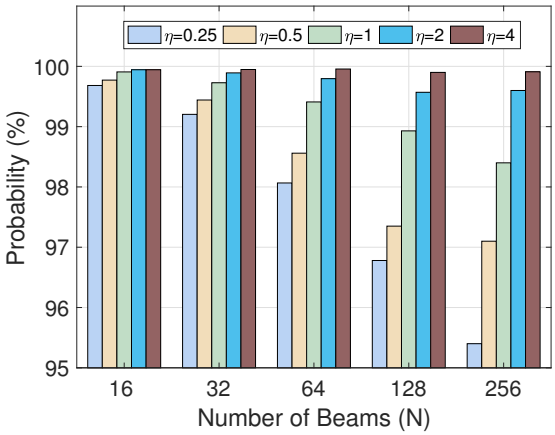

(b) Beam detection accuracy

Fig. 3.8: Performance comparison with coarse prior knowledge in two-path channels.

accurate prior knowledge. Overestimating prior knowledge results in a larger confidence margin to accommodate reward uncertainty, such that more exploration efforts are needed and better beam detection accuracy can be achieved, as shown in Fig. 3.8(b). In contrast, when prior knowledge is underestimated, the number of measurements is slightly smaller than that with accurate prior knowledge, while the beam detection accuracy decreases due to insufficient exploration efforts. More importantly, even with the coarse prior knowledge, the proposed algorithm can substantially reduce the number of measurements as compared

Table 3.2: BA latency comparison in the multipath channel.

N	**One user**		**Four-user**	
	802.11ad	**HBA**	**802.11ad**	**HBA**
8	0.25 ms	0.25 ms	0.63 ms	0.63 ms
16	0.51 ms	0.45 ms	1.26 ms	1.12 ms
32	1.01 ms	0.56 ms	2.53 ms	1.39 ms
64	2.02 ms	0.61 ms	103.03 ms	1.53 ms
128	4.04 ms	0.71 ms	304.04 ms	1.78 ms
256	106.07 ms	0.88 ms	706.07 ms	2.21 ms

to benchmarks, and achieve high beam detection accuracy. For a 256-beam case, even in the worst case, the proposed algorithm reduces the number of measurements by 6 times in comparison with the BA method in 802.11ad.

3.6.3 BA Latency

Practical BA latency needs to take the 802.11ad protocol into consideration, which is different from a simple product of the number of measurements and the duration of each measurement. In the protocol, BA must be performed in the associated beamforming training (A-BFT) stage, which contains 8 A-BFT slots, and each A-BFT slot contains 16 sector sweep (SSW) frames. Each SSW frame can only provide one measurement for one beam and has a duration about 15.8 *us* [11]. If the BA process cannot be finished in the A-BFT stage of the current beacon interval (BI), this BA process has to wait for the A-BFT stage in the next BI, which increases the BA latency for a whole BI duration. In the simulation, the duration of BI is set to 100 ms [11]. With the above protocol, BA latency is calculated based on the average number of measurements. Table 3.2 presents the BA latency with different numbers of beams in the two-path channel. As expected, the BA latency increases as the number of beams increases. For the case with one user, the proposed algorithm reduces the BA latency significantly as compared to the BA method in 802.11ad. In particular, for a large number ($N = 256$) of beams, the BA latency drops from 106.07 ms to only 0.88 ms. This is because the BA process with the proposed algorithm can be finished in one BI as a small number of measurements is required to identify the optimal beam. Furthermore, a larger performance gain can be observed in the four-user case. In contrast to the BA method in 802.11ad which incurs more than 700 ms latency for a 256-beam phase arrays, the proposed algorithm takes about 2.21 ms, which corresponds

to two orders of magnitude gain.

3.7 Summary

In this work, we have investigated the BA problem in mmWave systems to find the optimal beam pair. We have developed HBA, a learning algorithm which leverages the inherent correlation structure among beams and the prior knowledge on the channel fluctuation to accelerate the BA process. The proposed HBA algorithm can identify the optimal beam with a high probability using a small number of beam measurements, even when the number of beams is large.

3.8 Appendix

3.8.1 Proof of Theorem 1

According to (3.7), the maximum RSS can be achieved with the minimum angular misalignment denoted by, $\delta = \omega_{i^\star} - \vartheta$, where $\omega_{i^\star}$ is the spatial angle for the optimal transmit beam. Hence, $D\left(\omega_i - \vartheta\right)$ can be rewritten as

$$\begin{aligned} D\left(\omega_i - \vartheta\right) &= D\left(\delta + \frac{2(i - i^\star)}{N}\right) \\ &= \frac{\sin^2(N\pi d\delta/\lambda)}{\sin^2\left(\pi d\left(\delta + \frac{2(i-i^\star)}{N}\right)/\lambda\right)}, \forall b_i \in \mathcal{B}. \end{aligned} \tag{3.17}$$

From simple analysis in (3.17), $D\left(\omega_i - \vartheta\right)$ monotonically increases in $[i^\circ, i^\star]$ and decreases in $[i^\star, i^\star + \frac{N}{2}]$, where $i^\circ = i^\star - \frac{N}{2}$. Hence, the mean RSS function over the beam space increases along path $(b_{i^\circ}, b_{i^\circ+1}, ..., b_{i^\star})$ and decreases along path $(b_{i^\star}, b_{i^\star+1}, ..., b_{i^\circ-1})$, i.e., $r(b_{i^\circ}) < r(b_{i^\circ+1}) < ... < r(b_{i^\star}) > ... > r(b_{i^\circ-2}) > r(b_{i^\circ-1})$. With the definition of the unimodality structure, the mean RSS function is unimodal over the beam space in the single-path channel, and the theorem statement follows.

3.8.2 Proof of Corollary 1

Similar to (3.7), the mean RSS in the multipath channel is represented by

$$\mathbb{E}\left[r(b_i)\right] = \underbrace{\frac{Pg_0^2}{N} D\left(\omega_i - \vartheta_0\right)}_{\text{LOS component}} + \underbrace{\sum_{l=1}^{L-1} \frac{Pg_l^2}{N} D\left(\omega_i - \vartheta_l\right)}_{\text{NLOS component}} + N_o W \tag{3.18}$$

Above equation indicates that the aggregated RSS consists of a LOS component and several NLOS components. For each individual path of the mmWave channel, the corresponding RSS function is unimodal function based on Theorem 1. Hence, the RSS function in the multipath channel is the aggregation of several unimodal functions, which can be considered as a multimodal function. Specifically, L paths exist in the mmWave channel, which corresponds to L peaks in the multimodal function. As the channel gain of the LOS path is significantly larger than that of NLOS paths, i.e., $g_0^2 > g_l^2$. Hence, the dominant peak corresponds to the LOS path while other peaks correspond to NLOS paths. Hence, the Corollary 1 is proved.

3.8.3 Proof of Lemma 1

For any integer $m > 0$, according to the definition, the average times that node (h, j) has been visited up to time slot T, is given by

$$\begin{aligned}
\mathbb{E}\left[N_{h,j}(T)\right] &= \mathbb{E}\left[\sum_{t=1}^{T} \mathbb{1}_{(H_t, J_t) \in C_{h,j}}\right] \\
&= \mathbb{E}\left[\sum_{t=1}^{T} \mathbb{1}_{\{(H_t, J_t) \in C_{h,j}, N_{h,j}(t) \leq m\}}\right] + \mathbb{E}\left[\sum_{t=1}^{T} \mathbb{1}_{\{(H_t, J_t) \in C_{h,j}, N_{h,j}(t) > m\}}\right] \\
&\leq m + \mathbb{E}\left[\sum_{t=m+1}^{T} \mathbb{1}_{\{(H_t, J_t) \in C_{h,j}, N_{h,j}(t) > m\}}\right] \\
&= m + \sum_{t=m+1}^{T} \mathbb{P}\left((H_t, J_t) \in C_{h,j}, N_{h,j}(t) > m\right).
\end{aligned} \tag{3.19}$$

where $\mathbb{1}_{\{\cdot\}}$ is the indicator function and $(H_t, J_t) \in C_{h,j}$ denotes the selected node (H_t, J_t) locates within $C_{h,j}$. The first equality is because $N_{h,j}(t) > m$ only occurs when t is larger

than m.

We apply a case study to obtain an upper bound of $\mathbb{E}[N_{h,j}(T)]$. Assume node (h,j) is selected at time slot t. The path from root node $(0,1)$ to (h,j) is given by, $\mathcal{P} = \{(0,1),(1,j_1^\star),...,(k,j_k^\star),(k+1,j_{k+1}^o),...,(h,j)\}$, where k denotes the largest depth of the optimal node in the path. Before node $(k,j_k^\star)$, the optimal nodes are selected. For notation simplicity, we omit the time slot t in $Q_{k,j}(t)$. After traversing node $(k,j_k^\star)$, a sub-optimal node $(k+1,j_{k+1}^o)$ is selected instead of the optimal node $(k+1,j_{k+1}^\star)$ because the suboptimal node has a larger Q-value than the optimal node, i.e., $Q_{k+1,j^o} \geq Q_{k+1,j^\star}$. As Q-values increase along path $\mathcal{P}$, we have $Q_{k+1,j^\star} \leq Q_{k+1,j_{k+1}^o} \leq,...,\leq Q_{h,j}$. Note that Q-values are upper bounded by E-values according to the definition, such that $Q_{k+1,j^\star} \leq E_{h,j}$. Further, event $Q_{k+1,j^\star} \leq E_{h,j}$ can be interpreted as the union of two events, $\{Q_{k+1,j^\star} \leq f^\star\} \cup \{E_{h,j} \geq f^\star\}$. Hence, the probability that (H_t,J_t) locates within $C_{h,j}$ is upper bounded by

$$\mathbb{P}\left((H_t,J_t) \in C_{h,j}\right) \leq \mathbb{P}\left(Q_{k+1,j^\star} \leq f^\star\right) + \mathbb{P}\left(E_{h,j} \geq f^\star\right). \tag{3.20}$$

With the definition of Q-value, the Q-value of a node is the minimum value among the E-value of the node and B-values of its child nodes. Hence, event $\{Q_{k+1,j^\star} \leq f^\star\}$ can be interpreted as the union of two new events, $\{E_{k+1,j^\star} \leq f^\star\} \cup \{Q_{k+2,j_{k+2}^\star} \leq f^\star\}$. Since event $\{Q_{k+2,j_{k+2}^\star} \leq f^\star\}$ can be further recursively expanded as $\bigcup_{s=k+2}^{t-1} \{E_{s,j_s^\star} \leq f^\star\}$, we have

$$\mathbb{P}\left(Q_{k+1,j^\star} \leq f^\star\right) \leq \sum_{s=k+1}^{t-1} \mathbb{P}\left(E_{s,j_s^\star} \leq f^\star\right). \tag{3.21}$$

Substituting (3.21) and (3.20) into (3.19), (3.19) can be rewritten as

$$\mathbb{E}\left[N_{h,j}(T)\right] \leq m + \sum_{t=m+1}^{T} \left(\sum_{s=k+1}^{t-1} \mathbb{P}\left(E_{s,j^\star}(t) \leq f^\star\right) + \mathbb{P}\left(E_{h,j}(t) \geq f^\star, N_{h,j}(t) > m\right) \right). \tag{3.22}$$

The following analysis is to bound the three terms in (3.22) separately.

Firstly, since m is an arbitrary integer, taking m as the smallest integer that satisfies

the condition $m \geq \frac{8\sigma^2 \log T}{\left(\epsilon_{h,j} - c_1 \gamma^h\right)^2}$. Hence m is bounded by

$$m \leq \frac{8\sigma^2 \log T}{\left(\epsilon_{h,j} - \rho_1 \gamma^h\right)^2} + 1. \tag{3.23}$$

Secondly, we aim to bound the first term $\mathbb{P}\left(E_{s,j^\star} \leq f^\star\right)$. For the optimal nodes $(h, j^\star)$, according to the definition of E-values, $E_{h,j^\star} = \infty$ when $N_{h,j^\star} = 0$. Hence, event $E_{h,j^\star} \leq f^\star$ only occurs when $N_{h,j} \geq 1$. As a result, $\mathbb{P}\left(E_{h,j^\star} \leq f^\star\right)$ can be rewritten as

$$\begin{aligned}
\mathbb{P}\left(E_{h,j^\star} \leq f^\star, N_{h,j} \geq 1\right) &= \mathbb{P}\left(R_{h,j^\star} + \sqrt{\frac{2\sigma^2 \log t}{N_{h,j^\star}}} + \rho_1 \gamma^h \leq f^\star, N_{h,j^\star} \geq 1\right) \\
&= \mathbb{P}\left(\left(f^\star - R_{h,j^\star} - \rho_1 \gamma^h\right) N_{h,j^\star} \geq \sqrt{2\sigma^2 N_{h,j^\star} \log t}, N_{h,j^\star} \geq 1\right) \\
&\overset{(a)}{=} \mathbb{P}\left(\sum_{s=1}^{t} \left(f^\star - f(X_s) + \rho_1 \gamma^h\right) \mathbb{1}_{(H_t, J_t) \in C_{h,j^\star}}\right. \\
&\quad \left. + \sum_{s=1}^{t} \left(f(X_s) - Y_s\right) \mathbb{1}_{(H_t, J_t) \in C_{h,j^\star}} \geq \sqrt{2\sigma^2 N_{h,j^\star} \log t}, N_{h,j^\star} \geq 1\right) \\
&\overset{(b)}{\leq} \mathbb{P}\left(\sum_{s=1}^{t} \left(f(X_s) - Y_s\right) \mathbb{1}_{(H_t, J_t) \in C_{h,j^\star}} \geq \sqrt{2\sigma^2 N_{h,j^\star} \log t}, N_{h,j^\star} \geq 1\right) \\
&\overset{(c)}{=} \mathbb{P}\left(\sum_{p=1}^{N_{h,j^\star}} \left(\tilde{Y}_p - f(\tilde{X}_p)\right) \geq \sqrt{2\sigma^2 N_{h,j^\star} \log t}, N_{h,j^\star} \geq 1\right).
\end{aligned} \tag{3.24}$$

In (3.24), the first step follows from the definition of E-value in (3.11); (a) is obtained from the definition of $N_{h,j^\star}$, where $X_s, \forall s = 1, 2, ..., t-1$ denotes the sequentially selected beams up to time $t-1$ and the corresponding reward sequence is represented by Y_s; (b) follows from the fact that $f^\star - f(X_t) - \rho_1 \gamma^h < 0$ holds for all the beams in the optimal region $C_{h,j^\star}$; (c) is because the definition of a new beam selection sequence $\hat{X}_p, \forall p = 1, 2, 3, ...$ whose corresponding reward sequence is $\hat{Y}_p$.

Let $T_p = \min\{t : N_{h,j}(t) = p\}$ represent the time sequence for the selected node in $C_{h,j}$. The sequentially selected beams can be represented by a new sequence $\hat{X}_p = X_{T_p}, \forall p =$

$1, 2, 3, ...$, and (3.24) can be further bounded by

$$\begin{aligned}
&\mathbb{P}\left(\sum_{p=1}^{N_{h,j_h^\star}}\left(\tilde{Y}_p - f(\tilde{X}_p)\right) \geq \sqrt{2\sigma^2 N_{h,j^\star}\log t}, N_{h,j_h^\star} \geq 1\right) \\
&\overset{(a)}{\leq} \sum_{s=1}^{t}\mathbb{P}\left(\sum_{p=1}^{s}\left(\tilde{Y}_p - f(\tilde{X}_p)\right) \geq \sqrt{2\sigma^2 s\log t}\right) \overset{(b)}{\leq} \sum_{s=1}^{t}\exp\left(-\frac{4\sigma^2 s\log t}{s\sigma^2}\right) = t^{-3}.
\end{aligned} \tag{3.25}$$

In (3.25), (a) can be acquired via the union bound that takes all possible values of $N_{h,j_h^\star}$; as $\tilde{D}_p = \tilde{Y}_p - f(\tilde{X}_p)$ can be considered as martingale differences, (b) is obtained via the Hoeffding-Azuma inequality [66]

$$\mathbb{P}\left(\sum_{p=1}^{k}\tilde{D}_p \geq t\right) \leq \exp\left(-\frac{2t^2}{\sum_{p=1}^{k}\sigma^2}\right). \tag{3.26}$$

Thirdly, for suboptimal nodes (h, j), the upper bound of $\mathbb{P}\left(E_{h,j} \geq f^\star, N_{h,j} > m\right)$ can be obtained via a similar method of bounding $\mathbb{P}\left(E_{h,j^\star} \leq f^\star, N_{h,j} \geq 1\right)$, such that

$$\begin{aligned}
&\mathbb{P}\left(E_{h,j} \geq f^\star, N_{h,j} > m\right) \\
&= \mathbb{P}\left(R_{h,j} + \sqrt{\frac{2\sigma^2\log t}{N_{h,j}}} + \rho_1\gamma^h \geq f_{h,j}^\star + \epsilon_{h,j}, N_{h,j} > m\right) \\
&\overset{(a)}{\leq} \mathbb{P}\left(R_{h,j} \geq f_{h,j}^\star + \frac{\epsilon_{h,j} - \rho_1\gamma^h}{2}, N_{h,j} > m\right) \\
&= \mathbb{P}\left(\left(R_{h,j} - f_{h,j}^\star\right)N_{h,j} \geq \frac{\epsilon_{h,j} - \rho_1\gamma^h}{2}N_{h,j}, N_{h,j} > m\right) \\
&= \mathbb{P}\left(\sum_{s=1}^{t}\left(Y_s - f_{h,j}^\star\right)\mathbb{1}_{(H_s,J_s)\in C_{h,j}} \geq N_{h,j}\frac{\epsilon_{h,j} - \rho_1\gamma^h}{2}, N_{h,j} > m\right) \\
&\leq \mathbb{P}\left(\sum_{s=1}^{t}\left(Y_s - f(X_s)\right)\mathbb{1}_{(H_s,J_s)\in C_{h,j}} \geq N_{h,j}\frac{\epsilon_{h,j} - \rho_1\gamma^h}{2}, N_{h,j} > m\right) \\
&\overset{(b)}{=} \mathbb{P}\left(\sum_{p=1}^{N_{h,j}}\left(\hat{Y}_p - f(\hat{X}_p)\right) \geq N_{h,j}\frac{\epsilon_{h,j} - \rho_1\gamma^h}{2}, N_{h,j} > m\right)
\end{aligned} \tag{3.27}$$

In (3.27), (a) due to the substitution of $N_{h,j}(t) \geq \frac{8\sigma^2 \log t}{\left(\epsilon_{h,j}-\rho_1\gamma^h\right)^2}$ where $m \geq \frac{8\sigma^2 \log t}{\left(\epsilon_{h,j}-\rho_1\gamma^h\right)^2}$; (b) is obtained via a similar method as (3.24)(c), where a new beam sequence $\{\hat{X}_1, \hat{X}_2, ..., \hat{X}_p\}$ is formed to represent the sequentially selected beams in $C_{h,j}$. Next, (3.27) can be further bounded by

$$\begin{aligned}
&\mathbb{P}\left(\sum_{p=1}^{N_{h,j}}\left(\hat{Y}_p - f(\hat{X}_p)\right) \geq N_{h,j}\frac{\epsilon_{h,j}-\rho_1\gamma^h}{2}, N_{h,j} > m\right) \\
&\overset{(a)}{\leq} \sum_{k=m+1}^{t} \mathbb{P}\left(\sum_{p=1}^{k}\left(\hat{Y}_p - f(\hat{X}_p)\right) \geq \frac{k(\epsilon_{h,j}-\rho_1\gamma^h)}{2}\right) \\
&\overset{(b)}{\leq} \sum_{k=m+1}^{t} \exp\left(-\frac{k\left(\epsilon_{h,j}-\rho_1\gamma^h\right)^2}{2\sigma^2}\right) \\
&\leq t\exp\left(-\frac{m\left(\epsilon_{h,j}-\rho_1\gamma^h\right)^2}{2\sigma^2}\right) \\
&\overset{(c)}{\leq} t\exp\left(-4\log T\right) = tT^{-4}
\end{aligned} \tag{3.28}$$

In (3.28), (a) is due to a similar union bound in (3.25)(a); (b) is obtained via the Hoeffding-Azuma inequality; (c) is obtained via the substitution of $m \geq \frac{8\sigma^2 \log T}{\left(\epsilon_{h,j}-\rho_1\gamma^h\right)^2}$.

Finally, substituting (3.23), (3.25) and (3.28) into (3.22), the upper bound is given by

$$\begin{aligned}
\mathbb{E}\left[N_{h,j}(T)\right] &\leq \frac{8\sigma^2\log T}{\left(\epsilon_{h,j}-\rho_1\gamma^h\right)^2} + 1 + \sum_{t=m+1}^{T}\left(\sum_{k+1}^{t-1} t^{-3} + tT^{-4}\right) \\
&\leq \frac{8\sigma^2\log T}{\left(\epsilon_{h,j}-\rho_1\gamma^h\right)^2} + 1 + \sum_{t=1}^{T}\left(t^{-2}+T^{-3}\right) \\
&\leq \frac{8\sigma^2\log T}{\left(\epsilon_{h,j}-\rho_1\gamma^h\right)^2} + c
\end{aligned} \tag{3.29}$$

where c is a costant. The last step is because $\sum_{t=1}^{T} t^{-2}$ is bounded. Hence, Lemma 1 is proved.

3.8.4 Proof of Theorem 2

All nodes with depth h can be divided into two subsets: Φ_h that denotes the set of all the $2\rho_1\gamma^h$-optimal nodes, and Ω_h that denotes the set of nodes whose parents belong to Φ_{h-1} while itself does not belong to Φ_h. Let $H \geq 1$ be an integer whose value is determined later. With above definition, $\mathcal{T}$ can be divided into three subtrees: $\mathcal{T}_1$, $\mathcal{T}_2$ and $\mathcal{T}_3$. Let $\mathcal{T}_1$ contain Φ_H and its decedents. Let $\mathcal{T}_2$ include all the $2\rho_1\gamma^h$-optimal nodes at all the depths smaller than H, i.e., $\mathcal{T}_2 = \bigcup_{h=1}^{H-1} \Phi_h$. Let $\mathcal{T}_3$ include all the nodes in Ω_h at all the depths smaller than H, i.e., $\mathcal{T}_3 = \bigcup_{h=1}^{H} \Omega_h$. Hence the cumulative regret can be partitioned as

$$R^{\pi}(T) = \mathbb{E}\left[R^{\pi}(\mathcal{T}_1)\right] + \mathbb{E}\left[R^{\pi}(\mathcal{T}_2)\right] + \mathbb{E}\left[R^{\pi}(\mathcal{T}_3)\right] \tag{3.30}$$

where

$$\mathbb{E}\left[R^{\pi}(\mathcal{T}_i)\right] = \mathbb{E}\left[\sum_{t=1}^{T} \left(f^{\star} - f(X_t)\right) \mathbb{1}_{\{(H_t, J_t) \in \mathcal{T}_i\}}\right].$$

Next, the regret analysis follows the idea of bounding the regret on each subtree separately.

Step 1: Bounding the regret on $\mathcal{T}_1$. As each node in Φ_H is $2\rho_1\gamma^H$-optimal, all the beams located in Φ_H are $4\rho_1\gamma^H$-optimal, i.e., $f^{\star} - f(X_t) \leq 4\rho_1\gamma^H$, $X_t \in \Phi_H$. In addition, it is obvious that the number of nodes in subtree $\mathcal{T}_1$ is smaller than the time horizon, i.e., $|\mathcal{T}_1| \leq T$ where $|\cdot|$ represents the cardinality operator. Therefore, the regret on $\mathcal{T}_1$ is upper bounded by

$$\mathbb{E}\left[R^{\pi}(\mathcal{T}_1)\right] \leq 4\rho_1\gamma^H T. \tag{3.31}$$

Step 2: Bounding the regret on $\mathcal{T}_2$. As $\mathcal{T}_2 = \bigcup_{h=1}^{H-1} \Phi_h$ and each beam in Φ_h is $4\rho_1\gamma^h$-optimal, the regret on $\mathcal{T}_2$ can be written as $\mathbb{E}\left[R^{\pi}(\mathcal{T}_2)\right] \leq \sum_{h=1}^{H-1} 4\rho_1\gamma^h|\Phi_h|$. Based on the results in [66], we have $|\Phi_h| \leq c_1\left(\rho_2\gamma^h\right)^{-\kappa}$ where $\kappa = \frac{1}{\beta} - \frac{1}{\alpha}$. Specifically, α and β are give in the weak Lipschitz assumption and bounded diameter assumption respectively.

The regret on $\mathcal{T}_2$ can be further bounded by

$$\begin{aligned}\mathbb{E}\left[R^{\pi}\left(\mathcal{T}_2\right)\right] &\leq \sum_{h=1}^{H-1} 4\rho_1\gamma^h c_1\left(\rho_2\gamma^h\right)^{-\kappa} \\ &= 4\rho_1 c_1\rho_2^{-\kappa}\sum_{h=0}^{H-1}\gamma^{h(1-\kappa)} \\ &\leq \frac{4\rho_1 c_1\rho_2^{-\kappa}}{1-\gamma^{1-\kappa}}.\end{aligned} \tag{3.32}$$

From (3.32), we can see that $\mathbb{E}\left[R^{\pi}\left(\mathcal{T}_2\right)\right]$ is upper bounded by a constant as $\mathcal{T}_2$ is a finite tree.

Step 3: Bounding the regret on $\mathcal{T}_3$. For each node in Ω_h, its parents should be included by Φ_{h-1}. Thus, all the beams in Ω_h are $4\rho_1\gamma^{h-1}$-optimal and the cardinality of Ω_h is smaller than $2|\Phi_{h-1}|$. Besides, with the results in Lemma 1, $\mathbb{E}\left[N_{h,j}(t)\right] = \frac{8\sigma^2\log t}{\left(\rho_1\gamma^h\right)^2} + c$, for any $2\rho_1\gamma^{h-1}$-optimal nodes. Thus, the regret on $\mathcal{T}_3$ is given by

$$\begin{aligned}\mathbb{E}\left[R^{\pi}\left(\mathcal{T}_3\right)\right] &\leq \sum_{h=1}^{H} 4\rho_1\gamma^{h-1}2|\Phi_{h-1}|\mathbb{E}\left[N_{h,j}(T)\right] \\ &\leq 8\rho_1 c_1\rho_2^{-\kappa}\sum_{h=1}^{H}\gamma^{(h-1)(1-\kappa)}\left(\frac{8\sigma^2\log T}{\left(\rho_1\gamma^h\right)^2} + c\right).\end{aligned} \tag{3.33}$$

Finally, substituting (3.31), (3.32) and (3.33) into (3.30), we have

$$\begin{aligned}R^{\pi}(T) &\leq 4\rho_1\gamma^H T + \frac{4\rho_1 c_1\rho_2^{-\kappa}}{1-\gamma^{1-\kappa}} + 8\rho_1 c_1\rho_2^{-\kappa}\sum_{h=1}^{H}\gamma^{(h-1)(1-\kappa)}\left(\frac{8\sigma^2\log T}{\left(\rho_1\gamma^h\right)^2} + c\right) \\ &= O\left(\gamma^H T + \log T\gamma^{-H(1+\kappa)}\right) \\ &= O\left(T^{\frac{\kappa+1}{\kappa+2}}\left(\log T\right)^{\frac{1}{\kappa+2}}\right).\end{aligned} \tag{3.34}$$

The last step is obtained from setting γ^H as the order of $\left(T/\log T\right)^{-1/(\kappa+2)}$ [66]. If the soothness of the function is known, we can set $\alpha = \beta$ such that $\kappa = 0$ [66]. Hence, (3.34) can be rewritten as $O\left(\sqrt{T\log T}\right)$, and then the theorem is proved.

Chapter 4

Performance Analysis and Enhancement of 802.11ad MAC for mmWave Beamforming Training

4.1 Introduction

The mmWave communications, unfortunately, suffer from severe free-space path loss because of the high-frequency band [32]. To compensate for the path loss in mmWave communications, BF technology, which focuses the radio frequency power in a narrow direction, is adopted at both the transmitter and receiver. Since reliable communication is only possible when the BF of both the transmitter and receiver are properly aligned, a *BF training* procedure between transmitter and receiver is required. Without BF training, the data rate of mmWave WLAN drops from several Gbps to only a few hundred Mbps [22]. Hence, research on finding an efficient BF training scheme is imperative for mmWave networks.

Most recent works study efficient BF training schemes, such as codebook-based beam search [53], compressed sensing schemes [71], and out-of-band solutions [51]. Although existing works can significantly improve the efficiency of BF training, they mainly consider the BF training performance from the physical layer's perspective. However, the contention feature of MAC layer is seldom considered, i.e., the multiple stations (STAs[1]) compete for the same BF training time. Even with efficient BF training schemes, a coarse MAC would

[1]To keep consistent with the BFT-MAC protocol in 802.11ad, we use "STA" to represent a user in this chapter.

result in severe collisions for BF training, which wastes the cherished BF training time and incurs extra BF training latency. Hence, the elaborate analysis of the MAC protocol for BF training is of paramount importance.

IEEE 802.11ad specifies a new distributed BF training MAC (BFT-MAC) protocol for the BF training coordination among multiple STAs. Specifically, the BF training duration is divided into several associated beamforming training (A-BFT) slots, and all STAs will contend for these A-BFT slots in a contention and backoff manner. However, the performance of BFT-MAC in dense user scenarios is still unclear. The reason is two-fold. Firstly, due to the "deafness" problem caused by BF, i.e., an STA may not sense the transmission of other STAs, BFT-MAC is different from traditional carrier sensing based MAC protocols. Hence, existing analytical models for traditional microwave WLANs are unsuitable for BFT-MAC. Secondly, previous work in [52] simulate the MAC performance with a finite number of STAs and can hardly provide theoretical insights for dense user scenarios. Thus, we argue that a thorough theoretical framework on BFT-MAC is necessary and significant. Moreover, 802.11ad only provides at most eight A-BFT slots, and hence the collision probability is high in dense user scenarios, which results in low throughput and high BF training latency. Thus, an enhancement scheme on 802.11ad is required to improve the performance in dense user scenarios.

In this study, we focus on the performance of BFT-MAC. Specifically, we target at answering the following questions: *1) How good the performance of BFT-MAC is; 2) How to further enhance the performance of BFT-MAC in dense user scenarios?* Firstly, to evaluate the BFT-MAC performance, a two-dimensional Markov chain *analytical model* which models the number of consecutive collisions and the backoff time as a state, is developed. Our analytical model unveils the impact of the number of A-BFT slots, the number of STAs and MAC parameters on the BFT-MAC performance. Secondly, based on the analytical model, the closed-form expressions of normalized throughput and BF training latency are derived, respectively. Furthermore, asymptotic analysis in dense user scenarios demonstrates that the normalized throughput depends on the ratio between the number of STAs and the number of A-BFT slots. Particularly, the *maximum normalized throughput* is barely $1/e$, which is the same as slotted ALOHA. Finally, since the performance substantially degrades in dense user scenarios due to the limitation of A-BFT slots in practical systems, an *enhancement scheme* which adaptively adjusts MAC parameters according to the user density, is proposed to improve MAC performance. Extensive simulations are carried out and demonstrate that the enhancement scheme can significantly improve the normalized throughput and reduce the BF training latency, as compared to 802.11ad with the default parameter setting. The main contributions in this study are summarized as follows:

- We propose an analytical model to evaluate the performance of BFT-MAC. Extensive simulation results validate the accuracy of the proposed analytical model.
- We derive closed-form expressions of the successful BF training probability, normalized throughput and average BF training latency based on the proposed analytical model. Asymptotic analysis indicates that the maximum normalized throughput is barely $1/e$.
- We propose an enhancement scheme which adjusts MAC parameters in tune with the user density to improve the MAC performance in dense user scenarios.

The remainder of this chapter is organized as follows. Related work is reviewed in Section 4.2. An overview of BF training in 802.11ad is presented in Section 4.3. The proposed analytical model and the corresponding performance analysis are given in Section 4.4. Section 4.5 provides asymptotic analysis on the normalized throughput. Then, Section 4.6 proposes an enhancement scheme in dense user scenarios. In Section 4.7, extensive simulations are conducted to validate the proposed analytical model and the enhancement scheme. In Section 4.8, concluding remarks are given.

4.2 Literature Review

There are extensive research efforts on designing efficient BF training schemes [49,51,53,71]. A codebook-based search scheme is proposed in [53], in which beamwidth is adjusted in each step until the optimal beam is identified. Marzi *et al.* developed a compressed sensing based BF training method with low-complexity by exploiting the sparse characteristic of mmWave channels [71]. Some out-of-band schemes, which exploits traditional Wi-Fi signals to reduce BF training overhead, were developed in [51]. In another line of research, Hassanieh *et al.* proposed a fast BF training scheme by utilizing the multi-armed beam feature of directional antennas [49]. While the aforementioned works can enhance the efficiency of BF training, they lack of the considerations of the contentions of multiple STAs in the BF training protocol. In contrast, our work focuses on investigating the performance of BF training from the MAC layer's perspective.

The MAC performance has been extensively investigated in [72–77]. Inspired by the celebrated Bianchi's model [72], MAC protocols in traditional microwave systems have been analyzed in various networks and scenarios, such as highly mobile vehicular network [73,74], mobile ad hoc network [75], Internet-of-things network [76] and wireless body area network (WBAN) [77]. Luan *et al.* developed a pioneering three-dimensional Markov

chain analytical model to investigate the performance of 802.11 DCF in the drive-through Internet [73]. An extended work investigated the throughput performance of the drive-through Internet taking practical access procedures into consideration [74]. Another work considered the impact of interference and developed an analytical model to analyze the MAC performance in WBANs [77]. While the works in [72–77] shed insightful lights on the MAC performance in microwave systems, they solely focus on the omni-directional system. However, since 802.11ad WLANs are directional systems due to the adoption of BF technology, the legacy of MAC analytical models in omni-directional systems cannot be applied. Several recent works devoted to analyzing the MAC performance in 802.11ad WLANs. The impact of the number of sectors in the directional transmission is analyzed in [78]. A directional cooperative MAC protocol is proposed and analyzed in [79]. However, these works [78, 79] mainly focus on the MAC performance in the data transmission stage. In contrast, our work considers the MAC performance in the BF training stage, which is the bottleneck of the whole system.

On the other hand, some research works in [52, 80–83] are devoted to enhancing the MAC performance in the BF training stage. To alleviate collisions of BF training in dense user scenarios, a pioneering work [52] proposed a secondary backoff scheme in the A-BFT stage. Each STA selects not only a backoff A-BFT slot, but also a secondary backoff time within the A-BFT slot such that transmission collisions can be reduced. Leveraging the channel sparsity in the mmWave channel, Shao *et al.* developed a compressed sensing method of performing BF training simultaneously for a group of STAs in [80]. In addition, there are multiple standardization efforts on enhancing the MAC performance of BF training. Kim *et al.* in [81] spread out the access attempt over time to cope with the high collision issue in dense user networks. Another draft in [82] allowed BF training simultaneously for different STAs over multiple channels to enhance BF training, which may increase the protocol signaling overhead. Jo *et al.* proposed a short sector sweep (SSW) frame structure in [83] which has a shorter packet length compared with a SSW frame, to increase the BF training capability in an A-BFT slot. Although these works provide efficient solutions on enhancing MAC performance for BF training, they more or less need to modify the protocol and hence may be incompatible with current 802.11ad. In contrast to these works, rather than proposing new MAC schemes with distinguished features, we target on an in-depth understanding of the 802.11ad MAC protocol for BF training. The reason is two-fold. Firstly, 802.11ad is the most practical and adopted standard in mmWave WLANs, which is widely used in many COTS mmWave devices. Secondly, ongoing 802.11ay is expected to adopt a similar MAC protocol for BF training as 802.11ad, with an increased number of A-BFT slots [33]. As such, our analytical model can be easily extended to study the performance of 802.11ay.

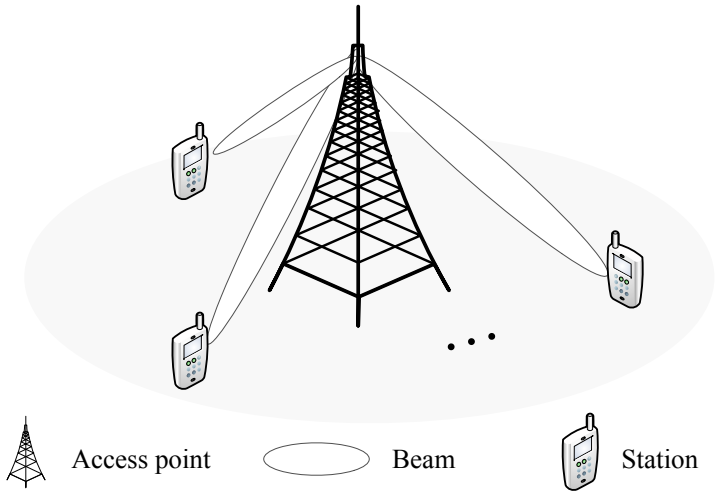

Fig. 4.1: A 802.11ad network topology.

4.3 BF Training in 802.11ad

This section first presents the BF training procedure in 802.11ad, and then details BFT-MAC.

4.3.1 BF Training

We consider a WLAN network compliant with the 802.11ad standard, consisting of an access point (AP) and multiple STAs, as shown in Fig. 4.1. The AP coordinates the BF training, link scheduling and network synchronization in the network. Both AP and STAs adopt the directional multi-gigabit mode, i.e., each node is equipped with an electrically steerable directional antenna capable of supporting the directional transmission.

To establish reliable mmWave communication links, an STA should perform BF training with AP at the beginning of each beacon interval (BI). As depicted in Fig. 4.2, the transmission time is partitioned into multiple BIs. Each BI is further segregated into (1) beacon transmission interval (BTI), during which AP performs the BF training with STA; (2) A-BFT, during which all STAs contend for BF training with AP; (3) announcement transmission intervals (ATI), which coordinates the transmission scheduling in data transmission interval (DTI); (4) DTI, which facilitates directional data transmission [11]. Our study focuses on the BF training in the A-BFT. A-BFT is further divided into multiple

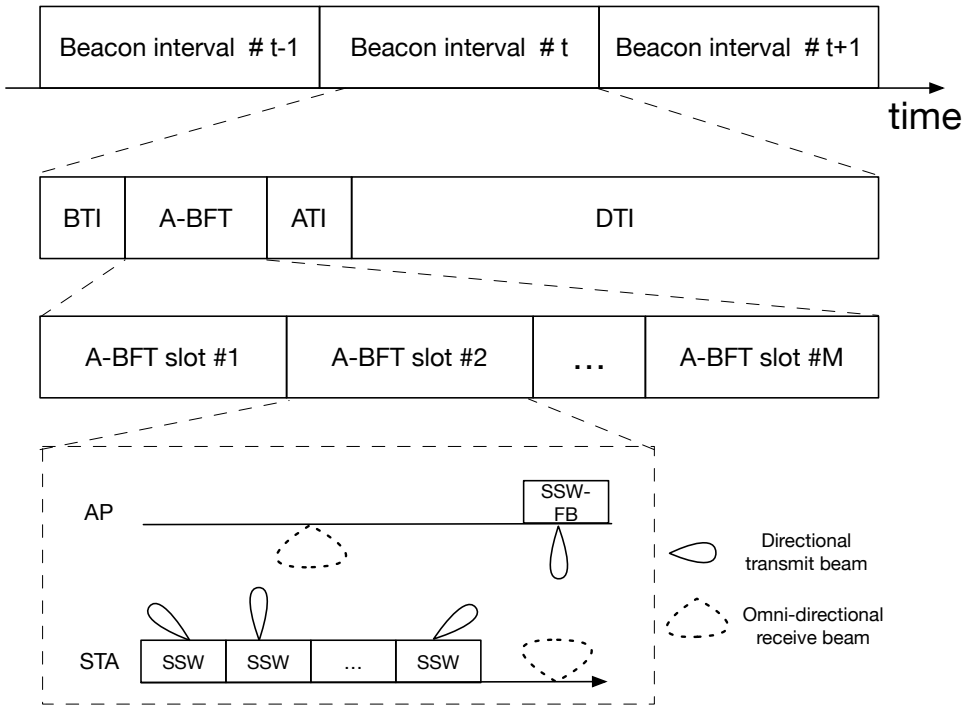

Fig. 4.2: The 802.11ad beacon interval format and an illustration of BF training.

A-BFT slots to provide separated BF training for different STAs. Specifically, the BF training procedure between AP and an STA in an A-BFT slot is illustrated in Fig. 4.2. An STA transmits multiple SSW frames via different directional beams, and AP receives these SSW frames via the omni-directional beam. Based on the received signal strength of these directional beams, AP can identify the best transmit beam of the STA. Subsequently, the AP sends an SSW-feedback (SSW-FB) frame to the STA for the acknowledgment of a *successful BF training*. Note that an A-BFT slot can only provide a BF training opportunity for an STA. If two STAs compete for the same A-BFT slot, a *collision* occurs. As such, no SSW-FB frame would be sent to STAs, and then the transmitting STAs are aware of the occurrence of the collision.

Note that above mentioned BF training in A-BFT is a part of the entire BF training procedure in 802.11ad. As we focus on the performance of BF training from the perspective of the MAC layer, the detailed BF training procedure is beyond the scope of our study. For more details, one can refer to a detailed review in [84].

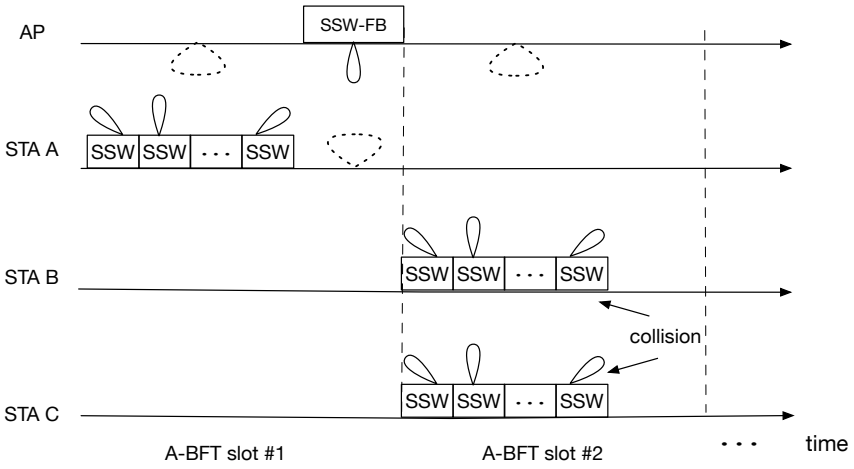

Fig. 4.3: Illustration of BFT-MAC in A-BFT. The BF training in the A-BFT slots #1 is successful, while that in A-BFT slot #2 is unsuccessful since this A-BFT slot is selected by two STAs simultaneously.

4.3.2 802.11ad BFT-MAC Protocol

To coordinate BF training for multiple STAs, 802.11ad specifies a distributed BF training MAC protocol, namely, BFT-MAC, in which each STA performs BF training with AP in a contention and backoff manner. The BFT-MAC protocol consists of the following two steps:

- Before BF training, each *active STA* randomly selects an A-BFT slot from the range $[1, M]$ for the transmission of BF training packets (referred to as a transmission for short hereinafter). Here, M denotes the number of A-BFT slots. A successful BF training depends on whether an A-BFT slot is selected by multiple STAs. If an A-BFT slot is only selected by one STA, the transmission would be successful, and an SSW-FB frame would be sent back from the AP. As shown in Fig. 4.3, the BF training of *STA A* in the A-BFT slot #1 is successful since this A-BFT slot is not selected by any other STAs. Otherwise, if more than one STA select the same A-BFT slot, a collision would occur, and no SSW-FB would be sent back from AP, such as *STA B* and *STA C* in Fig. 4.3.

- After BF training, if the number of consecutive collisions of an STA exceeds the retry limit R (referred to as *dot11RSSRetryLimit* in 802.11ad), the STA would uniformly select a discrete backoff time w from the range $[0, W)$. Here, W denotes the contention

Table 4.1: Summary of notations in BF training MAC.

Notation	Description
p	Conditional collision probability
p_s	Conditional successful transmission probability
τ	The probability that an STA is active
$C(t)$	Consecutive collision counter at time t
$B(t)$	Backoff time at time t
(r, w)	State with r consecutive collisions and w backoff time
M	Number of A-BFT slots
R	Retry limit
D	Average BF training latency
W	Contention window
S	Normalized throughput
$\boldsymbol{\pi}$	Steady state probability vector
T_{BI}	Duration of a beacon interval
T_{SSW}	Duration of a sector sweep frame
$\mathbb{Z}^+$	Positive integer set
F	Number of SSW frames in an A-BFT slot

window (referred to as *dot11RSSBackoff* in 802.11ad). Specifically, each STA maintains a consecutive collision counter (referred to as *FailedRSSAttempts* in 802.11ad) which indicates the number of consecutive collisions that the STA has experienced in A-BFT. Once a collision occurs, the consecutive collision counter is incremented by one. Otherwise, upon a successful transmission, the consecutive collision counter is cleared to zero.

Note that STAs can only transmit when the backoff time is zero. The backoff time is decremented by one after one BI. Thus, if the backoff time of an STA is w, the STA has to be frozen from transmission in the subsequent w BIs. Due to the backoff mechanism, not all STAs are contending for A-BFT slots. We refer to STAs that are contending as *active STAs*, while other STAs whose backoff times are nonzero, are called *inactive STAs*.

The advantages of 802.11ad BFT-MAC is salient. Firstly, BFT-MAC is fully distributed which is scalable with the network size. Secondly, the MAC protocol is simple which can be easily implemented under different scenarios. However, compared with the celebrated DCF protocol in traditional omni-directional WLANs, the absence of carrier sensing mechanism makes BFT-MAC susceptible to collide, especially in dense user scenarios. In what follows, we analyze the performance of BFT-MAC.

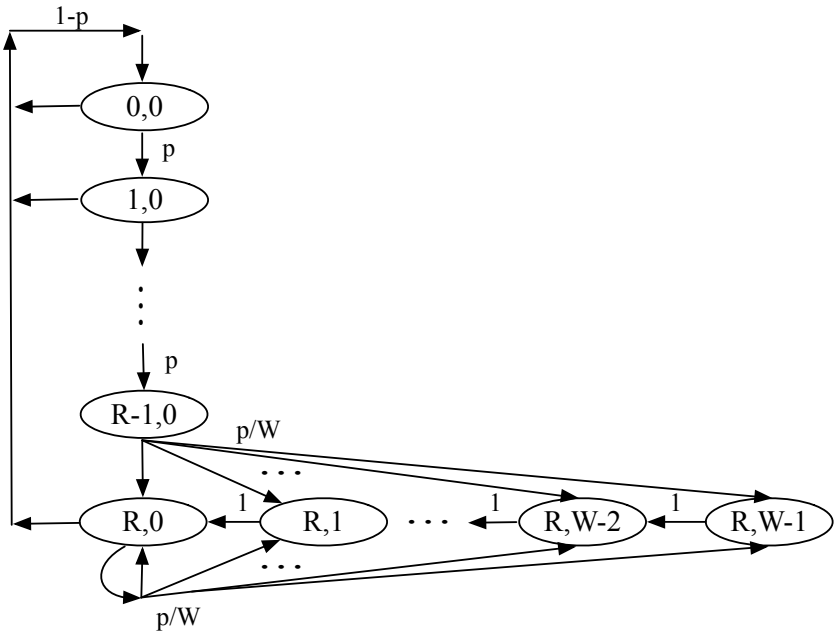

Fig. 4.4: Two-dimensional Markov model for BFT-MAC.

4.4 System Model and Performance Analysis

In this section, we first develop a two-dimensional Markov chain analytical model for 802.11ad BFT-MAC. Next, the average successful BF training probability and average BF training latency are derived. In the following analysis, we assume a fixed number of STAs and perfect physical channel conditions (i.e., no transmission errors) in the network. Besides, we consider the *saturation condition* in which each STA always needs to perform BF training at each BI [52, 72, 73]. This assumption is reasonable in dynamic mmWave networks. Since the established communication connections are intermittent and short-lived due to the mobility and blockage, the BF training procedure would be invoked persistently. For better illustration, a summary of important notations is given in Table 4.1.

4.4.1 Markov Model for BFT-MAC

We consider a discrete time slotted system, where t denotes the beginning of the t-th BI. To evaluate the performance of BFT-MAC, we examine a tagged STA and represent its status by a two-dimensional Markov chain $\{C(t), B(t)\}$. Let $C(t) \in [0, R]$ denote the number of

consecutive collisions that the tagged STA has experienced. Let $B(t) \in [0, W-1]$ denote the current backoff time of the tagged STA. For example, State (r, w) indicates that the tagged STA has experienced r consecutive collisions and its current backoff time is w.

Let p denote the average collision probability of the tagged STA. Note that p is the *conditional collision probability* since the collision occurs only when the tagged STA is active. Accordingly, $1-p$ denotes the average conditional successful transmission probability. The state transition diagram is depicted in Fig. 4.4, which is governed by the following events and the corresponding one-step transition probabilities.

- Upon a collision, the consecutive collision counter is incremented by one when it does not exceed the retry limit. The STA transits from state $(r, 0)$ to state $(r+1, 0)$, and the corresponding transition probability is given by

$$\mathbb{P}\left(r+1, 0 | r, 0\right) = p, \forall r \in [0, R-2]. \tag{4.1}$$

- Upon a successful transmission, the consecutive collision counter is cleared to zero. The STA transits from state $(r, 0)$ to state $(0, 0)$ with the following transition probability

$$\mathbb{P}\left(0, 0 | r, 0\right) = 1-p, \forall r \in [0, R]. \tag{4.2}$$

- If the consecutive collision counter reaches the retry limit R, the STA randomly selects a backoff time $w \in [0, W-1]$. The STA transits from state $(R-1, 0)$ to backoff state (R, w), and the corresponding the transition probability is

$$\mathbb{P}\left(R, w | R-1, 0\right) = \frac{p}{W}, \forall w \in [0, W-1]. \tag{4.3}$$

  The STA would be frozen from transmission in A-BFT in the subsequent w BIs.

- The backoff time is decremented by one after every BI. An STA transits from state (R, w) to state$(R, w-1)$, and the one step transition probability is given by

$$\mathbb{P}\left(R, w-1 | R, w\right) = 1, \forall w \in [1, W-1]. \tag{4.4}$$

- The consecutive collision counter will not be incremented if it reaches the retry limit. Upon an unsuccessful transmission, an STA transits from state $(R, 0)$ to state (R, w), and the corresponding transition probability is given by

$$\mathbb{P}\left(R, w | R, 0\right) = \frac{p}{W}, \forall w \in [0, W-1]. \tag{4.5}$$

Hence, the STA remains in backoff states for the subsequent w BIs.

Note that states whose backoff times are zero are called *active states*, while the other states are referred to as *inactive states*. Here, the steady probability of state (r, w) is defined as

$$\pi_{r,w} = \lim_{t\to\infty} \mathbb{P}\left(C(t) = r, B(t) = w\right) \tag{4.6}$$

and the corresponding steady state probability of the proposed Markov chain is $\boldsymbol{\pi} = \{\pi_{0,0}, \pi_{1,0}, ..., \pi_{R-1,0}, \pi_{R,0}, \pi_{R,1}, ..., \pi_{R,W-1}\} \in \mathbb{R}^{(R+W)\times 1}$. Let $\mathbf{P} \in \mathbb{R}^{(R+W)\times(R+W)}$ represent the state transition matrix whose nonnull elements are given in (4.1)-(4.5). Mathematically, $\boldsymbol{\pi}$ can be obtained via solving the following balance equations:

$$\mathbf{P}\boldsymbol{\pi} = \boldsymbol{\pi} \tag{4.7a}$$

$$\sum_{r=0}^{R}\sum_{w=0}^{W-1} \pi_{r,w} = 1 \tag{4.7b}$$

where (4.7b) accounts for the fact that the summation of all steady state probabilities equals one.

Note that our model is distinct from the celebrated Bianchi's model [72] in the following two ways. Firstly, STAs will backoff after every collision in Bianchi's model, while in our model STAs only backoff when the consecutive collision counter exceeds the retry limit. Secondly, the contention window size increases with the number of consecutive collisions in Bianchi's model, while the contention window size is fixed in our model.

4.4.2 Successful BF Training Probability

Based on our analytical model, we first derive the closed-from expression of the steady state probability and then obtain the successful BF training probability.

Theorem 3 *The steady state probabilities of the proposed Markov chain can be represented by*

$$\pi_{r,w} = \begin{cases} \dfrac{p^r\left(1-p\right)}{p^R\left(W-1\right)/2+1}, r \in [0, R-1], w = 0 \\ \dfrac{\left(W-w\right)p^R}{W\left(p^R\left(W-1\right)/2+1\right)}, r = R, w \in [0, W-1]. \end{cases} \tag{4.8}$$

Proof. The detailed proof is given in Appendix 4.9.1. □

All steady state probabilities in Theorem 3 are represented by p which is the unknown conditional collision probability. In the following, the value of p will be obtained.

The probability that an STA stays in an active state, is given by

$$\begin{aligned} \tau &= \sum_{r=0}^{R} \pi_{r,0} \\ &= \frac{1}{p^R (W-1)/2 + 1}. \end{aligned} \tag{4.9}$$

From the perspective of the STA, a successful transmission only occurs when other active STAs select other A-BFT slots for transmission or stay in inactive states. Hence, the conditional successful transmission probability, given an STA is active, is

$$\begin{aligned} p_s &= \left(\tau\left(1-\frac{1}{M}\right)+1-\tau\right)^{N-1} \\ &= \left(1-\frac{\tau}{M}\right)^{N-1} \\ &= \left(1-\frac{1}{M\left(p^R (W-1)/2+1\right)}\right)^{N-1}. \end{aligned} \tag{4.10}$$

The last step is obtained from the substitution of (4.9).

Since $p_s + p = 1$, we can obtain the following equation:

$$\left(1-\frac{1}{M\left(p^R (W-1)/2+1\right)}\right)^{N-1} + p - 1 = 0. \tag{4.11}$$

The conditional collision probability p can be obtained via solving (4.11). However, due to the summation and permutation, Eq. (4.11) is an implicit function, and thus it is challenging to obtain a closed-form solution. Here, we apply a numerical method to obtain p. More importantly, Eq. (4.11) demonstrates that the conditional collision probability p depends on the retry limit R, the contention window W, the number of A-BFT slots M and the number of STAs N. Obviously, these parameters are closely coupled with each other, which poses challenges on the further throughput analysis.

With the obtained p, the successful transmission probability can be computed via the following way. Since $1 - p$ represents the conditional successful transmission probability

given the STA is active, the successful transmission probability is represented as follows:

$$\hat{p}_s = (1-p)\,\tau \tag{4.12}$$

which also denotes the successful BF training probability of BFT-MAC.

4.4.3 Average BF Training Latency

In addition to the average successful BF training probability, the BF training latency is also another important performance indicator for BFT-MAC. The average BF training latency represents the average time spent until a successful transmission. Taking the consecutive collisions before a successful transmission into account, the average BF training latency can be represented by

$$\begin{aligned} D &= \sum_{i=0}^{\infty} \mathbb{P}\left(\text{Success}|\text{Collisions} = i\right) \mathbb{E}\left[D_i\right] \\ &= \sum_{i=0}^{\infty} (1-p)\, p^i \mathbb{E}\left[D_i\right] \end{aligned} \tag{4.13}$$

where $\mathbb{E}[D_i]$ represents the BF training latency of a successful transmission after experiencing i consecutive collisions. Note that if the number of consecutive collisions exceeds the retry limit, the STA would be frozen from transmission for a backoff time. Hence, $\mathbb{E}[D_i]$ can be divided into the following two cases based on the number of consecutive collisions:

- When $i < R$, $\mathbb{E}\left[D_i\right]$ can be represented by

$$\begin{aligned} \mathbb{E}\left[D_i\right] &= i \cdot T_{BI} + F \cdot T_{SSW} \\ &= T_{BI}\left(i + \alpha\right) \end{aligned} \tag{4.14}$$

  where $\alpha = F \cdot T_{SSW}/T_{BI}$. Here, T_{BI} and T_{SSW} denote the duration of a BI and an SSW frame, respectively. The first term in (4.14) accounts for the latency caused by i consecutive collisions before a successful transmission. According to BFT-MAC, if a collision occurs, the collided STA must wait until the subsequent BI to initiate a transmission attempt, which increases the latency by an entire BI duration. The second term in (4.14) represents the latency for the successful transmission. As shown in Fig. 4.3, the successful BF training procedure consists of F (referred to as *FSS* field in 802.11ad) SSW frames and the corresponding BF training latency is

$F \cdot T_{SSW}$. With (4.14), the average BF training latency of an STA when the number of consecutive collisions is less than R, is given by

$$\begin{aligned}\sum_{i=0}^{R-1}(1-p)\,p^i\mathbb{E}\left[D_i\right] &= \sum_{i=0}^{R-1}(1-p)\,p^i\,(i+\alpha)\,T_{BI}\\ &= T_{BI}\,(1-p)\left(\sum_{i=0}^{R-1}p^i\cdot i+\alpha\sum_{i=0}^{R-1}p^i\right)\\ &= T_{BI}\left(\frac{p^{R+1}\,(R-1)-Rp^R+p}{1-p}+\left(1-p^R\right)\alpha\right).\end{aligned} \tag{4.15}$$

- When $i \geq R$, each collision results in a further random backoff time of w BIs, and hence $\mathbb{E}\left[D_i\right]$ is given by

$$\begin{aligned}\mathbb{E}\left[D_i\right] &= ((i-R+1)(\mathbb{E}\left[w\right]+1)+R-1)T_{BI}+F\cdot T_{SSW}\\ &= T_{BI}\left((i-R+1)(\mathbb{E}\left[w\right]+1)+R-1+\alpha\right)\end{aligned} \tag{4.16}$$

where $\mathbb{E}\left[w\right]$ denotes the average backoff time. The BF training latency when the number of a consecutive collision exceeds R, can be represented by

$$\begin{aligned}&\sum_{i=R}^{\infty}(1-p)\,p^i\mathbb{E}\left[D_i\right]\\ &= \sum_{i=R}^{\infty}T_{BI}\,(1-p)\,p^i\left((i-R+1)(\mathbb{E}\left[w\right]+1)+R-1+\alpha\right)\\ &\overset{(a)}{=} \sum_{j=0}^{\infty}T_{BI}\,(1-p)\,p^{R+j}\left((j+1)\left(\mathbb{E}\left[w\right]+1\right)+R-1+\alpha\right)\\ &= T_{BI}\,(1-p)\,p^R\left(\left(\mathbb{E}\left[w\right]+1\right)\sum_{j=0}^{\infty}p^j\cdot j+\left(\left(\mathbb{E}\left[w\right]+1\right)+R-1+\alpha\right)\sum_{j=0}^{\infty}p^j\right)\\ &= T_{BI}\cdot p^R\left(\frac{p(\mathbb{E}\left[w\right]+1)}{1-p}+\mathbb{E}\left[w\right]+R+\alpha\right)\\ &\overset{(b)}{=} T_{BI}\cdot p^R\left(\frac{W+1}{2(1-p)}+R+\alpha-1\right)\end{aligned} \tag{4.17}$$

where (a) follows by changing variable $j = i - R$; (b) is due to the substitution of

$\mathbb{E}[w] = (W-1)/2$.

Taking these two cases into consideration, the average BF training latency in (4.13) can be obtained as follows:

$$\begin{aligned} D &= \sum_{i=0}^{R-1} (1-p)\, p^i \mathbb{E}[D_i] + \sum_{i=R}^{\infty} (1-p)\, p^i \mathbb{E}[D_i] \\ &= T_{BI} \left(\frac{p^{R+1}(R-1) - Rp^R + p}{1-p} + \left(1-p^R\right)\alpha \right) + T_{BI} p^R \left(\frac{W+1}{2(1-p)} + R + \alpha - 1 \right) \\ &= T_{BI} \left(\frac{p^R (W-1)/2 + p}{1-p} + a \right). \end{aligned} \tag{4.18}$$

Eq. (4.18) demonstrates that the BF training latency depends on the collision probability p, the retry limit R and the contention window W. Obviously, the BF training latency increases with the increase of the collision probability since severe collisions would result in substantial retransmission in the network.

4.5 Asymptotic Throughput Analysis

4.5.1 Normalized Throughput

Since the average successful transmission probability is $p_s\tau$, the average number of STAs that successfully perform BF training is $p_s\tau N$. The *normalized throughput* of BFT-MAC represents the percentage of A-BFT slots that has been successfully utilized, which is defined as

$$\begin{aligned} S &= \frac{p_s \tau N}{M} \\ &= \left(1 - \frac{\tau}{M}\right)^{N-1} \frac{\tau N}{M} \end{aligned} \tag{4.19}$$

where the last step follows from the substitution of (4.10). Since τ depends on MAC parameters, above equation characterizes the impact of the number of STAs, the number of A-BFT slots and MAC parameters on the MAC throughput.

From (4.19), it is computational complex to obtain the asymptotic MAC throughput in dense user scenarios. This is because (4.19) is a complex function of τ, N, and M.

To make the performance analysis tractable, an approximation of throughput is desired. According to (4.10), for a large number of STAs, the conditional successful transmission probability can be approximated by

$$\begin{aligned}\hat{p}_s &= \left(1-\frac{\tau}{M}\right)^{N-1} \\ &\overset{(a)}{\approx} \left(1-\frac{\tau}{M}\right)^{N} \\ &= \left(\left(1-\frac{\tau}{M}\right)^{M/\tau}\right)^{N\tau/M} \\ &\overset{(b)}{\approx} e^{-N\tau/M}\end{aligned} \tag{4.20}$$

where (a) is obtained when N is sufficiently large. Since we consider dense user scenarios, this condition can be easily satisfied, and hence the approximation is valid; (b) follows from the equation $\lim_{n\to\infty}(1-1/n)^n = 1/e$ where $n = M/\tau$ is sufficiently large in dense user scenarios. Here, (4.20) demonstrates the average successful transmission probability is dependent on N/M.

Substituting (4.20) into (4.19), the *asymptotic normalized throughput* when the number of STAs is sufficiently large, can be given as follows:

$$\hat{S} = \frac{\tau N}{M} e^{-\tau N/M}. \tag{4.21}$$

Eq. (4.21) characterizes the asymptotic throughput performance with respect to system parameters and provides the following important insights for MAC design in dense user scenarios. Firstly, the normalized throughput in dense user scenarios depends on the ratio between the number of STAs and the number of A-BFT slots, i.e., N/M. Therefore, increasing the number of A-BFT slots adaptive to the number of STAs is an effective solution to maintain excellent performance. Secondly, with a further analysis of (4.21), the throughput increases with $\tau N/M$ when it is less than 1 while decreases with $\tau N/M$ when it exceeds 1. For a practical system with a fixed number of A-BFT slots, the throughput would decrease with the increase of user density in dense user scenarios. Thirdly, since τ is determined by the MAC parameters, the throughput is also affected by the MAC parameters. Thus, we can conclude that the default MAC parameter setting is not always optimal in different user density scenarios, which implies that the MAC parameters should be tuned according to user density. The accuracy of this approximation is validated by extensive simulation results in Fig. 4.9.

4.5.2 Maximum Normalized Throughput

With the asymptotic normalized throughput, we target at analyzing the *maximum normalized throughput* in dense user scenarios. Since the number of STAs in the network is uncontrollable, the number of A-BFT slots can be optimized with respect to the number of STAs to maximize the normalized throughput. Here, we assume the number of A-BFT slots is sufficient. The problem with limitation of A-BFT slots will be discussed in the following section. The normalized throughput maximization problem can be formulated as follows:

$$\begin{aligned} \mathcal{P}2: \max_{M} \quad & \hat{S} \\ \text{s.t.} \quad & M \in \mathbb{Z}^{+}. \end{aligned} \tag{4.22}$$

The constraint indicates that the number of A-BFT slots takes positive integers. Hence, problem (4.22) is an integer programming problem. To solve this problem, we first relax the integer constraint to a non-integer constraint. Then, this optimization problem can be readily solved by taking the derivation of (4.21), and the condition to achieve the maximum normalized throughput is given by

$$M^{\star} = \tau N. \tag{4.23}$$

The condition (4.23) provides an interesting insight on the MAC design, i.e., in order to maximize the normalized throughput, the number of A-BFT slots should equal the number of active STAs (τN) in the network. In other words, the network should provide equivalent A-BFT slots for all active users.

Under the condition in (4.23), the maximum normalized throughput is

$$\hat{S}^{\star} = e^{-1} \tag{4.24}$$

which is the same as that of slotted ALOHA.

Since τ depends on the MAC parameters, the optimal number of A-BFT slots is also dependent on the MAC parameters. When the condition in (4.23) is satisfied, we have $p = 1 - 1/e$ because of (4.20). Then, according to (4.9), (4.23) can be rewritten as

$$M^{\star} = \frac{N}{\left(1 - e^{-1}\right)^{R} \left(W - 1\right)/2 + 1}. \tag{4.25}$$

which characterizes the relationship between the optimal number of A-BFT slots and MAC parameters R and W. With a further analysis of (4.25), the optimal number of A-BFT

slots decreases with the decrease of R and the increase of W. To achieve the maximum throughput with limited A-BFT slots, we should choose a small value of R and a large value of W. The detailed optimization of MAC parameters is given in Section 4.6.

Remark 4 *Asymptotic analysis reveals useful insights onto the performance of BFT-MAC. Firstly, the maximum normalized throughput achieved by BFT-MAC is only* $1/e$*, which is the same as that of slotted ALOHA. The normalized throughput is low because the absence of carrier sensing mechanism results in severe collisions for BF training. Secondly, to achieve the maximum throughput, the optimal number of A-BFT slots should equal the number of active STAs in the network. Thus, the mismatch between the active STAs and A-BFT slots renders the throughput degradation.*

4.6 Enhancement Scheme

In this section, we propose an enhancement scheme to improve MAC performance in dense user scenarios. Previous analysis indicates that the normalized throughput depends on the ratio between the number of STAs and the number of A-BFT slots. However, the number of A-BFT slots in practical mmWave WLANs is limited. For example, 802.11ad only provides at most 8 A-BFT slots for BF training. Even though future 802.11ay increases the number of A-BFT slots to 40, the number of A-BFT slots is still limited [33]. Thus, in dense user scenarios, the limitation of A-BFT slots renders the throughput degradation.

To improve the throughput in dense user networks, we propose an *enhancement scheme* that MAC parameters R and W should be tuned with the user density in the network. The reasoning behind the enhancement scheme is that adjusting MAC parameters can determine the probability that STAs are active (τ) such that the number of active STAs could be equivalent to the number of provided A-BFT slots. This reason is also validated by our analytical results. Since $\tau = 1/(p^R (W-1)/2 + 1)$ in (4.9), τ decreases with the decrease of R, i.e., a small value of the retry limit renders that STAs are prone to enter backoff states and thus reduces the number of active STAs in the network. In addition, τ also decreases with the decrease of W, because large contention window size makes STAs keep inactive for a longer time. Therefore, adaptively adjusting MAC parameters in tune with user density is an effective solution in dense user scenarios.

The proposed enhancement scheme mainly consists of two steps. Firstly, AP obtains the number of STAs in the network. Secondly, based on the number of STAs in the network, AP configures the optimal parameter setting of BFT-MAC and broadcasts the

MAC parameters (the retry limit and the contention window) to all STAs in the network. The key issue of the enhancement scheme is the optimal MAC parameters, which could be obtained by solving the following optimization problem with the objective to maximize the normalized throughput:

$$\begin{aligned} \mathcal{P}3: \max_{R,W} \quad & S \\ \text{s.t.} \quad & 1 \leq W \leq W_{max}, W \in \mathbb{Z}^+ && \text{(4.26a)} \\ & 1 \leq R \leq R_{max}, R \in \mathbb{Z}^+ && \text{(4.26b)} \end{aligned}$$

where W_{max} denotes the maximum contention window size, which is applied to avoid infinite backoff time. Here, R_{max} denotes the maximum value of the retry limit.

The problem is challenging to be solved due to the following two reasons. Firstly, the optimization variables obey integer constraints. Secondly, the objective function is non-convex. This is because S is an implicit function with respect to R and W, since two variables R and W are coupled with each other according to (4.11). Therefore, problem $\mathcal{P}3$ is a mix-integer non-convex problem, which is difficult to obtain the optimal solution. However, because the number of possible combinations of the MAC parameters is limited, we can solve this problem via an exhaustive search method [73]. The computational complexity of the exhaustive search method is $O(W_{max}R_{max})$. In addition, to reduce computational time, the optimal parameter setting can be computed offline with different numbers of STAs and loaded into AP as a table. Then, based on the number of STAs in the coverage of AP, the AP could search the table to obtain the optimal MAC parameters with low complexity.

4.7 Simulation Results

In this section, we evaluate the proposed analytical model and the enhancement scheme via extensive Monte-Carlo simulations.

4.7.1 Simulation Setup

We validate the proposed analytical model based on a discrete event simulator coded in Matlab. We consider an 802.11ad system which operates in the unlicensed 60 GHz band.

Table 4.2: Simulation parameters in BF training MAC.

Parameter	**Value**
BI duration (T_{BI})	100 ms
SSW frame duration (T_{SSW})	15.8 us
Number of STAs (N)	[8,32]
Number of A-BFT slots (M)	8
Default retry limit (R)	8
Default contention window (W)	8
Number of SSW frames in an A-BFT slot (F)	16
Frequency band	60 GHz
Maximum retry limit (R_{max})	10
Maximum contention window (W_{max})	10

Specifically, we simulate 10,000 BIs and study the statistics of interests. Unless otherwise specified, we set $M = 8$, $W = 8$ and $R = 8$ based on the default configuration of the 802.11ad standard [11]. Other important simulation parameters are listed in Table 4.2. For each experiment, we conduct 1000 simulation runs and plot a 95 percent confidence interval for each simulation point.

4.7.2 Analytical Model Validation

As shown in Fig. 4.5, we first observe the successful BF training probability in terms of the number of STAs for $M = 8, 12, 16$. It is evident that the results obtained via our analytical model are highly consistent with that via simulations, which validates the accuracy of our analytical model. As expected, we can see a lower successful BF training probability in denser user scenarios since more STAs contend for limited A-BFT slots. The successful BF training probability drops from more than 80% to less than 20% as the number of STAs increases from 4 to 32. Moreover, as the number of A-BFT slots (M) increases, the successful BF training probability increases because more A-BFT slots are provided. The results validate that the successful BF training probability mainly depends on the numbers of STAs and A-BFT slots.

In Fig. 4.6, we further show the normalized throughput with respect to the number of STAs. Several important observations can be made. Firstly, simulation results are closely matched with analytical results, which further validates our analytical model. Secondly, the normalized throughput exhibits a bell-shape behavior. The reason is two-fold: a) many A-BFT slots are not utilized in low user density scenarios; a) severe collision occurs in high

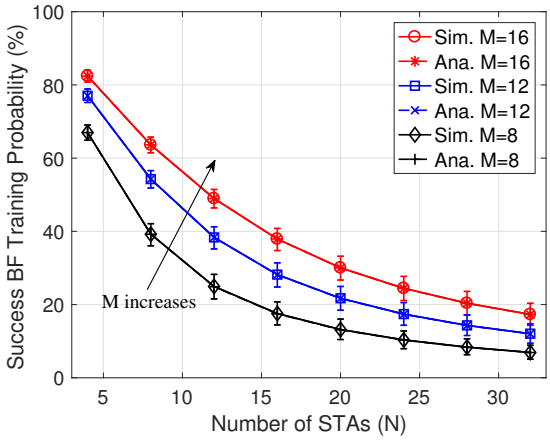

Fig. 4.5: Successful BF training probability in terms of the number of STAs.

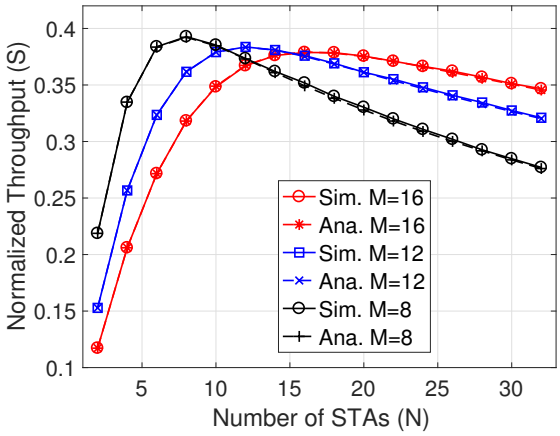

Fig. 4.6: Normalized throughput with respect to the number of STAs.

user density scenarios, which results in a low throughput. Thus, to achieve the maximum normalized throughput, the number of A-BFT slots should be cautiously selected. Thirdly, it is interesting to note that a system with more A-BFT slots achieves a higher normalized throughput than that with fewer A-BFT slots. For example, in a dense user scenario ($N = 32$), the normalized throughput for $M = 16$ is 25% more than that for $M = 8$. This is because more A-BFT slots can effectively alleviate the collision issue in dense user scenarios. Finally, we can observe the maximum normalize throughput is around $1/e$ (0.37), which complies with our analytical results.

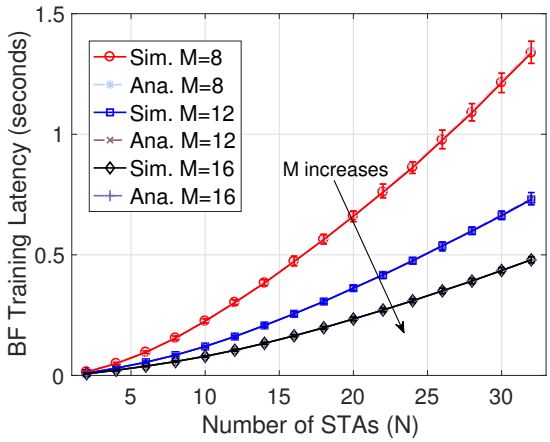

Fig. 4.7: Average BF training latency with different numbers of STAs.

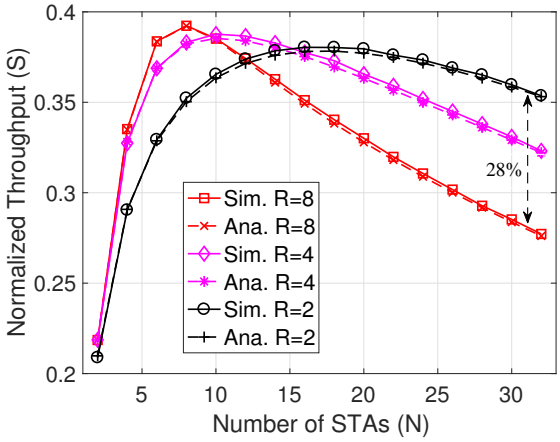

Fig. 4.8: Normalized throughput with different values of the retry limit.

Figure 4.7 shows the impact of the number of STAs on the average BF training latency. It can be observed that simulation results comply with our analytical results in (4.18). Clearly, the BF training latency increases with the number of STAs. This is because STAs suffer from severe collisions in dense user scenarios which results in a large amount of retransmission. Moreover, the average BF training latency decreases as the number of A-BFT slots increases. Specifically,when $N = 32$, the average BF training latency for $M = 8$ is up to 1.3 seconds, which is 150% more than that for $M = 16$. Hence, increasing the number of A-BFT slots can reduce the BF training latency.

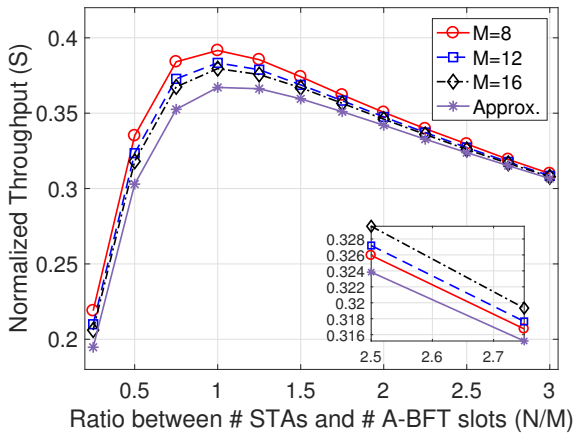

Fig. 4.9: Normalized throughput with respect to different ratios between the number of STAs and the number of A-BFT slots.

Figure 4.8 plots the impact of the value of the retry limit on the normalized throughput. The normalized throughput of BFT-MAC varies with different values of retry limit. Specifically, in dense user scenarios, BFT-MAC with a small value of the retry limit achieves a higher throughput than that with a larger value of retry limit. For example, when $N = 32$, BFT-MAC for $R = 2$ achieves around 28% throughput gain as compared to that for $R = 8$. The reason is that a small value of the retry limit renders STAs are susceptible to enter the backoff states. As such, fewer active STAs will contend for the A-BFT slots, thereby enhancing the performance in dense user scenarios. Since $R = 8$ is the default configuration of the retry limit, we claim that the default MAC configuration is not optimal in dense user scenarios. Thus, adaptively adjusting MAC parameters in tune with the user density is a potential solution to improve MAC performance.

As plotted in Fig. 4.9, we investigate the normalized throughput in terms of the ratio between the number of STAs and the number of A-BFT slots. The normalized throughput with the same ratio for different numbers of A-BFTs and STAs are quite close. The results validate our asymptotic analysis result that the MAC throughput mainly depends on the ratio between contending STAs and the provided A-BFT slots. Besides, as M increases, the gap between simulation results and our approximation in (4.21) narrows. The gap can be ignored in dense user scenarios (i.e., the ratio is larger than 2), which validates the accuracy of our approximation.

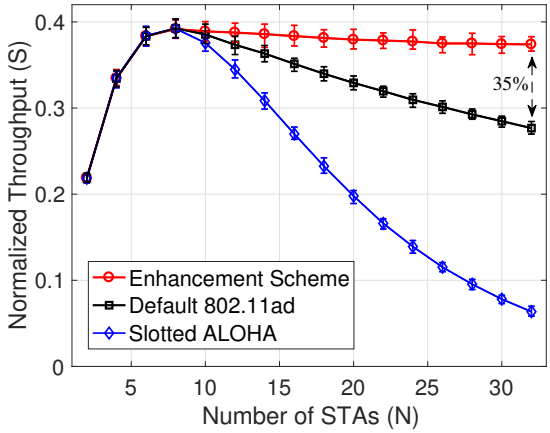

(a) M=8

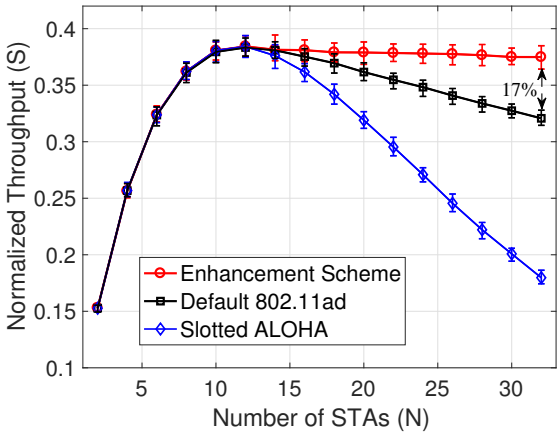

(b) M=12

Fig. 4.10: Normalized throughput comparison in terms of different system parameters.

4.7.3 Enhancement Scheme Evaluation

In this subsection, we evaluate the performance of the proposed enhancement scheme by comparing with two benchmarks: 1) default 802.11ad BFT-MAC protocol, in which both R and W adopt default configurations; 2) slotted ALOHA protocol, where each STA randomly selects an A-BFT slot for BF training without a backoff mechanism.

We first compare the normalized throughput of the proposed enhancement scheme with

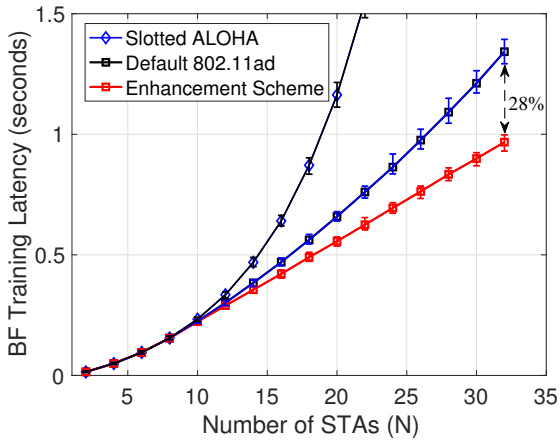

(a) M=8

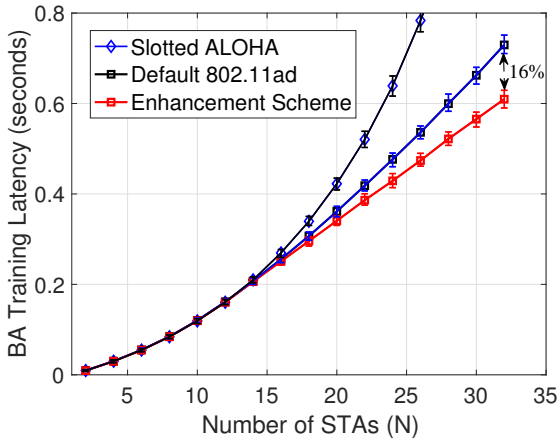

(b) M=12

Fig. 4.11: Average BF training latency comparison in terms of different system parameters.

other two benchmarks in Fig. 4.10. Several important observations can be obtained from simulation results. Firstly, the proposed enhancement scheme can significantly enhance the normalized throughput in dense user scenarios as compared to the benchmarks, which is presented in Fig. 4.10(a). Specifically, we show that a 35% performance gain can be achieved when $N = 32$, which demonstrates the effectiveness of the proposed enhancement scheme. The key reason is that the proposed scheme can adjust MAC parameters in tune with user density to achieve the best performance. Secondly, it is worth noting that all

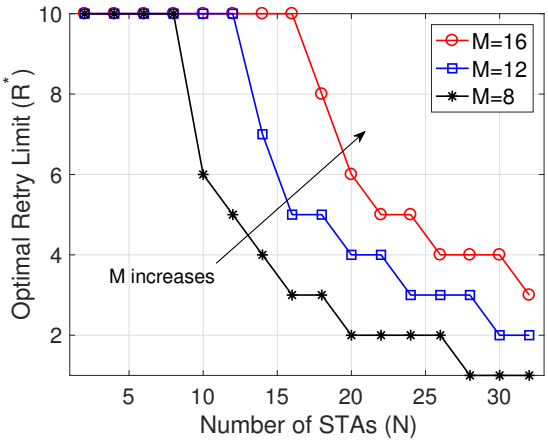

Fig. 4.12: The optimal value of the retry limit in terms of the number of STAs.

three schemes achieve nearly the same performance in low user density scenarios. This is because the key difference between three schemes is the backoff mechanism which mainly works in dense user scenarios. Thirdly, the performance gain decreases as the number of A-BFT slots increases. As reported in Fig. 4.10(b) for $M = 12$, the proposed enhancement scheme only achieves 17% performance gain as compared to the default 802.11ad. Hence, simulation results show that the proposed enhancement scheme is more suitable for dense user scenarios.

We then present the average BF training latency comparison between the proposed scheme and benchmarks for $M = 8, 12$, as shown in Fig. 4.11. The average BF training latency of all three schemes increases with the number of STAs because of the increase of the collision probability. The slotted ALOHA protocol suffers from severe latency as compared to other two schemes. The reason can be explained as follows: the slotted ALOHA lacks a backoff mechanism and hence all STAs always stay active, which results in a higher collision probability and a longer delay. As compared to the default 802.11ad, the proposed scheme can achieve a considerable latency reduction. Specifically, for a large number of STAs ($N = 32$), a 28% performance gain can be observed clearly in Fig. 4.11(a). Similar to the normalized throughput, as the number of A-BFT slots grows, the performance gain of the average BF training latency drops because the increase of A-BFT slots relieves the collision. As shown in Fig. 4.11(b), for $M = 12$, the proposed scheme can still obtain a 16% latency reduction when $N = 32$, which further validates the effectiveness of the proposed scheme. Although the BF training latency can be reduced via adjusting MAC parameters, the latency is still up to hundreds of milliseconds in dense user scenarios.

Finally, Fig. 4.12 plots the optimal values of the retry limit with respect to the number of STAs for $M = 8, 12, 16$. Obviously, the optimal value of the retry limit decreases with the number of STAs. The simulation results show that a small value of retry limit is preferred in dense user scenarios. For example, for $M = 8$, the optimal value of the retry limit is decreased to 1 when the number of STAs is larger than 28. The reason is that a small value of the retry limit in dense user scenarios renders that STAs are prone to enter backoff states. Then, the collision probability is reduced to enhance the normalized throughput. In addition, with the increase of A-BFT slots, the network becomes less congested, and hence a larger value of the retry limit should be chosen. For instance, when $N = 32$, the optimal retry limit value is 3 for $M = 16$, which is larger than that for $M = 8$.

4.8 Summary

In this chapter, we have investigated the performance of 802.11ad BFT-MAC. An accurate analytical model has been proposed to analyze the performance of BFT-MAC, which is validated by extensive simulation results. Based on the analytical model, asymptotic analysis has demonstrated that the maximum normalized throughput is barely $1/e$. Since 802.11ay is expected to adopt a similar MAC protocol for BF training, the proposed analytical model can be readily extended to future 802.11ay systems. Furthermore, to enhance the performance in dense user scenarios, we have proposed an enhancement scheme which can effectively improve the normalized throughput and reduce the BA training latency.

4.9 Appendix

4.9.1 Proof of Theorem 3

Based on the proposed analytical model, the steady state probability vector can be solved with the following three steps.

Firstly, with the one-step transition probability in (4.1), we know that $\pi_{r+1,0} = p \cdot \pi_{r,0}, \forall r \in [0, R-2]$. Hence, the steady state probability at state $(R-1, 0)$ can be represented by

$$\pi_{R-1,0} = p^{R-1}\pi_{0,0}. \tag{4.27}$$

Secondly, with the one-step transition probability in backoff states (4.3)-(4.5), the

steady probability for backoff states can be given as follows:

$$\pi_{R,w} = \frac{(W-w)\,p}{W}\left(\pi_{R,0} + \pi_{R-1,0}\right), \forall w \in [0, W-1]. \tag{4.28}$$

Specifically, it can be obtained that $\pi_{R,0} = \frac{p}{1-p}\pi_{R-1,0}$ by taking $w = 0$ in (4.28). Thus, according to (4.27), (4.28) can be rewritten as

$$\begin{aligned} \pi_{R,w} &= \frac{(W-w)\,p}{W\,(1-p)}\pi_{R-1,0} \\ &= \frac{(W-w)\,p^R}{W\,(1-p)}\pi_{0,0}, \forall w \in [0, W-1]. \end{aligned} \tag{4.29}$$

Finally, substituting (4.27) and (4.29) into (4.7b), $\pi_{0,0}$ can be solved as

$$\pi_{0,0} = \frac{(1-p)}{p^R\,(W-1)/2 + 1}. \tag{4.30}$$

Since other steady state probabilities can be represented by $\pi_{0,0}$, as shown in (4.27) and (4.29), Theorem 3 is proved.

Chapter 5

D2D-assisted Cooperative Edge Caching for mmWave Dense Networks

5.1 Introduction

The proliferation of ever-increasing data-intensive wireless applications, such as virtual reality, augmented reality gaming, and high-definition video streaming, are expected to drastically strain the capacity of cellular networks in the foreseeable future [16, 85]. To accommodate the surging demands of wireless data traffic, mmWave communication, which is a de-facto candidate technology for on-going 5G networks, is envisaged to provide a pseudo-wire wireless connection service by exploiting a large swath of spectrum resource [37, 86]. Leveraging high-gain directional antennas, current mmWave networks offer an extremely high data rate of nearly 7 Gbit/s, which is expected to increase to 40 Gbit/s in the forthcoming future. As mmWave networks can be further densified due to the hostile propagation characteristics, deploying unconstrained wired backhaul links in dense networks becomes infeasible due to high costs, which results in backhaul congestion. Alleviating backhaul pressure is imperative for mmWave dense networks in the future.

Edge caching, which exploits the repetitive pattern of content requests in mobile applications, is a favorable solution to achieve this goal [87, 88]. Specifically, popular contents can be cached in the small base station (SBS) during off-peak hours to serve users in proximity during peak hours, which has a potential to reduce up to 35% backhaul traffic [76, 89, 90]. In addition, edge caching provides a low-latency service since the content

is retrieved from the edge instead of remote servers. However, due to the limited cache capacity of an individual SBS, the performance of edge caching can be constrained. To enlarge cached contents, a straightforward method is to leverage caching resources in a cooperative manner, i.e., cooperative caching. Cooperative caching can be divided into two categories: a) *cooperative edge caching* where contents are cached in the SBS cluster which consists of multiple SBSs in proximity, and b) *device-to-device (D2D) caching* where contents are cached in nearby users. In the cooperative edge caching, each SBS in the SBS cluster caches diverse contents to increase caching diversity and serves users, while in the D2D caching, each user and its neighboring user cache diverse contents and exchange cached contents via high-rate D2D communications.

Incorporating cooperative caching in mmWave dense networks can significantly relieve the backhaul burden and reduce the content retrieval delay. Besides, it also introduces an extra advantage. In lower frequency band systems, the performance of cooperative caching is throttled by multiuser interference which is caused by omni-directional transmission patterns, while directional antennas in mmWave systems naturally tackle the interference issue. However, cooperative caching in mmWave networks poses new challenges. There is no tractable analytical model for mmWave networks which incorporates the impacts of directional antenna, network density and content caching. Moreover, this intractability makes it difficult to attain closed-form expressions, which is arduous to provide valuable insights for the system design.

In this chapter, we propose a novel cooperative caching policy in mmWave cellular networks, which cooperatively utilizes cache resources of the user, its D2D peer and neighboring SBSs. Specifically, the contents are cached according to the content retrieval delay. The most popular contents are cached in the user and its D2D peer due to the low content retrieval delay, while less popular contents are cached in the SBS cluster. With such designed caching policy, we derive the backhaul offloading gain. In addition, we consider a practical mmWave directional antenna model, where the main lobe antenna gain varies and the side lobe antenna gain is non-zero, which entangles the interference analysis. Exploiting the stochastic information of the network topology, we theoretically analyze the average content retrieval delay of the proposed policy in mmWave systems. Analytical results reveal the impacts of the network density and practical directional antennas on caching performance, which are not well considered in the literature. Main contributions are summarized as follows:

- A D2D-assisted cooperative edge caching (DCEC) policy which cooperatively exploits the cache resources of both users and SBSs, is proposed and analyzed in mmWave dense networks.

- We derive closed-form expressions of the backhaul offloading gain and the content retrieval delay in mmWave dense networks based on stochastic information of network topology.
- The impacts of the network density and practical directional antennas on caching performance are analyzed respectively. Analytical results show that content retrieval delay via D2D communications increases significantly with the network density, while that via cellular communications increases slightly. Besides, analytical results indicate the performance increases linearly with the directional antenna gain.
- Analytical results reveal the tradeoff relationship between transmission efficiency and caching diversity in mmWave dense networks, which investigates the optimal SBS cluster size.

The remainder of this chapter is organized as follows. Section 5.2 reviews related works. Then, the system model is presented in Section 5.3. Next, we propose the DCEC policy and analyze its backhaul offloading gain in Section 5.4. Section 5.5 analyzes the content retrieval delay performance of the proposed policy. Extensive simulations are presented in Section 5.6. Finally, concluding remarks are given in Section 5.7.

5.2 Literature Review

Endowed with the computing and storage functionalities, mobile edge computing (MEC) provides high quality of experience (QoE) for mobile users in proximity. A significant body of recent literature focuses on the computing functionality of MEC [91–93]. Rodrigues *et al.* proposed a hybrid method through virtual machine migration and transmission power control, aiming at minimizing the service latency [91]. An extended work focused on reconfiguring edge servers with an objective to improve the scalability [92]. Also, recently, the authors in [93] jointly optimized the computing and caching resources to achieve the maximum utility in mobile edge networks.

Cooperative caching, which cooperatively utilizes storage functionality of MEC, is another approach to enhance QoE. Two methods are distinguished in the literature: D2D caching and cooperative edge caching. In microwave bands, both these two caching policies have been studied in an extensive body of work. Firstly, by utilizing caching resources among users and high-rate D2D communications [94–96], D2D caching can offload cellular traffic, increase cellular transmission rate and reduce the power consumption of SBS.

A scaling law, where the throughput increases with the number of nodes in the network under an impractical condition that the D2D transmission range adjusts to the network density, is obtained in D2D caching networks [97]. Wang *et al.* investigated the performance of D2D caching in mobile scenarios where users frequently contact with neighboring users to exchange contents via D2D communications [98]. In [99], three scheduling schemes for edge caching with D2D connections are proposed which can maximize the throughput of D2D links with low complexity. Secondly, for the cooperative edge caching, caching resources in the SBS cluster are utilized to enlarge cached contents. Chen *et al.* firstly presented a cooperative caching policy which cooperatively cached different fractions of less popular contents in different SBSs to increase content diversity, and revealed the trade-off relationship between transmission diversity and content diversity [100]. To maximize the performance of the cooperative edge caching, content placement and cache size have been optimized. Zhang *et al.* studied the delay-optimal problem via optimizing content placement, where a greedy algorithm is proposed to optimize content placement in the cooperative edge caching policy [101]. Another work investigated the cache size optimization problem considering the budget of cache deployment in heterogeneous networks [102]. Recent research in [103] applied in-memory storage and processing to enhance the energy efficiency of edge caching. Also, recently, the authors in [104] developed a cooperative caching policy based on the content popularity distribution and user preference, which can improve the content hit ratio and reduce the transmission delay. Furthermore, observing the fact that popular contents are highly correlated to user locations, recent research [58] proposed a location-aware caching policy through an online learning approach.

Although interesting, these works solely focus on the cooperative caching policies operate in the microwave bands and do not consider the capability of mmWave communications. In addition, multiuser interference poses a challenge for cooperative caching at low frequency bands, especially in ultra-dense networks. Both D2D caching and cooperative edge caching require complex interference management technologies, such as power control and interference alignment, to reduce interference [101, 105]. However, this challenge can be easily addressed in mmWave systems as directional antennas significantly reduce multiuser interference. Studies on caching at mmWave frequency bands are quite limited. Semiari *et al.* proposed a proactive caching policy to reduce handover failures in mobile mmWave networks [106]. They focused on utilizing device caching and did not consider the cooperative edge caching. Ji *et al.* first employed D2D caching in mmWave networks to enhance network performance [107]. However, no analytical results in [107] is provided to characterize the D2D caching performance. Then, in the very recent work [108], Giatsoglou *et al.* proposed and analyzed the D2D caching policy based on a stochastic geometry framework. However, this caching policy does not exploit cache resource of SBSs

Table 5.1: Variables and notations in cooperative caching.

Notation	Description
$\mathcal{F}$	Requested file library
Φ_{BS}	PPP of SBS
λ_{BS}	Density of SBS
Φ_{UE}	PPP of users
λ_{UE}	Density of users
W	System bandwidth
ϕ	Fraction of bandwidth allocation
α	Path loss exponent
K	SBS cluster size
r	Physical distance
R	Transmission rate
σ^2	Background noise power
D	Average content retrieval delay
S	Signal power
I	Interference power
ξ	Content popularity skewness
G	Directional antenna gain
F	Backhaul offloading gain
h	Content hit ratio
$\mathcal{B}_o$	Associated SBS

in proximity. In addition, the analytical results cannot characterize the impact of directional antennas in mmWave communications. Both solutions from [107] and [108] solely applied D2D caching in mmWave networks to offload backhaul traffic while without taking the network density into consideration. Furthermore, cooperative edge caching policy and practical mmWave antenna features have not been investigated, which may greatly impact the network performance.

5.3 System Model

In this section, we present the network model, the content popularity model, the directional antenna model, the mmWave channel model and the transmission model, respectively. A summary of important notations is given in Table 5.1.

5.3.1 Network Model

As shown in Fig. 5.1, we consider a cache-enabled edge network where each entity can cache popular contents. SBSs and users follow homogeneous Poisson point processes (PPPs) Φ_{BS} and Φ_{UE} on the plane, whose densities are given by λ_{BS} and λ_{UE}, respectively [108, 109]. All the SBSs share the same spectrum and connect to remote servers with constrained backhaul links. Each SBS adopts a time division multiple access (TDMA) mode to serve associated users. Both SBSs and users are equipped with steerable directional antennas. Beamforming training is perfectly performed between users and associated SBSs before the data transmission.

Considering the user-centric architecture [101], each user is allowed to be served by K SBSs, which composes a SBS cluster, denoted by $\{\text{SBS}_1, \text{SBS}_2, ..., \text{SBS}_K\}$. For example, as shown in Fig. 5.1, User A is served by a SBS cluster with three SBSs, $\{\text{SBS}_1, \text{SBS}_2, \text{SBS}_3\}$. Users are divided into two categories: unpaired users and paired users. Unpaired users follow a homogeneous PPP Φ_u with a density of λ_u, which are only served by SBSs, such as User C shown in Fig. 5.1. A paired user is not only served by the SBS cluster but also its D2D peer. Paired users follow a homogeneous PPP Φ_p with a density of λ_p, and exchange cached contents via high-rate D2D communications. For example, User A and User B form a D2D pair and connect with each other via a D2D link. For a paired user, its D2D peer uniformly distributes within a disk of radius r_d^{max}. Thus, the distance r_d between the user and its D2D peer follows the following distribution [108]

$$f(r_d) = \frac{2r_d}{(r_d^{max})^2}, 0 < r_d < r_d^{max}. \tag{5.1}$$

As D2D communications and cellular communications coexist in the system, we adopt an overlay scheme, i.e., D2D communications and cellular communications use different frequency bands to avoid interference. Assume that W is the available bandwidth of the mmWave system, and ϕW bandwidth is allocated to D2D communications.

5.3.2 Content Popularity Model

Let $\mathcal{F} = \{f_1, f_2, ..., f_i, ...f_{|\mathcal{F}|}\}$ and $\mathcal{Q} = \{q_1, q_2, ..., q_i, ..., q_{|\mathcal{F}|}\}$ denote the sets of requested content and corresponding popularity distribution, respectively. $|\mathcal{F}|$ is the total number of contents. The Zipf distribution is used to characterize the popularity distribution [101],

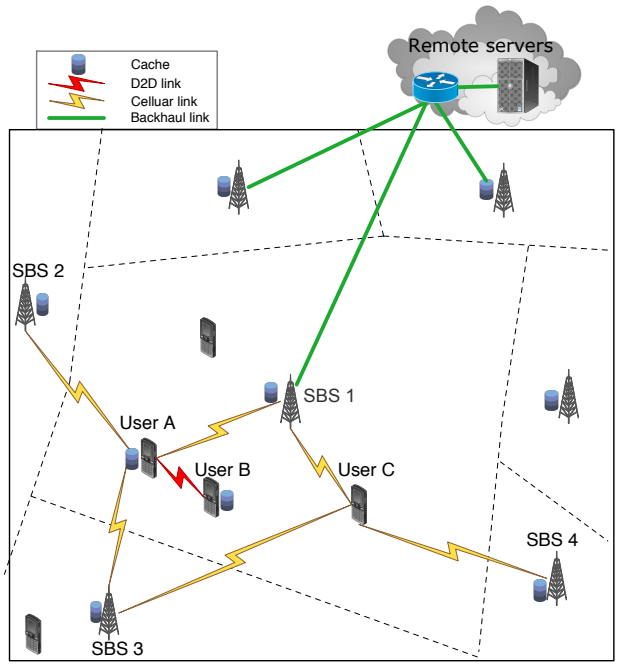

Fig. 5.1: Cache-enabled edge network topology.

and the popularity of the i-th content is given by

$$q_i = \frac{i^{-\xi}}{\sum_{j=1}^{|\mathcal{F}|} j^{-\xi}}, 1 \leq i \leq |\mathcal{F}| \tag{5.2}$$

where $\xi \geq 0$ denotes the content popularity skewness which varies based on content types. A larger popularity skewness value implies that the content requests are more concentrated.

5.3.3 Directional Antenna Model

Literature widely adopts the idealized "flat-top" model, which has a constant antenna gain in the main lobe and zero elsewhere, to simplify the interference analysis [110]. However, in the practical directional antenna, the main-lobe antenna gain varies and the side-lobe antenna gain is non-zero, which brings difficulty in interference analysis and management. In this chapter, we adopt a practical model with respect to a relative angle θ to its boresight

to characterize the directional antenna gain, which is given by

$$G(\theta) = \begin{cases} G_m 10^{-c\left(\frac{2\theta}{\omega_m}\right)^2} & |\theta| \leq \frac{\theta_m}{2} \\ G_s & \frac{\theta_m}{2} < |\theta| \leq \pi. \end{cases} \tag{5.3}$$

G_m and G_s denote the maximum antenna gain of the main lobe and the average antenna gain of the side lobe, respectively. ω_m and θ_m represent the beamwidth of the half-power and main lobe, respectively. c is an experienced constant, which takes the value of 0.3 [16].

5.3.4 mmWave Channel Model

Regarding the channel model, the large-scale channel fading of mmWave links, in dB, is modeled as

$$PL(dB) = 20\log_{10}\left(\frac{4\pi d_0}{\lambda}\right) + 10\alpha\log_{10}\left(\frac{r}{d_0}\right), r \geq d_0 \tag{5.4}$$

where r and α denote the propagation distance and the path loss exponent, respectively. λ is the wavelength and d_0 is the free space reference distance [10, 111]. This model works well when the propagation distance is larger than the reference distance. For the sake of presentation, the average path loss can be rewritten as

$$\beta = Cr^{-\alpha} \tag{5.5}$$

where $C = \frac{\lambda^2}{d_0^3(4\pi)^2}$ is a constant.

For the small scale fading, the fast Raleigh fading is considered in this chapter, i.e., $h \sim \exp(1)$ whose channel power gain is an exponential random variable with a unit mean.

5.3.5 Transmission Model

The transmission rate of a mmWave link is given by

$$R = \frac{W}{N_{cell}}\log_2\left(1 + \frac{S}{I + \sigma^2}\right) \tag{5.6}$$

where N_{cell} is the cell load. The power of background thermal noise can be modeled as $\sigma^2 = WN_o$ where N_o is the noise power spectral density. S and I represent the power of signal and interference, respectively.

In mmWave networks, each user is interfered by all the other SBSs excluding its associated SBS $\mathcal{B}_o$. Thus, considering the directional antenna model and the channel model, interference power is given by

$$\begin{aligned} I &= \sum_{i \in \Phi_{BS} \setminus \mathcal{B}_o} I_i \\ &= \sum_{i \in \Phi_{BS} \setminus \mathcal{B}_o} P_B G(\theta_{t,i}) G(\theta_{r,i}) h_i C r_i^{-\alpha} \end{aligned} \tag{5.7}$$

where $G(\theta_{t,i})$ and $G(\theta_{r,i})$ represent transmit and receive directional antenna gains, receptively. $\theta_{t,i}$ and $\theta_{r,i}$ are the angle of departure (AOD) and the angle of arrival (AOA) of the interference link between the user and the ith interfered SBS, respectively. r_i denotes the physical distance between the user and the ith interfered SBS. For tractability of the analysis, we assume that AOAs and AODs of interference links are uniformly distributed in $(0, 2\pi]$ [7], which provides an average directional antenna gain for the interference signal. The average directional antenna gain is given by

$$\begin{aligned} \bar{G} &= \int_0^{2\pi} G(\theta) f(\theta) d\theta \\ &= \int_0^{\frac{\theta_m}{2}} G_m 10^{-c\left(\frac{2\theta}{\omega_m}\right)^2} \frac{1}{\pi} d\theta + \int_{\frac{\theta}{2}}^{\pi} G_s \frac{1}{\pi} d\theta \\ &= \frac{\omega_m G_m}{\sqrt{2c\pi \ln 10}} \mathrm{erfc}\left(\frac{\theta_m \sqrt{c \ln 10}}{\omega_m} \right) - \frac{G_s \theta_m}{2\pi} + G_s \end{aligned} \tag{5.8}$$

where $\mathrm{erfc}(x) = \int_0^x e^{-t^2} dt$ represents the Gauss error function. Considering average directional antenna gains of interference links, the average interference power in (5.7) can be rewritten as

$$\mathbb{E}[I] = \sum_{i \in \Phi_{BS} \setminus \mathcal{B}_o} P_B \bar{G}^2 C \mathbb{E}[h_i] \mathbb{E}[r_i^{-\alpha}]. \tag{5.9}$$

This interference model is used in the following analysis in this chapter.

5.4 D2D-Assisted Cooperative Edge Caching (DCEC) Policy

In this section, we first propose the DCEC policy to exploit caching diversity, and then analyze its backhaul offloading performance.

5.4.1 Scheme Design

In the DCEC policy, cache resource of the user, its D2D peer and the SBS cluster are utilized in a cooperative manner to store diverse contents to offload backhaul traffic. Note that the user queries its D2D peer and the SBS cluster to identify where the requested content is cached. For a requested content, if the content is cached in the user on-board storage, the user retrieves the content locally with negligible latency. Next, if the content is cached in its D2D peer, the user retrieves the content via D2D communications. Then, if the content is cached in an arbitrary SBS in the SBS cluster, the user associates to the SBS and then retrieves the content via cellular communications. Retrieving contents via cellular communications incurs higher delays compared with that via D2D communications, as D2D communications provide higher transmission rates than cellular communications due to shorter distances. Otherwise, if the content is miss cached, the user associates with the nearest SBS B_o and retrieves the content from remote servers via the constraint backhaul link, which incurs a long delay. Thus, for a specific user, the content retrieval priority set which is sorted based on delay in an ascending order, is given by {user $\leq$ its D2D peer $\leq$ SBS cluster $\leq$ remoter servers}. This content retrieval priority set is applied in the content placement of our proposed caching policy to minimize content retrieval delay, which is described in the following two steps.

Firstly, the most popular contents are cached in both the user and its D2D peer due to the short content retrieval delay. Assume that each user has the same cache capacity, which is denoted by C_u. Note that users are divided into paired users and unpaired users. For paired users, the most popular $2C_u$ contents, i.e., $\{f_1, f_2, ..., f_{2C_u}\}$, are cached in the D2D pair which consists of the user and its D2D peer. For fairness, these $2C_u$ contents are equally distributed in the user and its D2D peer based on content popularity so that two users in the D2D pair have nearly the same content hit ratio. For example, User A and User B in the D2D pair have the same content hit ratio, i.e., $h_A = h_B$. Thus, the content

hit ratio of a paired user is given by

$$h_p = \frac{1}{2}\sum_{i=1}^{2C_u} q_i. \tag{5.10}$$

For unpaired users, without the assistance of D2D peers, unpaired users can only cache the most popular C_u contents, i.e., $\{f_1, f_2, ..., f_{C_u}\}$. Thus, the content hit ratio for an unpaired user is

$$h_u = \sum_{i=1}^{C_u} q_i. \tag{5.11}$$

Secondly, less popular contents are cached in the SBS cluster due to the long content retrieval delay via cellular communications. Note that users are served by a SBS cluster with a size of K. Assume that each SBS has the same cache capacity C_s. The SBS cluster caches the next KC_s popular contents, i.e., $\{f_{2C_u+1}, f_{2C_u+2}, ..., f_{2C_u+KC_s}\}$. Similarly, for the fairness and cell load balance, these KC_s contents are equally distributed in each SBS in the SBS cluster based on content popularity so that each SBS has the same content hit ratio, which is given by

$$h_s = \frac{1}{K}\sum_{i=2C_u+1}^{2C_u+KC_s} q_i. \tag{5.12}$$

Note that some fair popular contents are miss cached for the unpaired users. However, in the dense network scenario, the unpaired users only account for a small portion of all the users as users can associate with neighboring users with high probability. Specifically, in our simulations, we assume that 80% users are paired users while only 20% users are unpaired users. Hence, the impact of unpaired users on all the users is relatively small.

5.4.2 Backhaul Offloading Analysis

With the proposed caching policy, backhaul burden can be significantly relieved as users retrieve cached contents in edge networks instead of constrained backhaul links. In this chapter, we define the *backhaul offloading gain* as the ratio between data traffic that is not served by backhaul links and all the data traffic. In this subsection, the backhaul offloading gain of DCEC policy is analyzed.

For paired users, cache capacities of two users and the SBS cluster are cooperatively utilized to store the most popular $2C_u + KC_s$ contents, and hence the backhaul offloading

gain is $2h_p + Kh_s$. For unpaired users, the backhaul offloading gain is $h_u + Kh_s$ without the assistance of the D2D peer. Thus, the average backhaul offloading gain of the DCEC policy is given by

$$F = h_u(1-\delta) + 2h_p\delta + Kh_s \tag{5.13}$$

where $\delta = \frac{\lambda_p}{\lambda_p+\lambda_u}$ denotes the fraction of paired users among all the users. It is obvious that the backhaul offloading gain increases with the cluster size K due to the caching diversity gain.

The corresponding miss caching probability, i.e., the probability that the requested content is not cached in edge networks, is given by

$$P_m = 1 - F. \tag{5.14}$$

The miss cached contents can be retrieved from remote servers via the nearest cellular link and the constraint backhaul link.

5.5 Content Retrieval Delay Analysis

In this section, the average *content retrieval delay* of DCEC policy is analyzed. As users retrieve the requested content via different communication links, transmission performance of these communication links are analyzed respectively to obtain the average content retrieval delay. If the requested content is miss cached, users retrieve the content via two communication links. Firstly, the content is downloaded from remote servers to the nearest SBS with the average backhaul transmission rate $\mathbb{E}[R_B]$, and then transmitted to the user with the average nearest SBS transmission rate $\mathbb{E}[R_N]$. If the content is cached in the SBS cluster or its D2D peer, the user retrieves the content with the average SBS cluster transmission rate $\mathbb{E}[R_C]$ or the average D2D transmission rate $\mathbb{E}[R_D]$. Assume that the average content size is represented by ν, the average content retrieval delay of the DCEC policy is given by

$$D = \frac{P_m\nu}{\mathbb{E}[R_B]} + \frac{P_m\nu}{\mathbb{E}[R_N]} + \frac{P_s\nu}{\mathbb{E}[R_C]} + \frac{P_d\nu}{\mathbb{E}[R_D]} \tag{5.15}$$

where $P_s = Kh_s$ and $P_d = \delta h_p$ denote the probabilities that the requested content is cached in the SBS cluster and the D2D peer, respectively. In the following, lower bounds of these transmission rates are derived analytically respectively, and hence the upper bound of the average content retrieval delay is provided.

5.5.1 Backhaul Transmission Rate Analysis

In this subsection, the average backhaul transmission rate is analyzed. According to the property of PPP, the traffic of each part in the network also follows PPP. Users served by constraint backhaul links are considered as a homogeneous PPP Φ_B in the plane with a density of $P_m\lambda_{UE}$. Assume each SBS has the same backhaul capacity B and is served by its associated users with a TDMA mode.

Lemma 2 *The average backhaul transmission rate of each user is given by*

$$\mathbb{E}[R_B] = \frac{B\lambda_{BS}}{P_m\lambda_{UE}} \frac{\left(1+\frac{P_m\lambda_{UE}}{\kappa\lambda_{BS}}\right)^{\kappa+1}}{\left(1+\frac{P_m\lambda_{UE}}{\kappa\lambda_{BS}}\right)^{\kappa+1}-1} \tag{5.16}$$

where $\kappa = 3.5$ is a constant.

Proof. As the backhaul resource is equally allocated to each user, the average backhaul rate of each user is $B/\mathbb{E}[N_B]$. N_B is the backhaul load which is a random variable depending on the SBS cell area. The SBS cell area follows a Gamma distribution with a parameter κ. The probability distribution function (PDF) of the cell area a is given by [112]

$$f(a) = a^{\kappa-1}e^{-\kappa\lambda_{BS}a}\frac{(\kappa\lambda_{BS})^{\kappa}}{\Gamma(\kappa)}. \tag{5.17}$$

Hence, the average backhaul load is

$$\begin{aligned}
\mathbb{E}[N_B] &= \int_a^{\infty} \sum_{n=1}^{\infty} n \Pr\{N_B = n|a\} f(a) da \\
&\overset{(a)}{=} \int_a^{\infty} \sum_{n=1}^{\infty} n \frac{(P_m \lambda_{UE} a)^n}{n!} e^{-P_m \lambda_{UE} a} f(a) da \\
&= \int_a^{\infty} P_m \lambda_{UE} a \left(1 - e^{-P_m \lambda_{UE} a}\right) a^{\kappa-1} e^{-\kappa \lambda_{BS} a} \frac{(\kappa \lambda_{BS})^{\kappa}}{\Gamma(\kappa)} da \\
&\overset{(b)}{=} \frac{P_m \lambda_{UE}}{\kappa \lambda_{BS}} \frac{\Gamma(\kappa+1)}{\Gamma(\kappa)} \left(1 - \left(\frac{\kappa \lambda_{BS}}{\kappa \lambda_{BS} + P_m \lambda_{UE}}\right)^{\kappa+1}\right) \\
&= \frac{P_m \lambda_{UE}}{\lambda_{BS}} \left(1 - \frac{1}{\left(1 + \frac{P_m \lambda_{UE}}{\kappa \lambda_{BS}}\right)^{\kappa+1}}\right).
\end{aligned} \tag{5.18}$$

(a) follows from the fact that N_B is a Poisson distribution random variable with a mean of $P_m \lambda_{UE} a$ [113]. (b) is obtained via the definition of the gamma function $\Gamma(z) = \int_0^{\infty} x^{z-1} e^{-x} dx$. Thus, Lemma 2 is proved. □

5.5.2 Nearest SBS Transmission Rate Analysis

When the requested content is downloaded from remote servers via backhaul links, the user retrieves the content by associating to the nearest SBS, which provides the maximum cellular transmission rate. In this subsection, we aim to analyze the transmission rate of the nearest SBS.

Since the overlay scheme is adopted in the system, $(1-\phi)W$ bandwidth is allocated to cellular communications and each SBS serves associated users with a TDMA mode. The associated users of each SBS consist of two categories: miss cached users whose requested content is miss cached and SBS cluster cached user whose requested content is cached in the SBS cluster. Thus, the associated users of each SBS are modeled as a PPP Φ_C with a density of $\lambda_C = (P_m + P_s)\lambda_{UE}$. The total number of SBS is given by N_{BS}. Similar to the

result in (5.18), the average cell load is given by

$$\mathbb{E}[N_C] = \frac{(P_m + P_s)\lambda_{UE}}{\lambda_{BS}} \left(1 - \frac{1}{\left(1 + \frac{(P_m+P_s)\lambda_{UE}}{\kappa\lambda_{BS}}\right)^{\kappa+1}} \right). \tag{5.19}$$

Lemma 3 *When the user is associated to the nearest SBS $\mathcal{B}_o$, the average transmission rate is lower bounded by*

$$\mathbb{E}[R_N] \geq \frac{(1-\phi)W}{\mathbb{E}[N_C]\ln 2} \left(2\ln\frac{G_m}{\bar{G}} + \frac{(\alpha-2)\gamma}{2} - \ln J_1(\alpha) \right) \tag{5.20}$$

where

$$J_1(\alpha) = \begin{cases} \dfrac{\Gamma(N_{BS}+1-\frac{\alpha}{2})}{(1-\frac{\alpha}{2})\Gamma(N_{BS})} - \Gamma\left(1-\dfrac{\alpha}{2}\right), \ \alpha \neq 2 \\ \ln(N_{BS}-1) + \gamma, \ \alpha = 2 \end{cases} \tag{5.21}$$

and γ is the Euler-Mascheroni constant whose value approximates to 0.577.

Proof. Assume directional antennas between the user and its associated nearest SBS are well-aligned, the received signal power is given by

$$S = P_B G_m^2 h_1 C r_1^{-\alpha} \tag{5.22}$$

where r_1 is the distance between the user and the nearest SBS. The interference signal power includes the interference signal from all the other SBSs, and the interference signals are independent random variables [114].

Using the transmission model in (5.6), the average transmission rate is given by

$$\begin{aligned}
\mathbb{E}[R_N] &= \mathbb{E}\left[\frac{(1-\phi)W}{N_C}\log_2\left(1+\frac{S}{I+\sigma^2}\right)\right] \\
&= \frac{(1-\phi)W}{\mathbb{E}[N_C]\ln 2}\mathbb{E}\left[\ln\left(1+\frac{S}{\sum_{i\in\Phi_{BS}\setminus\mathcal{B}_o} I_i+\sigma^2}\right)\right] \\
&\geq \frac{(1-\phi)W}{\mathbb{E}[N_C]\ln 2}\mathbb{E}\left[\ln\frac{S}{\sum_{i\in\Phi_{BS}\setminus\mathcal{B}_o} I_i}\right] \\
&\geq \frac{(1-\phi)W}{\mathbb{E}[N_C]\ln 2}\left(\mathbb{E}[\ln S]-\ln\sum_{i\in\Phi_{BS}\setminus\mathcal{B}_o}\mathbb{E}\left[I_i\right]\right).
\end{aligned} \tag{5.23}$$

The second step is because the received signal-to-interference-plus-noise-ratio (SINR) and the cellular load are independent random variables. The first inequality holds as the thermal noise can be ignored in high SNR scenarios. Practical applications are guaranteed with high SNR due to the reliable communication requirement. The last inequality holds from the Jensen inequality. In the following, $\mathbb{E}[\ln S]$ and $\sum_{i\in\Phi_{BS}\setminus\mathcal{B}_o}\mathbb{E}[I_i]$ are analyzed, respectively.

Firstly, substituting the definition of desired signal in (5.22), $\mathbb{E}[\ln S]$ can be rewritten as

$$\begin{aligned}
\mathbb{E}[\ln S] &= \mathbb{E}\left[\ln\left(P_B G_m^2 h_1 C r_1^{-\alpha}\right)\right] \\
&= \ln\left(P_B G_m^2 C\right)+\mathbb{E}\left[\ln h_1\right]-\alpha\mathbb{E}\left[\ln r_1\right] \\
&= \ln\left(P_B G_m^2 C\right)-\gamma+\frac{\alpha}{2}\left(\gamma+\ln\pi\lambda_{BS}\right).
\end{aligned} \tag{5.24}$$

The equality holds because of the following two facts:

$$\mathbb{E}[\ln h_1]=\int_0^\infty \ln x e^{-x}dx=-\gamma$$

and

$$\begin{aligned}\mathbb{E}[\ln r_1] &= \int_0^\infty \ln r_1 f(r_1) dr_1 \\ &\overset{(a)}{=} \int_0^\infty \ln(r_1) 2\pi\lambda_{BS} r_1 e^{-\pi\lambda_{BS} r_1^2} dr_1 \\ &\overset{(b)}{=} \frac{1}{2}\left(\int_0^\infty e^{-y}\ln y dy - \int_0^\infty e^{-y}\ln(\pi\lambda_{BS}) dy\right) \\ &= -\frac{\gamma + \ln \pi\lambda_{BS}}{2}\end{aligned} \tag{5.25}$$

where (a) is due to the fact that r_1 obeys the following distribution $f(r_1) = 2\pi\lambda_{BS} r_1 e^{-\pi\lambda_{BS} r_1^2}$ [114]. (b) follows by changing variable $y = \pi\lambda_{BS} r_1^2$.

Secondly, using the average interference model in (5.9), $\sum_{i\in\Phi_{BS}\setminus\mathcal{B}_o} \mathbb{E}[I_i]$ is given as

$$\begin{aligned}\ln \sum_{i\in\Phi_{BS}\setminus\mathcal{B}_o} \mathbb{E}[I_i] &= \ln \sum_{i\in\Phi_{BS}\setminus\mathcal{B}_o} P_B \bar{G}^2 C \mathbb{E}[h_i]\mathbb{E}[r_i^{-\alpha}] \\ &= \ln\left(P_B \bar{G}^2 C\right) + \ln \sum_{i\in\Phi_{BS}\setminus\mathcal{B}_o} \mathbb{E}[r_i^{-\alpha}].\end{aligned} \tag{5.26}$$

The last equality is due to the fact that $\mathbb{E}[h_i] = 1$.

As the PDF of the distance between the user and i-th nearest SBS r_i is given by [113]

$$f(r,i) = \frac{2(\pi\lambda_{BS})^i}{(i-1)!} r^{2i-1} e^{-\pi\lambda_{BS} r^2}, i = 2, 3...$$

the $-\alpha$th moments of r_i can be calculated as follows:

$$\begin{aligned}\mathbb{E}[r_i^{-\alpha}] &= \int_0^\infty r^{-\alpha} f(r,i) dr \\ &= \int_0^\infty \frac{2(\pi\lambda_{BS})^i}{(i-1)!} r^{2i-1-\alpha} e^{-\pi\lambda_{BS} r^2} dr \\ &= \frac{(\pi\lambda_{BS})^{\frac{\alpha}{2}}}{(i-1)!} \int_0^\infty y^{\frac{2i-\alpha}{2}-1} e^{-y} dy \\ &= (\pi\lambda_{BS})^{\frac{\alpha}{2}} \frac{\Gamma(i-\frac{\alpha}{2})}{\Gamma(i)}, i > \frac{\alpha}{2}.\end{aligned} \tag{5.27}$$

Next, we aim to obtain the summation of the $-\alpha$th moments of r_i. When α attains different values, the summation of the $-\alpha$th moments of r_i varies.

- When $\alpha \neq 2$, with results in (5.27), the summation of the $-\alpha$th moments of r_i is

$$\begin{aligned}\sum_{i\in\Phi_{BS}\setminus\mathcal{B}_o}\mathbb{E}[r_i^{-\alpha}] &= (\pi\lambda_{BS})^{\frac{\alpha}{2}}\sum_{i=2}^{N_{BS}}\frac{\Gamma(i-\frac{\alpha}{2})}{\Gamma(i)}\\ &= (\pi\lambda_{BS})^{\frac{\alpha}{2}}\left(\frac{\Gamma(N_{BS}+1-\frac{\alpha}{2})}{(1-\frac{\alpha}{2})\Gamma(N_{BS})}-\Gamma\left(1-\frac{\alpha}{2}\right)\right).\end{aligned} \tag{5.28}$$

  The last equality follows from the following equality [114]

$$\sum_{j=1}^{n}\frac{\Gamma(j-\beta)}{\Gamma(j)} = \frac{\Gamma(n+1-\beta)}{(1-\beta)\Gamma(n)}, \beta\neq 2. \tag{5.29}$$

- When $\alpha = 2$, the summation is given by

$$\begin{aligned}\sum_{i\in\Phi_{BS}\setminus\mathcal{B}_o}\mathbb{E}[r_i^{-\alpha}] &= (\pi\lambda_{BS})^{\frac{\alpha}{2}}\sum_{i=2}^{N_{BS}}\frac{\Gamma(i-1)}{\Gamma(i)}\\ &= (\pi\lambda_{BS})^{\frac{\alpha}{2}}\sum_{i=1}^{N_{BS}-1}\frac{1}{i}\\ &\approx (\pi\lambda_{BS})^{\frac{\alpha}{2}}\left(\ln(N_{BS}-1)+\gamma\right)\end{aligned} \tag{5.30}$$

where the equality holds when N_{BS} is large enough. Thus, this approximation is reasonable in dense networks.

Substituting (5.28) and (5.30) into (5.26), the logarithmic form of the summation of average interference power can be rewritten as

$$\ln\sum_{i\in\Phi_{BS}\setminus\mathcal{B}_o}\mathbb{E}[I_i] = \ln P_B\bar{G}^2C + \frac{\alpha}{2}\ln\pi\lambda_{BS} + \ln J_1(\alpha) \tag{5.31}$$

where the definition of $J_1(\alpha)$ is given in (5.21). Substituting (5.24) and (5.31) into (5.23), Lemma 3 is proved. □

Remark 5 *Lemma 3 characterizes the nearest SBS transmission performance in terms*

of system parameters, such as the network density, the directional antenna gain and the path loss exponent. Firstly, the average transmission rate increases linearly with the directional antennas gain, i.e., $G_m/\bar{G}$, which indicates that directional antennas enhance the throughput of mmWave systems. Secondly, the average transmission rate grows linearly with the path loss exponent α because hostile path loss at mmWave frequency bands severely mitigates interference and offers a spatial reuse gain. Thirdly, transmission performance slightly decreases with the network density as $\ln J_1(\alpha)$ slightly increases with the number of SBSs N_{BS}. The reason is that both communication distance and interference distance adjust to the network density.

5.5.3 SBS Cluster Transmission Rate Analysis

Since each SBS in the SBS cluster has the same content hit ratio, the user has the same probability to associate to an arbitrary SBS in the SBS cluster. Thus, the average SBS cluster transmission rate should be averaged by transmission rates of all the candidate SBSs.

Lemma 4 *The average SBS cluster transmission rate is given by*

$$\mathbb{E}[R_C] \geq \frac{(1-\phi)W}{\mathbb{E}[N_C]\ln 2}\left(2\ln\frac{G_m}{\bar{G}} + \frac{(\alpha-2)\gamma}{2} - \frac{\alpha}{2K}\sum_{k=1}^{K}\sum_{i=1}^{k-1}\frac{1}{i} - \frac{1}{K}\sum_{k=1}^{K}\ln J_2(\alpha,k)\right) \tag{5.32}$$

where

$$J_2(\alpha,k) = \begin{cases} \dfrac{\Gamma(N_{BS}+1-\frac{\alpha}{2})}{(1-\frac{\alpha}{2})\Gamma(N_{BS})} - \dfrac{\Gamma(k-\frac{\alpha}{2})}{\Gamma(k)}, \ \alpha < 2 \\ E_1(r_0) + \ln(N_{BS}-1) + \gamma - J_4(k), \ \alpha = 2 \\ \Gamma\left(1-\dfrac{\alpha}{2}, r_0\right) + \dfrac{\Gamma(N_{BS}+1-\frac{\alpha}{2})}{(1-\frac{\alpha}{2})\Gamma(N_{BS})} - \Gamma\left(1-\dfrac{\alpha}{2}\right) - J_3(k) \end{cases} \tag{5.33}$$

$$J_3(k) = \begin{cases} \Gamma(1-\dfrac{\alpha}{2}, r_0), \ k = 1 \\ \dfrac{\Gamma(k-\frac{\alpha}{2})}{\Gamma(k)}, \ k \geq 2, \end{cases} \tag{5.34}$$

$$J_4(k) = \begin{cases} E_1(r_0), \ k = 1 \\ \dfrac{1}{k-1}, \ k \geq 2. \end{cases} \tag{5.35}$$

Note that $r_0 = \pi\lambda_{BS} d_0^2$. $\Gamma(z,a) = \int_a^\infty x^{z-1}e^{-x}dx$ *and* $E_1(x) = \int_x^\infty \frac{1}{t}e^{-t}dt$ *denote the incomplete gamma function and the exponential integral function, respectively.*

Proof. Let $\mathcal{B}_o = \{\mathcal{B}_o^1, \mathcal{B}_o^2, ..., \mathcal{B}_o^k, ..., \mathcal{B}_o^K\}$ denote the set of candidate SBSs among the SBS cluster, which is sorted based on physical distances in an ascending order. The corresponding set of physical distances is $\{r_1, r_2, ..., r_k, ..., r_K\}$.

If the user is associated to the kth nearest SBS $\mathcal{B}_o^k$, the received desired signal power is given by

$$S_C^k = P_B G_m^2 h_1 C r_k^{-\alpha}, 1 \leq k \leq K. \tag{5.36}$$

The corresponding interference power consists of received signal power from all the SBSs excluding the kth nearest SBS, which is given by

$$I_C^k = \sum_{i \in \Phi_{BS} \setminus \mathcal{B}_o^k} P_B G(\theta_{t,i}) G(\theta_{r,i}) h_i C r_i^{-\alpha}, 1 \leq k \leq K. \tag{5.37}$$

R_C^k denotes the average transmission rate between the user and the kth nearest SBS. Hence, the average transmission rate among the SBS cluster can be represented by

$$\begin{aligned} \mathbb{E}[R_C] &= \mathbb{E}\left[\frac{1}{K}\sum_{k=1}^{K} R_C^k\right] \\ &= \frac{(1-\phi)W}{K\mathbb{E}[N_C]\ln 2}\sum_{k=1}^{K}\ln\left(1+\frac{S_C^k}{I_C^k+\sigma^2}\right) \\ &\geq \frac{(1-\phi)W}{K\mathbb{E}[N_C]\ln 2}\sum_{k=1}^{K}\left(\mathbb{E}[\ln S_C^k] - \ln\sum_{i\in\Phi_{BS}\setminus\mathcal{B}_o^k} I_i^k\right) \\ &= \frac{(1-\phi)W}{\mathbb{E}[N_C]\ln 2}\left(2\ln\left(\frac{G_m}{\bar{G}}\right) - \gamma - \frac{\alpha}{K}\sum_{k=1}^{K}\mathbb{E}[\ln r_k] - \frac{1}{K}\sum_{k=1}^{K}\ln\sum_{i\in\Phi_{BS}\setminus\mathcal{B}_o^k}\mathbb{E}[r_i^{-\alpha}]\right). \end{aligned} \tag{5.38}$$

The inequality follows from the lower bound obtained in (5.23). The last step follows from

substitutions of (5.24) and (5.26). Then, according to [101], $\mathbb{E}[\ln r_k]$ is given by

$$\mathbb{E}[\ln r_k] = -\frac{1}{2}\left(\gamma + \ln(\pi\lambda_{BS}) - \sum_{i=1}^{k-1}\frac{1}{i}\right). \tag{5.39}$$

$\sum_{i\in\Phi_{BS}\setminus\mathcal{B}_o^k}\mathbb{E}[r_i^{-\alpha}]$ is derived in the following. When α attains different values, it can be represented in different forms.

- When $\alpha < 2$, with results in (5.27), we have

$$\begin{aligned}\sum_{i\in\Phi_{BS}\setminus\mathcal{B}_o^k}\mathbb{E}[r_i^{-\alpha}] &= \sum_{i=1}^{N_{BS}}\mathbb{E}[r_i^{-\alpha}] - \mathbb{E}[r_k^{-\alpha}] \\ &= (\pi\lambda_{BS})^{\frac{\alpha}{2}}\left(\frac{\Gamma(N_{BS}+1-\frac{\alpha}{2})}{(1-\frac{\alpha}{2})\Gamma(N_{BS})} - \frac{\Gamma(k-\frac{\alpha}{2})}{\Gamma(k)}\right).\end{aligned} \tag{5.40}$$

- When $\alpha = 2$, $\mathbb{E}[r_1^{-\alpha}] = \int_{r_0}^{\infty}\frac{1}{y}e^{-y}dy = E_1(r_0)$ according to the definition of the exponential integral function $E_1(x)$. While for $k \geq 2$, $\mathbb{E}[r_k^{-\alpha}] = \frac{1}{k-1}$ based on (5.30). Hence, $\mathbb{E}[r_k^{-\alpha}]$ can be described with a piecewise function $J_4(k)$ in (5.35). With the same method in (5.43), we have

$$\sum_{i\in\Phi_{BS}\setminus\mathcal{B}_o^k}\mathbb{E}[r_i^{-\alpha}] = (\pi\lambda_{BS})\left(E_1(r_0) + \ln(N_{BS}-1) + \gamma - J_4(k)\right). \tag{5.41}$$

- When $\alpha > 2$, $\mathbb{E}[r_1^{-\alpha}]$ becomes unbounded because the condition $i > \frac{\alpha}{2}$ in (5.27) is not satisfied. The reason is that the path loss model in (5.4) breaks down when the distance is smaller than d_0. As a solution, we apply a guard radius d_0 among receivers to exclude interferers in the short distance. Hence, $-\alpha$th moments of r_1 becomes

$$\begin{aligned}\mathbb{E}[r_1^{-\alpha}] &= \int_{d_0}^{\infty} r_1^{-\alpha} f(r_1) dr_1 \\ &= (\pi\lambda_{BS})^{\frac{\alpha}{2}}\int_{\pi\lambda_{BS}d_0^2}^{\infty} y^{\frac{2-\alpha}{2}-1}e^{-y}dy \\ &= (\pi\lambda_{BS})^{\frac{\alpha}{2}}\Gamma(1-\frac{\alpha}{2}, r_0).\end{aligned} \tag{5.42}$$

Thus, $\sum_{i\in\Phi_{BS}\setminus\mathcal{B}_o^k}\mathbb{E}[r_i^{-\alpha}]$ is given by

$$\sum_{i\in\Phi_{BS}\setminus\mathcal{B}_o^k}\mathbb{E}[r_i^{-\alpha}] = \mathbb{E}[r_1^{-\alpha}] + \sum_{i=2}^{N_{BS}}\mathbb{E}[r_i^{-\alpha}] - \mathbb{E}[r_k^{-\alpha}]$$
$$= (\pi\lambda_{BS})^{\frac{\alpha}{2}}\left(\Gamma(1-\frac{\alpha}{2}, r_0) - \Gamma(1-\frac{\alpha}{2}) + \frac{\Gamma(N_{BS}+1-\frac{\alpha}{2})}{(1-\frac{\alpha}{2})\Gamma(N_{BS})} - J_3(k)\right). \tag{5.43}$$

Substituting (5.39), (5.40), (5.43) and (5.41) into (5.38), Lemma 4 is proved. □

Remark 6 *Lemma 4 gives the transmission performance of the SBS cluster with respect to mmWave system parameters and provides the following important observations. Similar to that in Lemma 3 , the average SBS cluster transmission rate slightly decreases with network density because $J_2(\alpha, k)$ slightly increases with respect to the network density. Lemma 4 indicates that the transmission rate decreases with the cluster size, which illuminates the tradeoff relationship between caching diversity and transmission efficiency. Enlarging cluster size increases cache capacity to cache more contents, while transmission performance degrades as users retrieve cached contents with a large distance.*

5.5.4 D2D Transmission Rate Analysis

The D2D caching performance is analyzed in this subsection. D2D users follow a homogeneous PPP Φ_D and the corresponding density is $\lambda_D = P_d\lambda_{UE}$. Since mobile users provide a smaller directional antenna gain compared with SBSs due to limited space, G_u^m and $\bar{G}_u$ represent the maximal main lobe and the average antenna gains of users, respectively. Considering the overlay scheme, ϕW system bandwidth is allocated to D2D communications.

Lemma 5 *The average D2D transmission rate is lower bounded by*

$$\mathbb{E}[R_D] \geq \frac{\phi W}{\ln 2}\left(2\ln\frac{G_u^m}{\bar{G}_u} - \gamma - \alpha\left(\ln r_d^{max} - \frac{1}{2}\right) - \ln(\pi\lambda_D) - \ln J_5(\alpha)\right) \tag{5.44}$$

where

$$J_5(\alpha) = \begin{cases} \dfrac{R^{2-\alpha}}{1-\frac{\alpha}{2}}, \ \alpha < 2 \\ 2\ln\left(\dfrac{R}{d_0}\right), \ \alpha = 2 \\ \dfrac{R^{2-\alpha} - d_0^{2-\alpha}}{1-\frac{\alpha}{2}}, \ \alpha > 2 \end{cases} \tag{5.45}$$

where $R = \sqrt{\frac{N_D}{\pi\lambda_D}}$ *and* N_D *is the number of D2D transmitters.*

Proof. The detailed proof is given in Appendix 5.8.1. □

Remark 7 *Lemma 5 gives the transmission performance of D2D communication in terms of varying physical layer parameters. Most importantly, analytical results show that transmission performance decreases with the D2D user density* λ_D *which depends on the network density. This is because that distance of interference links scales with the network density, while the D2D communication distance keeps unchanged. In addition, comparing Lemma 3 and Lemma 4 with Lemma 5, the average D2D transmission rate decreases significantly with the increase of the network density, while cellular transmission performance decreases slightly with the network density. Hence, the content retrieval delay via D2D communications increases significantly with the network density, which requires a coordinated scheduling scheme for D2D communications in dense networks.*

5.6 Simulation Results

In this section, we compare the proposed DCEC policy with the state-of-the-art caching policy, and validate analytical results via extensive Monte-Carlo simulations. The simulation setup is given in Section 5.6.1. We evaluate the backhaul offloading performance in Section 5.6.2, analytical results of transmission performance in Section 5.6.3 and content retrieval delay performance in Section 5.6.4, respectively.

5.6.1 Simulation Setup

Important simulation parameters are listed in Table 5.2. We consider a simulation area of dimensions 1 km^2 (1000 m $\times$ 1000 m). Regarding the mmWave system, we consider the

Table 5.2: Simulation parameters in cooperative caching.

Notation	Parameter	Value
A	Simulation area	1 km^2
N_o	Background noise density	-174 dBm/Hz
W	Bandwidth	2.16 GHz
ϕ	Fraction of D2D spectrum	20%
f	Carrier frequency	60 GHz
α	Path loss exponent	$\{1.4, 1.6, 2\}$
P_B	SBS transmit power	30 dBm
P_U	User transmit power	20 dBm
G_s^m	SBS main lobe gain	18 dB
G_s^s	SBS side lobe gain	-2 dB
G_u^m	User main lobe gain	9 dB
G_u^m	User side lobe gain	-2 dB
ω_m	Half-power beamwidth	10^o
d_0	Reference distance	1 m
r_d^{max}	Maximum D2D distance	10 m
λ_{BS}	Network density	{80-400} per km^2
λ_{UE}	User density	{800-4000} per km^2
δ	Fraction of paired users	80%
F	Content library size	2000
ν	Average content size	100 Mbit
C_u	User cache capacity	150
C_s	SBS cache capacity	200

ratified IEEE 802.11ad system which operates at the 60 GHz unlicensed band with a channel bandwidth of 2.16 GHz [32]. 80% bandwidth is allocated to cellular communications, while 20% bandwidth to D2D communications. The parameters of directional antenna model are chosen based on typical values [108]. Here, we consider three different scenarios: the indoor conference room with LOS links, the living room with LOS links and NLOS links, and corresponding path loss exponents are set to 1.4, 1.6 and 2, respectively. Due to constraint on-board battery capacity and space in mobile devices, users adopt a lower transmit power and directional antenna gain compared to SBS. The constraint backhaul capacity is set to 3 Gbit/s unless otherwise specified. SBS density is chosen from 80 to 400 per km^2, with the average cell radius from 65 to 30 meters, corresponding to sparse rural and dense urban mmWave networks. The user density is set from 800 to 4000 per km^2, where 80% users are paired users. We consider a requested content library with a total

number of 2000 contents. The cache capacities of users and SBSs are set to 150 and 200 contents, respectively. To characterize video streaming applications, content popularity skewness is set to 0.56 unless otherwise specified [102].

In this section, we adopt the state-of-the-art most popular caching (MPC) policy as the benchmark. In the MPC policy, only the user and its associated SBS cache the most popular contents, i.e., the user and its associated SBS cache $\{f_1, f_2, ..., f_{C_u}\}$ and $\{f_{C_u+1}, f_{C_u+2}, ..., f_{C_u+C_s}\}$, respectively.

5.6.2 Backhaul Offloading Performance

As shown in Fig. 5.2(a), we compare the backhaul offloading performance of the DCEC policy with the MPC policy in terms of popularity skewness. It is obvious that the proposed policy significantly outperforms the MPC policy due to exploiting cache resource efficiently. More specifically, the proposed policy offloads about 50% backhaul traffic than MPC policy for $\xi = 0.6$. Besides, the performance gap between these two policies narrows with the growth of the content popularity skewness. The reason is that the cache capacities of individual user and its associated SBS are enough to store highly concentrated contents.

Figure 5.2 shows the backhaul offloading performance in terms of different system parameters. Fig. 5.2(b) shows the impact of SBS cache capacity on the backhaul offloading performance for $K = 3$. We observe that more backhaul traffic is offloaded by local edge networks with the increase of the SBS cache capacity because more contents are cached. Specifically, caching resource growth provides more performance gain in the small popularity skewness region than that in large popularity skewness region. This is because that large cache capacity is favored for less concentrated content request applications. In addition, the performance gap between the DCEC policy and the MPC policy broadens with the increase of SBS cache capacity. We further demonstrate the backhaul offloading performance in terms of the SBS cluster size in Fig. 5.2(c), where a significant backhaul offloading gain is achieved with the increase of SBS cluster size for low popularity skewness values. Particularly, the DCEC policy with eight SBSs offloads 70% backhaul traffic more than that with two SBSs for $\xi = 0.56$. But for large values of ξ, the performance enhancement becomes limited. Therefore, the DCEC policy favors less concentrated content request applications.

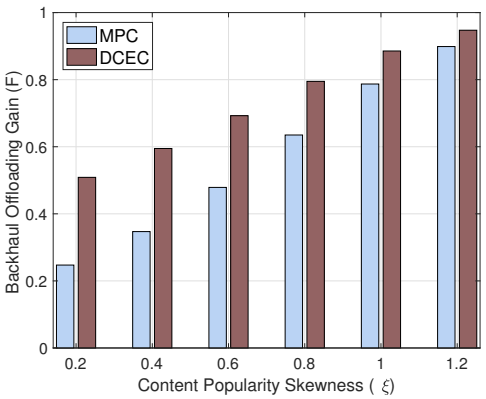

(a) Content popularity skewness.

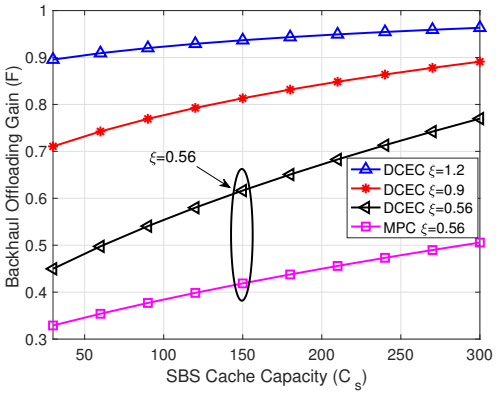

(b) SBS cache capacity

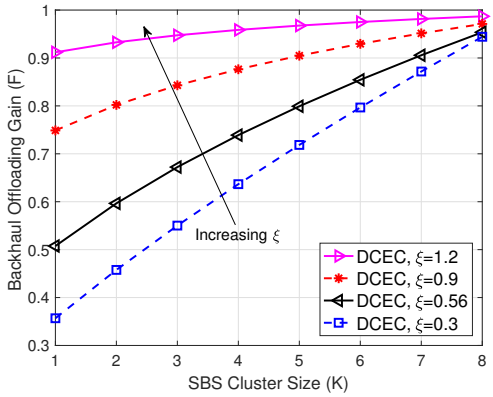

(c) SBS cluster size

Fig. 5.2: Backhaul offloading performance with respect to different system parameters.

5.6.3 Transmission Performance

In this subsection, analytical results of transmission performance are validated via extensive simulations. The simulation results are averaged over 10000 samples with different network topologies and channel fading.

Figure 5.3(a) shows the nearest SBS transmission rate in terms of the network density for $\alpha = 1.4, 1.6, 2$. The analytical lower bounds in Lemma 2 are quite close to simulation results under different channel conditions, which validates our analytical results. More importantly, the average rate slightly decreases with the network density. For $\alpha = 2$, the

transmission rate only decreases by 8% as the network density increases from 80 to 400 per km^2. Even for $\alpha = 1.4$, the transmission rate only degrades by 15%. In addition, we observe that the average transmission rate increases with respect to α due to the fact that interference is alleviated by severe propagation loss in mmWave channels.

As shown in Fig. 5.3(b), we investigate the average SBS cluster transmission rate for $K = 2$ and $\alpha = 1.4$, 1.6, 2. Narrow gaps are observed between simulation results and analytical bounds with respect to the network density, which indicates that our analytical results in Lemma 3 are quite accurate. Additionally, we observe that the transmission performance slightly decreases with the network density, which is similar as that of the nearest SBS. Particularly, for $\alpha = 2$, the average transmission rate decreases by only 10% from the sparse network for $\lambda_{BS} = 80$ to the dense network for $\lambda_{BS} = 400$.

Figure 5.3(c) shows the average transmission rates in terms of the network density with different cluster sizes for $\alpha = 1.6$. Analytical results are highly consistent with simulation results, which further corroborates the accuracy of Lemma 4. More importantly, we observe that the average SBS cluster transmission rate decreases with the increase of the cluster size. Specifically, the SBS cluster with two SBSs provides a data rate is around 1.08 Gbit/s for $\lambda_{BS} = 80$, while the SBS cluster with four SBSs only provides a data rate of 0.83 Gbit/s for the same network density, which decreases by nearly 23%. This is because users retrieve cached contents from remote SBSs with long distances. A large SBS cluster caches more contents while reduces the average transmission rate, which reveals the tradeoff relationship between caching diversity and transmission efficiency.

In Fig. 5.3(d), we investigate the average D2D transmission rate with respect to the D2D user density for $\alpha = 1.4$, 1.6, 2. Simulation results match the analytical bounds in Lemma 5 under different channel conditions. Firstly, it can be seen that D2D communications achieve a higher transmission rate compared with cellular communications due to short distances, which means a low content retrieval delay via D2D communications. Then, we observe a sharp performance degradation with the growth of the D2D user density, i.e., the transmission rate decreases from 4 Gbit/s to only 2 Gbit/s when the D2D user density increases from 40 to 800 per km^2 for $\alpha = 1.6$. For this reason is that the desired signal power keeps unchanged as D2D communication distance is independent of D2D user density, while the interference increases drastically due to decreasing interference link distances with the D2D user density. Hence, a coordinated scheduling scheme is required to enhance D2D transmission performance in dense networks.

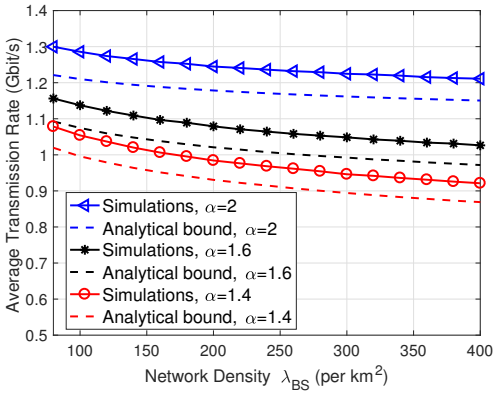

(a) The nearest SBS transmission rate

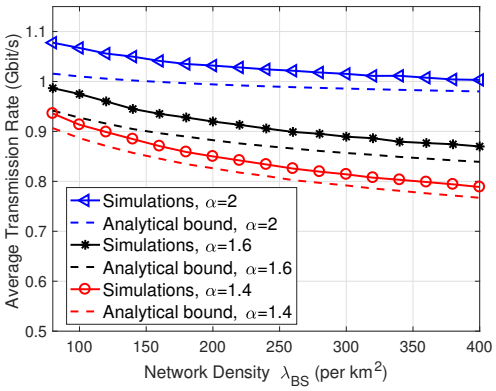

(b) SBS cluster transmission rate

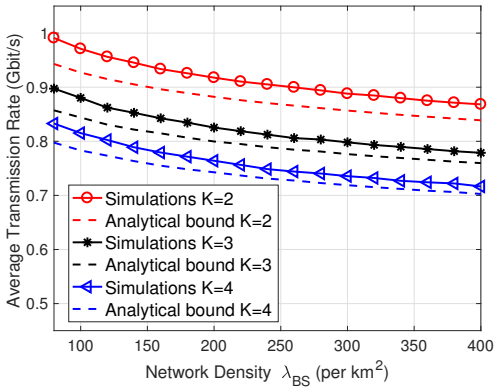

(c) SBS cluster transmission rate with respect to the cluster size

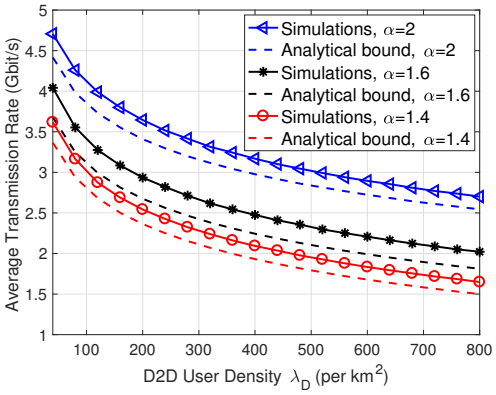

(d) D2D transmission rate

Fig. 5.3: Transmission performance with respect to different system parameters.

5.6.4 Content Retrieval Delay

We investigate the content retrieval delay performance with different caching policies with respect to the content popularity, the network density, the backhaul capacity and the cluster size, respectively.

Figure 5.4(a) shows the impact of the content popularity skewness on the average content retrieval delay. The proposed policy outperforms the MPC policy in the low popularity skewness region because low concentrated content request applications favor large cache capacity. For example, the DCEC policy with four SBSs reduces 48% content

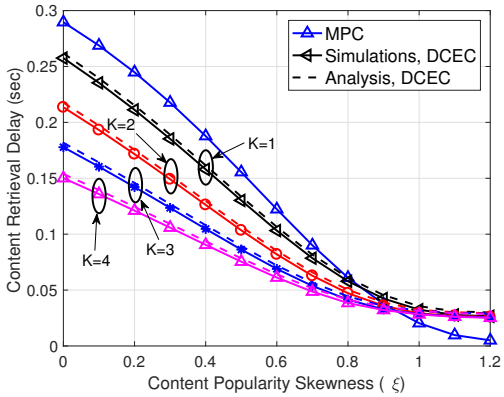

(a) Content popularity

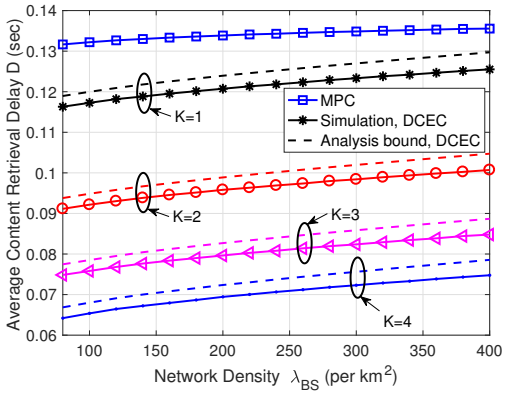

(b) Network density

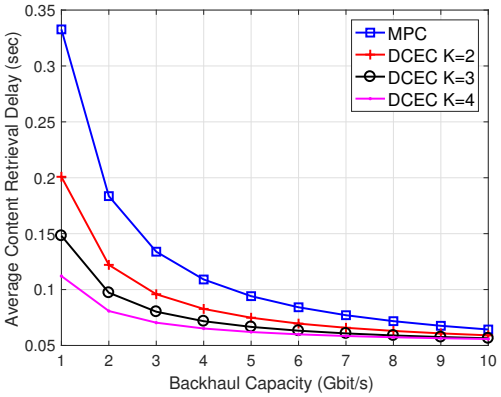

(c) Backhaul capacity

Fig. 5.4: Content retrieval delay with respect to different system parameters.

retrieval delay compared with the MPC policy for $\xi = 0.6$. However, the performance gain provided by the DCEC policy vanishes with the increase of the content popularity skewness, which further validates the fact that DCEC policy favors less concentrated content request applications.

The content retrieval delay performance in terms of the network density is studied for $\xi = 0.56$, as shown in Fig. 5.4(b). Firstly, simulation results and analytical bounds are highly consistent with each other. Secondly, the content retrieval delay increases with the growth of the network density, because both cellular and D2D transmission rates decrease in dense networks. For illustration, users spend about 23% more time to retrieve contents

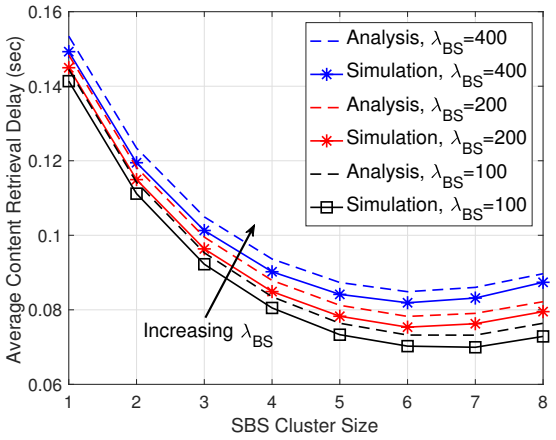

Fig. 5.5: The impact of SBS cluster size on the content retrieval delay.

when the network density increases from 80 to 400 per km^2 for $K = 4$. More importantly, with high-rate cellular and D2D communications, the proposed caching policy with four SBSs reduces as much as 45% content retrieval delay compared with the MPC policy.

As shown in Fig. 5.4(c), we plot the average transmission delay in terms of the backhaul capacity. It can be observed that the performance gain acquired by the DCEC policy vanishes with the increase of backhaul capacity. When the constraint backhaul capacity acts as the bottleneck of the system performance, the proposed policy cooperatively cache more contents in edge networks to reduce the content retrieval delay. However, with unconstrained backhaul capacity, the performance gain degrades because users are able to fetch contents with low latency from remote servers.

Figure 5.5 shows the impact of the SBS cluster size on the average content retrieval delay for $\lambda_{BS} = 100, 200, 400$. As aforementioned, there exists a tradeoff between the transmission efficiency and the caching diversity. We observe that the average content retrieval delay decreases and then increases with the growth of SBS cluster size. When the SBS cluster size is too large, the benefit of cooperative edge caching vanishes. The reason is that a large SBS cluster size caches more popular contents while reduces the average SBS cluster transmission rate due to long physical distances to fetch contents. In addition, the tradeoff relationship between caching diversity and transmission performance indicates the optimal SBS cluster size exists. Specifically, the optimal cluster size is 7 for $\lambda_{BS} = 100$, while when the network density increases to 400 per km^2, the optimal SBS cluster size decreases to 6.

Furthermore, Fig. 5.6 presents the optimal SBS cluster size with respect to the backhaul

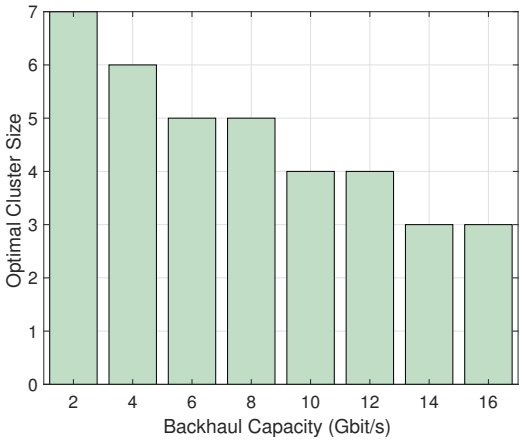

Fig. 5.6: Optimal SBS cluster size with respect to backhaul capacity.

capacity. We observe that the optimal cluster size decreases with the increase of backhaul capacity, which means that a large SBS cluster size is preferred in the backhaul constrained scenario. The reason is that the increase of backhaul capacity alleviates the performance gain provided by the DCEC policy. For illustration, the optimal cluster size is 7 for 2 Gbit/s, while when the backhaul capacity increases to 16 Gbit/s, the optimal SBS cluster size decreases to 3.

5.7 Summary

In this chapter, a D2D-assisted cooperative edge caching has been proposed in mmWave dense networks. The closed-form expressions of backhaul offloading and content retrieval delay performance of the proposed policy have been obtained taking the practical directional antennas model and the network density into consideration. Both analytical and simulation results have revealed the average content retrieval delay increases with the network density. Besides, the tradeoff relationship between caching diversity and transmission efficiency has been investigated. Comparing with state-of-the-art MPC policy via extensive simulations, the proposed caching policy provides significant performance gains in both backhaul traffic offloading and content retrieval delay.

5.8 Appendix

5.8.1 Proof of Lemma 5

When a user is served by its D2D peer via mmWave D2D communications, the received signal power is given by

$$S_D = P_U (G_u^m)^2 h_1 C r_d^{-\alpha}. \tag{5.46}$$

The received interference power which consists of the received signal from all the other D2D transmitters Φ_D, is

$$I_D = \sum_{i \in \Phi_D} P_U G_u(\theta_{t,i}) G_u(\theta_{r,i}) h_i C r_i^{-\alpha} \tag{5.47}$$

where r_i is the distance between the user and i-th D2D interferers.

Similarly, the average D2D transmission rate is lower bounded by

$$\begin{aligned}
\mathbb{E}[R_D] &= \phi W \log_2 \left(1 + \frac{S_D}{I_D + \sigma^2}\right) \\
&\geq \frac{\phi W}{\ln 2} \left(\mathbb{E}[\ln S_D] - \ln \sum_{i \in \Phi_D} \mathbb{E}[I_D^i]\right) \\
&\geq \frac{\phi W}{\ln 2} \left(2 \ln \frac{G_u^m}{\bar{G}_u} - \gamma - \alpha \mathbb{E}[\ln r_d] - \ln \sum_{i \in \Phi_D} \mathbb{E}[r_i^{-\alpha}]\right).
\end{aligned} \tag{5.48}$$

Following the similar step in (5.24), with PDF of r_d in (5.1), $\mathbb{E}[\ln r_d]$ is given by

$$\begin{aligned}
\mathbb{E}[\ln r_d] &= \int_0^{r_d^{max}} \ln r_d \frac{2 r_d}{(r_d^{max})^2} dr_d \\
&= \ln r_d^{max} - \frac{1}{2}.
\end{aligned} \tag{5.49}$$

Then, for the second term in (5.48), $\sum_{i \in \Phi_D} \mathbb{E}[r_i^{-\alpha}]$ is obtained in the following step. r_i represents the inter-node distances of PPP, which follows a generalized beta distribution

[114]. The $-\alpha$th moment of r_i is given by

$$\mathbb{E}[r_i^{-\alpha}] = \begin{cases} \dfrac{R^{-\alpha}\Gamma(N_D+1)\Gamma(i-\frac{\alpha}{2})}{\Gamma(i)\Gamma(N_D+1-\frac{\alpha}{2})}, & \alpha < 2 \\ \infty, & \alpha \geq 2 \end{cases} \tag{5.50}$$

where $R = \sqrt{\frac{N_D}{\pi\lambda_D}}$ is the equivalent cell radius and N_D is the number of D2D users. The summation of the $-\alpha$th moments of r_i can be represented into different forms when α attains different values.

- When $\alpha < 2$, the summation of moments of r_i is given by

$$\begin{aligned} \sum_{i\in\Phi_D} \mathbb{E}[r_i^{-\alpha}] &= \frac{R^{-\alpha}\Gamma(N_D+1)}{\Gamma(N_D+1-\frac{\alpha}{2})} \sum_{i=1}^{N_D} \frac{\Gamma(i-\frac{\alpha}{2})}{\Gamma(i)} \\ &= \pi\lambda_D \frac{R^{2-\alpha}}{1-\frac{\alpha}{2}} \end{aligned} \tag{5.51}$$

  where the last the step due to the fact $\pi R^2\lambda_D = N_D$.

- When $\alpha > 2$, the moment of r_i becomes unbounded because the path loss model we adopt break down at short distances. Applying the guard radius d_0 around every receiver, i.e., the transmitters within d_0 are not allowed to transmit. The sum of interference within d_0 is $\pi\lambda_D d_0^{2-\alpha}/(1-\frac{\alpha}{2})$ according to (5.51). Excluding the interference within the guard radius, we have

$$\sum_{i\in\Phi_D} \mathbb{E}[r_i^{-\alpha}] = \pi\lambda_D \frac{R^{2-\alpha} - d_0^{2-\alpha}}{1-\frac{\alpha}{2}}. \tag{5.52}$$

- When $\alpha = 2$, taking the limit of (5.52), we obtain

$$\sum_{i\in\Phi_D} \mathbb{E}[r_i^{-\alpha}] = 2\pi\lambda_D \ln\left(\frac{R}{d_0}\right). \tag{5.53}$$

Substituting (5.49), (5.51), (5.52) and (5.53) into (5.48), Lemma 5 is proved.

Chapter 6

Conclusions and Future Work

6.1 Conclusions

This dissertation reports our research work on enhancing the performance of mmWave networks. Considering the distinct high directionality feature of mmWave communications, our target is to explore the efficient and, more importantly, practical solutions. To this end, a comprehensive and systematic study which analyzes and designs the communication layers to address those new challenges is necessary. In this chapter, based on the analysis and discussion provided, we present the following remarks.

6.1.1 Beam Alignment Scheme Design

From the perspective of physical layer, both transmitter and receiver must align their beams in order to establish reliable communication links. The BA process, however, may incur significant latency on the order of seconds due to the prohibitive complexity of searching the entire beam space. In Chapter 3, our goal is to develop an efficient BA solution for mmWave communications. To this end, we have formulated the BA problem as an MAB problem and then proposed the learning-based HBA algorithm to solve the MAB problem. The HBA algorithm leverages the correlation structure among beams and the prior knowledge on the channel fluctuation to speed up the BA process. Theoretical analysis characterizes the asymptotically optimality and convergence speed of the proposed algorithm. Using extensive simulations, we verify the effectiveness of the proposed algorithm as compared to existing BA method in 802.11ad.

6.1.2 MAC Performance Evaluation and Enhancement

To coordinate the BF training for multiple users, 802.11ad requires all the users to distributedly compete for BF training resources, which results in severe collisions in the BF training stage. Thus, how to configure MAC parameters towards the global welfare of the system is a fundamental issue of a mmWave network. In order to conduct effective network management, the accurate evaluation of the MAC performance is of paramount importance. This motivates our research on the evaluation of MAC performance in mmWave networks. In Chapter 4 of the dissertation, we focus on BFT-MAC which is specified by 802.11ad, and have established a simple yet accurate analytical model to evaluate the performance of BFT-MAC. Based on the analytical model, the normalized throughput and average BF training latency have been derived with different user densities and configurations of BFT-MAC. The proposed analytical model provides insightful guidance on practical configurations of BFT-MAC under different scenarios. To enhance the performance of BFT-MAC in high user density scenarios, we have proposed an enhancement scheme which adaptively configures the MAC parameters based on the user density. Lastly, extensive simulations are carried out, and the results validate the accuracy of the proposed analytical model and the effectiveness of the proposed enhancement scheme.

6.1.3 Backhaul Alleviation Scheme Design

From the perspective of network deployment, deploying unconstrained wired backhaul links in mmWave dense networks is infeasible due to prohibitive costs especially in urban scenarios, which results in backhaul congestion. Thus, to effectively alleviate the burden of backhaul links is an imperative issue. In this case, we can rely on the emerging edge caching technology which proactively stores popular contents during off-peak hours and distributes contents to mobile users in proximity. In Chapter 5, we target at developing efficient caching policy to alleviate the backhaul congestion and reduce content retrieval delay in mmWave dense networks. We have proposed the DCEC policy which jointly leverages the caching resources of both mobile users and SBSs to enlarge the set of cached contents. Taking the directional antenna and network density into consideration, we have applied the stochastic geometry theory to derive the closed-form expressions on the content retrieval delay performance with our proposed caching policy. Analytical results provide important guidelines for future mmWave deployment. Comprehensive simulation results validate the accuracy of our analytical results and demonstrate that the proposed caching policy can effectively alleviate the backhaul burden.

6.2 Future Research Directions

Towards enhancing the mmWave networks and improving the QoS of mobile users, there are still many open issues remain to be solved. Next, we outline several important directions for future work.

6.2.1 Beam Alignment Under High Mobility

It is well-known that the performance of mmWave networks significantly degrades in high mobility scenarios. The reason is two-fold. Firstly, user mobility changes the beam direction which results in beam misalignment and frequently breaks the established communication links. Secondly, due to high mobility, mobile users usually suffer from the blockage issue. For example, in vehicular mmWave networks, vehicle users not only need to frequently align their beams with roadside BSs, but also deal with the blockage caused by either buildings or other vehicles (e.g., bus and tram). Thus, the established mmWave link is intermittent and short-lived, which may experience a high link outage probability. How to establish reliable mmWave communication links in mobile scenarios is a challenging issue. As high-mobility users usually moves along a specific trajectory, such as vehicles obey the road lane to travel, to explore the trajectory information of mobile users is a practical and potential solution to enhance mmWave communications in high mobility scenarios. For example, based on the velocity and moving direction of a vehicle, BS can predict the future positions of the vehicle so as to proactively align their beams before the link outage occurs. However, as the real-time moving direction and location information are usually unknown to BS *a priori*, an efficient and effective prediction scheme is necessary to optimally determine the beam direction based on the trajectory feature of mobile users and meanwhile maximize their QoS.

6.2.2 Efficient QoS-aware MAC Protocol

Compared with that the physical layer techniques of mmWave networks have been well studied, such as BF, research from the perspective of MAC layer is relatively underdeveloped. Even with efficient physical layer schemes, a coarse MAC protocol would still lead to poor network performance. The MAC design emerges as a new bottleneck of the entire mmWave network due to the following two reasons. Firstly, based on our analytical results in Chapter 4, the MAC throughput in the BF training stage degrades greatly in high user density scenarios, which limits the application of mmWave networks in dense

user scenarios. Secondly, since the traffic types become diverse, future mmWave networks should support heterogeneous traffic while satisfying various QoS requirements. However, MAC protocols in mmWave networks are not only inefficient, but also do not consider the QoS requirements of different users. Thus, designing an efficient yet QoS-aware MAC protocol is of paramount importance for future mmWave networks.

6.2.3 Blockage-aware mmWave Network

The blockage problem is considered as one of thorny open issues for mmWave networks, especially in indoor scenarios. The mmWave connection can be easily interrupted when the LOS path is blocked by the human body or indoor infrastructure (e.g., pillar and desk), which results in high link outage probability and intermittent connection. When link outage occurs, the link will be re-established, which results in frequent beam realignment with increased latency. In addition, the latency caused by the link outage will be amplified at higher layers. For example, at the transport layer, link outage may be treated as time-out so that transmission control protocol (TCP) connections may be re-established, which further exacerbates the latency. Since a mobile user cannot be always served by one BS, to explore a user-centric framework that a mobile user can be simultaneously served by multiple BSs, is a practical solution for blockage-aware mmWave networks. Specifically, when the connection between a mobile user and a BS is blocked, the system detects this blockage and proactively activates another connection between the mobile user and another BS. In this proactive manner, the latency caused by link establishment can be ignored since the backup connection is established in time once the blockage occurs. However, how to accurately and proactively identify blockage is a challenging issue. In addition, an effective yet low complexity link re-establishment solution between the mobile user and all BSs, requires further investigation.

References

[1] International Data Corporation, "Augmented reality and virtual reality headsets poised for significant growth," 2019. [Online]. Available: https://www.idc.com/getdoc.jsp?containerId=prUS44966319.

[2] Cisco, "Cisco visual networking index: Global mobile data traffic forecast update, 2017-2022 white paper," 2019. [Online]. Available: https://www.cisco.com/c/en/us/solutions/collateral/service-provider/visual-networking-index-vni/white-paper-c11-741490.html.

[3] O. Abari, D. Bharadia, A. Duffield, and D. Katabi, "Enabling high-quality untethered virtual reality," in *Proc. USENIX NSDI*, 2017, pp. 531–544.

[4] I. Chih-Lin, C. Rowell, S. Han, Z. Xu, G. Li, and Z. Pan, "Toward green and soft: A 5G perspective," *IEEE Commun. Mag.*, vol. 52, no. 2, pp. 66–73, 2014.

[5] K. Aldubaikhy, W. Wu, N. Zhang, N. Cheng, and X. Shen, "mmwave IEEE 802.11ay for 5G fixed wireless access," *IEEE Wireless Mag.*, submitted.

[6] D. T. Emerson, "The work of Jagadis Chandra Bose: 100 years of millimeter-wave research," *IEEE Trans. Microw. Theory Techn.*, vol. 45, no. 12, pp. 2267–2273, 1997.

[7] T. Bai and R. W. Heath, "Coverage and rate analysis for millimeter-wave cellular networks," *IEEE Trans. Wireless Commun.*, vol. 14, no. 2, pp. 1100–1114, 2015.

[8] R. W. Heath, N. Gonzalez-Prelcic, S. Rangan, W. Roh, and A. M. Sayeed, "An overview of signal processing techniques for millimeter wave MIMO systems," *IEEE J. Sel. Topics Signal Process.*, vol. 10, no. 3, pp. 436–453, 2016.

[9] A. Alkhateeb, G. Leus, and R. W. Heath, "Limited feedback hybrid precoding for multi-user millimeter wave systems," *IEEE Trans. Wireless Commun.*, vol. 14, no. 11, pp. 6481–6494, 2015.

[10] W. Wu, Q. Shen, K. Aldubaikhy, N. Cheng, N. Zhang, and X. Shen, "Enhance the edge with beamforming: Performance analysis of beamforming-enabled WLAN," in *Proc. IEEE WiOpt*, 2018.

[11] IEEE Standards, "IEEE standards 802.11 ad-2012: Enhancement for very high throughput in the 60 GHz band," 2012.

[12] IEEE Standards Association, "IEEE standards 802.15.3c-2009: Millimeter-wave-based alternate physical layer extension," 2009.

[13] T. Wei and X. Zhang, "Pose information assisted 60 Ghz networks: Towards seamless coverage and mobility support," in *Proc. ACM MOBICOM*, 2017, pp. 42–55.

[14] J. G. Andrews, S. Buzzi, W. Choi, S. V. Hanly, A. Lozano, A. C. Soong, and J. C. Zhang, "What will 5G be?" *IEEE J. Sel. Areas Commun.*, vol. 32, no. 6, pp. 1065–1082, 2014.

[15] H. T. Friis, "A note on a simple transmission formula," *Proc. IRE*, vol. 34, no. 5, pp. 254–256, 1946.

[16] M. Xiao, S. Mumtaz, Y. Huang, L. Dai, Y. Li, M. Matthaiou, G. K. Karagiannidis, E. Björnson, K. Yang, and I. Chih-Lin, "Millimeter wave communications for future mobile networks," *IEEE J. Sel. Areas Commun.*, vol. 35, no. 9, pp. 1909–1935, 2017.

[17] E-Band Communications, "E-band technology," [Online]. Available: http://www.e-band.com/index.php?id=86.

[18] mmMAGIC, "Measurement campaigns and initial channel models for preferred suitable frequency ranges," 2016. [Online]. Available: https://5g-mmmagic.eu/results/deliverable.

[19] V. E. A. Maltsev, "Channel Models for 60 GHz WLAN Systems," *doc.: IEEE 802.11-09/0334r8*, no. 3.

[20] Z. Pi and F. Khan, "An introduction to millimeter-wave mobile broadband systems," *IEEE Commun. Mag.*, vol. 49, no. 6, 2011.

[21] C. R. Anderson and T. S. Rappaport, "In-building wideband partition loss measurements at 2.5 and 60 GHz," *IEEE Trans. Wireless Commun.*, vol. 3, no. 3, pp. 922–928, 2004.

[22] S. Sur, X. Zhang, P. Ramanathan, and R. Chandra, "BeamSpy: Enabling robust 60 GHz links under blockage," in *Proc. USENIX NSDI*, 2016, pp. 193–206.

[23] M. Samimi, K. Wang, Y. Azar, G. N. Wong, R. Mayzus, H. Zhao, J. K. Schulz, S. Sun, F. Gutierrez, and T. S. Rappaport, "28 GHz angle of arrival and angle of departure analysis for outdoor cellular communications using steerable beam antennas in New York City," in *Proc. IEEE VTC Spring*, 2013, pp. 1–6.

[24] A. Maltsev, R. Maslennikov, A. Sevastyanov, A. Khoryaev, and A. Lomayev, "Experimental investigations of 60 GHz WLAN systems in office environment," *IEEE J. Sel. Areas Commun.*, vol. 27, no. 8, pp. 1488–1499, 2009.

[25] Y. Shabara, C. E. Koksal, and E. Ekici, "Linear block coding for efficient beam discovery in millimeter wave communication networks," in *Proc. IEEE INFOCOM*, 2018, pp. 2285–2293.

[26] R. Méndez-Rial, C. Rusu, N. González-Prelcic, A. Alkhateeb, and R. W. Heath, "Hybrid MIMO architectures for millimeter wave communications: Phase shifters or switches?" *IEEE Access*, vol. 4, pp. 247–267, 2016.

[27] F. Sohrabi and W. Yu, "Hybrid digital and analog beamforming design for large-scale antenna arrays," *IEEE J. Sel. Topics Signal Process.*, vol. 10, no. 3, pp. 501–513, 2016.

[28] A. Alkhateeb and R. W. Heath, "Frequency selective hybrid precoding for limited feedback millimeter wave systems," *IEEE Trans. Commun.*, vol. 64, no. 5, pp. 1801–1818, 2016.

[29] C. Rusu, R. Méndez-Rial, N. González-Prelcicy, and R. W. Heath, "Low complexity hybrid sparse precoding and combining in millimeter wave MIMO systems," in *Proc. IEEE ICC*, 2015, pp. 1340–1345.

[30] A. Alkhateeb, O. El Ayach, G. Leus, and R. W. Heath, "Hybrid precoding for millimeter wave cellular systems with partial channel knowledge," in *Proc. IEEE ITA*, 2013, pp. 1–5.

[31] A. Khalid, W. Wen, Y. Qiang, and S. Xuemin, "Low-complexity user selection algorithm for multiuser transmission in mmwave WLANs," *Trans. Wireless Commun.*, submitted.

[32] W. Wu, Q. Shen, M. Wang, and X. Shen, "Performance analysis of IEEE 802.11. ad downlink hybrid beamforming," in *Proc. IEEE ICC*, 2017.

[33] Y. Ghasempour, C. R. da Silva, C. Cordeiro, and E. W. Knightly, "IEEE 802.11 ay: Next-generation 60 GHz communication for 100 Gb/s Wi-Fi," *IEEE Commun. Mag.*, vol. 55, no. 12, pp. 186–192, 2017.

[34] A. Loch, G. Bielsa, and J. Widmer, "Practical lower layer 60 GHz measurements using commercial off-the-shelf hardware," in *Proc. ACM WiNTECH*, 2016, pp. 9–16.

[35] M. Boers, B. Afshar, I. Vassiliou, S. Sarkar, S. T. Nicolson, E. Adabi, B. G. Perumana, T. Chalvatzis, S. Kavvadias, P. Sen *et al.*, "A 16TX/16RX 60 GHz 802.11 ad chipset with single coaxial interface and polarization diversity," *IEEE J. Solid-State Circuits*, vol. 49, no. 12, pp. 3031–3045, 2014.

[36] ABI Research, "802.11ad will vastly enhance wi-fi: The Importance of the 60 GHz Band to Wi-Fi's Continued Evolution," 2016. [Online]. Available: https://www.qualcomm.com/media/documents/files/abi-research-802-11ad-will-vastly-enhance-wi-fi.pdf.

[37] T. S. Rappaport, S. Sun, R. Mayzus, H. Zhao, Y. Azar, K. Wang, G. N. Wong, J. K. Schulz, M. Samimi, and F. Gutierrez, "Millimeter wave mobile communications for 5G cellular: It will work!" *IEEE Access*, vol. 1, pp. 335–349, 2013.

[38] T. L. Lai and H. Robbins, "Asymptotically efficient adaptive allocation rules," *Adv. Appl. Math.*, vol. 6, pp. 4–22, 1985.

[39] P. Auer, N. Cesa-Bianchi, and P. Fischer, "Finite-time analysis of the multiarmed bandit problem," *Mach. Learn.*, vol. 47, no. 2, pp. 235–256, 2002.

[40] P. B. Reverdy, V. Srivastava, and N. E. Leonard, "Modeling human decision making in generalized Gaussian multiarmed bandits," *Proc. IEEE*, vol. 102, no. 4, pp. 544–571, 2014.

[41] Z. Wang and C. Shen, "Small cell transmit power assignment based on correlated bandit learning," *IEEE J. Sel. Areas Commun.*, vol. 35, no. 5, pp. 1030–1045, 2017.

[42] W. Chen, Y. Wang, and Y. Yuan, "Combinatorial multi-armed bandit: General framework and applications," in *Proc. ICML*, 2013, pp. 151–159.

[43] L. Chen, J. Xu, and Z. Lu, "Contextual combinatorial multi-armed bandits with volatile arms and submodular reward," in *Proc. NIPS*, 2018, pp. 3247–3256.

[44] C. Shen, R. Zhou, C. Tekin, and M. van der Schaar, "Generalized global bandit and its application in cellular coverage optimization," *IEEE J. Sel. Topics Signal Process.*, vol. 12, no. 1, pp. 218–232, 2018.

[45] C. Claus and C. Boutilier, "The dynamics of reinforcement learning in cooperative multiagent systems," *AAAI/IAAI*, vol. 1998, pp. 746–752, 1998.

[46] S. Bubeck, N. Cesa-Bianchi *et al.*, "Regret analysis of stochastic and nonstochastic multi-armed bandit problems," *Foundations and Trends® in Machine Learning*, vol. 5, no. 1, pp. 1–122, 2012.

[47] J. Qiao, Y. He, and X. Shen, "Proactive caching for mobile video streaming in millimeter wave 5G networks." *IEEE Trans. Wireless Commun.*, vol. 15, no. 10, pp. 7187–7198, 2016.

[48] M. Hashemi, A. Sabharwal, C. E. Koksal, and N. B. Shroff, "Efficient beam alignment in millimeter wave systems using contextual bandits," in *Proc. IEEE INFOCOM*, 2018, pp. 2393–2401.

[49] H. Hassanieh, O. Abari, M. Rodriguez, M. Abdelghany, D. Katabi, and P. Indyk, "Fast millimeter wave beam alignment," in *Proc. ACM SIGCOMM*, 2018, pp. 432–445.

[50] Z. Marzi, D. Ramasamy, and U. Madhow, "Compressive channel estimation and tracking for large arrays in mm-Wave picocells," *IEEE J. Sel. Topics Signal Process.*, vol. 10, no. 3, pp. 514–527, 2016.

[51] S. Sur, I. Pefkianakis, X. Zhang, and K. H. Kim, "WiFi-assisted 60 GHz wireless networks," in *Proc. ACM MOBICOM*, 2017, pp. 28–41.

[52] P. Zhou, X. Fang, Y. Fang, Y. Long, R. He, and X. Han, "Enhanced random access and beam training for millimeter wave wireless local networks with high user density," *IEEE Trans. Wireless Commun.*, vol. 16, no. 12, pp. 7760–7773, 2017.

[53] J. Wang, Z. Lan, C. Pyo, T. Baykas, C. Sum, M. A. Rahman, J. Gao, R. Funada, F. Kojima, H. Harada, and S. Kato, "Beam codebook based beamforming protocol for multi-Gbps millimeter-wave WPAN systems," *IEEE J. Sel. Areas Commun.*, vol. 27, no. 8, pp. 1390–1399, 2009.

[54] Z. Xiao, T. He, P. Xia, and X.-G. Xia, "Hierarchical codebook design for beamforming training in millimeter-wave communication," *IEEE Trans. Wireless Commun.*, vol. 15, no. 5, pp. 3380–3392, 2016.

[55] X. Sun, C. Qi, and G. Y. Li, "Beam training and allocation for multiuser millimeter wave massive MIMO systems," *IEEE Trans. Wireless Commun.*, vol. 18, no. 2, pp. 1041–1053, 2019.

[56] A. Ali, N. González-Prelcic, and R. W. Heath, "Millimeter wave beam-selection using out-of-band spatial information," *IEEE Trans. Wireless Commun.*, vol. 17, no. 2, pp. 1038–1052, 2018.

[57] M. Hashemi, C. E. Koksal, and N. B. Shroff, "Out-of-band millimeter wave beamforming and communications to achieve low latency and high energy efficiency in 5G systems," *IEEE Trans. Commun.*, vol. 66, no. 2, pp. 875–888, 2018.

[58] P. Yang, N. Zhang, S. Zhang, L. Yu, J. Zhang, and X. Shen, "Content popularity prediction towards location-aware mobile edge caching," *IEEE Trans. Multimedia*, vol. 21, no. 4, pp. 915–929, 2019.

[59] S. Müller, O. Atan, M. van der Schaar, and A. Klein, "Context-aware proactive content caching with service differentiation in wireless networks," *IEEE Trans. Wireless Commun.*, vol. 16, no. 2, pp. 1024–1036, 2017.

[60] P. Yang, N. Zhang, S. Zhang, K. Yang, L. Yu, and X. Shen, "Identifying the most valuable workers in fog-assisted spatial crowdsourcing," *IEEE Internet of Things J.*, vol. 4, no. 5, pp. 1193–1203, 2017.

[61] Y. Sun, S. Zhou, and J. Xu, "EMM: Energy-aware mobility management for mobile edge computing in ultra dense networks," *IEEE J. Sel. Areas Commun.*, vol. 35, no. 11, pp. 2637–2646, 2017.

[62] N. Gulati and K. R. Dandekar, "Learning state selection for reconfigurable antennas: A multi-armed bandit approach," *IEEE Trans. Antennas Propag.*, vol. 62, no. 3, pp. 1027–1038, 2014.

[63] G. H. Sim, S. Klos, A. Asadi, A. Klein, and M. Hollick, "An online context-aware machine learning algorithm for 5G mmWave vehicular communications," *IEEE/ACM Trans. Netw.*, vol. 26, no. 6, pp. 2487–2500, 2018.

[64] I. Chafaa, E. V. Belmega, and M. Debbah, "Adversarial multi-armed bandit for mmwave beam alignment with one-bit feedback," in *Proc. ACM ValueTools*, 2019.

[65] M. R. Akdeniz, Y. Liu, S. Sun, S. Rangan, T. S. Rappaport, and E. Erkip, "Millimeter wave channel modeling and cellular capacity evaluation," *IEEE J. Sel. Areas Commun.*, vol. 32, no. 6, pp. 1164–1179, 2013.

[66] S. Bubeck, G. Stoltz, C. Szepesvári, and R. Munos, "Online optimization in X-armed bandits," in *Proc. NIPS*, 2009.

[67] W. Wu, N. Zhang, N. Cheng, Y. Tang, K. Aldubaikhy, and X. Shen, "Beef up mmwave dense cellular networks with D2D-assisted cooperative edge caching," *IEEE Trans. Veh. Technol.*, vol. 68, no. 4, pp. 3890–3904, 2019.

[68] FCC, "Report and order and further notice of proposed rulemaking, federal communications commission," 2016.

[69] J. Du and R. A. Valenzuela, "How much spectrum is too much in millimeter wave wireless access," *IEEE J. Sel. Areas Commun.*, vol. 35, no. 7, pp. 1444–1458, 2017.

[70] 3GPP, "Technical specification group radio access network: Study on channel model for frequencies from 0.5 to 100 GHz," 2017.

[71] Z. Marzi, D. Ramasamy, and U. Madhow, "Compressive channel estimation and tracking for large arrays in mm-wave picocells," *IEEE J. Sel. Topics Signal Process.*, vol. 10, no. 3, pp. 514–527, 2016.

[72] G. Bianchi, "Performance analysis of the IEEE 802.11 distributed coordination function," *IEEE J. Sel. Areas Commun.*, vol. 18, no. 3, pp. 535–547, Mar. 2000.

[73] T. H. Luan, X. Ling, and X. Shen, "MAC in motion: Impact of mobility on the MAC of drive-thru Internet," *IEEE Trans. Mobile Comput.*, vol. 11, no. 2, pp. 305–319, Feb. 2012.

[74] W. Xu, W. Shi, F. Lyu, H. Zhou, N. Cheng, and X. Shen, "Throughput analysis of vehicular Internet access via roadside WiFi hotspot," *IEEE Trans. Veh. Technol.*, vol. 68, no. 4, pp. 3980–3991, Apr. 2019.

[75] Q. Ye, W. Zhuang, L. Li, and P. Vigneron, "Traffic-load-adaptive medium access control for fully connected mobile ad hoc networks," *IEEE Trans. Veh. Technol.*, vol. 65, no. 11, pp. 9358–9371, Nov. 2016.

[76] ——, "Traffic-load-adaptive medium access control for fully connected mobile ad hoc networks," *IEEE Trans. Veh. Technol.*, vol. 65, no. 11, pp. 9358–9371, 2016.

[77] X. Yuan, C. Li, Q. Ye, K. Zhang, N. Cheng, N. Zhang, and X. Shen, "Performance analysis of IEEE 802.15.6-based coexisting mobile WBANs with prioritized traffic and dynamic interference," *IEEE Trans. Wireless Commun.*, vol. 17, no. 8, pp. 5637–5652, Aug. 2018.

[78] K. Chandra, V. Prasad, and I. Niemegeers, "Performance analysis of IEEE 802.11ad MAC protocol," *IEEE Commun. Lett.*, vol. 21, no. 7, pp. 1513 – 1516, Jul. 2017.

[79] Q. Chen, J. Tang, D. T. C. Wong, X. Peng, and Y. Zhang, "Directional cooperative MAC protocol design and performance analysis for IEEE 802.11 ad WLANs," *IEEE Trans. Veh. Techol.*, vol. 62, no. 6, pp. 2667–2677, Jul. 2013.

[80] S. Shao, H. Zhang, D. Koutsonikolas, and A. Khreishah, "Two-dimensional reduction of beam training overhead in crowded 802.11ad based networks," in *Proc. IEEE INFOCOM Workshops*, 2018, pp. 680–685.

[81] S. G. Kim, K. Jo, S. Park, H. Cho, J. Kim, and S. Bang, "On random access in A-BFT," *IEEE 802.11 Documents, doc.:IEEE 802.11-16/0948-00-00ay*, Jul. 2016.

[82] Y. Xin, R. Sun, and O. Aboul-Magd, "Channel access in A-BFT over multiple channels," *IEEE 802.11 Documents, doc.:IEEE 802.11-16/0101r0*, Jan. 2016.

[83] K. Jo, S. Park, H. Cho, J. Kim, S. Bang, and S. G. Kim, "Short SSW frame for A-BFT," *IEEE 802.11 Documents, doc.:IEEE 802.11-17/0117-00-00ay*, Jan. 2017.

[84] P. Zhou, K. Cheng, X. Han, X. Fang, Y. Fang, R. He, Y. Long, and Y. Liu, "IEEE 802.11ay-based mmWave WLANs: Design challenges and solutions," *IEEE Commun. Surveys Tuts.*, vol. 20, no. 3, pp. 1654–1681, 3rd Quart. 2018.

[85] N. Cheng, F. Lyu, J. Chen, W. Xu, H. Zhou, S. Zhang, and X. Shen, "Big data driven vehicular networks," *IEEE Network*, vol. 32, no. 6, pp. 160–167, 2018.

[86] N. Cheng, H. Zhou, L. Lei, N. Zhang, Y. Zhou, X. Shen, and F. Bai, "Performance analysis of vehicular device-to-device underlay communication," *IEEE Trans. Veh. Technol.*, vol. 66, no. 6, pp. 5409–5421, 2017.

[87] E. Bastug, M. Bennis, and M. Debbah, "Living on the edge: The role of proactive caching in 5G wireless networks," *IEEE Commun. Mag.*, vol. 52, no. 8, pp. 82–89, 2014.

[88] Y. Zhong, M. Haenggi, F. Zheng, W. Zhang, T. Q. Quek, and W. Nie, "Towards a tractable delay analysis in ultra-dense networks," *IEEE Commun. Mag.*, vol. 55, no. 12, pp. 103–109, 2017.

[89] "Mobile-edge computing - introductory technical white paper," *European Telecommunications Standards Institute, Tech.*, Rep., Sep. 2014, accessed Mar. 27, 2017.[Online]. Available: https: //portal.etsi.org/.

[90] F. Lyu, H. Zhu, H. Zhou, W. Xu, N. Zhang, M. Li, and X. Shen, "SS-MAC: A novel time slot-sharing MAC for safety messages broadcasting in VANETs," *IEEE Trans. Veh. Technol.*, vol. 67, no. 4, pp. 3586–3597, 2018.

[91] T. G. Rodrigues, K. Suto, H. Nishiyama, and N. Kato, "Hybrid method for minimizing service delay in edge cloud computing through VM migration and transmission power control," *IEEE Trans. Comput.*, vol. 66, no. 5, pp. 810–819, 2017.

[92] T. G. Rodrigues, K. Suto, H. Nishiyama, N. Kato, and K. Temma, "Cloudlets activation scheme for scalable mobile edge computing with transmission power control and virtual machine migration," *IEEE Trans. Comput.*, vol. 67, no. 9, pp. 1287–1300, 2018.

[93] Y. Zhou, F. R. Yu, J. Chen, and Y. Kuo, "Resource allocation for information-centric virtualized heterogeneous networks with in-network caching and mobile edge computing," *IEEE Trans. Veh. Technol.*, vol. 66, no. 12, pp. 11 339–11 351, 2017.

[94] J. Liu, H. Nishiyama, N. Kato, and J. Guo, "On the outage probability of device-to-device-communication-enabled multichannel cellular networks: An RSS-threshold-based perspective." *IEEE J. Sel. Areas Commun.*, vol. 34, no. 1, pp. 163–175, 2016.

[95] W. Song, Y. Zhao, and W. Zhuang, "Stable device pairing for collaborative data dissemination with device-to-device communications," *IEEE Internet of Things J.*, vol. 5, no. 2, pp. 1251–1264, 2018.

[96] Z. Zhou, K. Ota, M. Dong, and C. Xu, "Energy-efficient matching for resource allocation in D2D enabled cellular networks," *IEEE Trans. Veh. Technol.*, vol. 66, no. 6, pp. 5256–5268, 2017.

[97] M. Ji, G. Caire, and A. F. Molisch, "The throughput-outage tradeoff of wireless one-hop caching networks," *IEEE Trans. Inf. Theory*, vol. 61, no. 12, pp. 6833–6859, 2015.

[98] R. Wang, J. Zhang, S. Song, and K. B. Letaief, "Mobility-aware caching in D2D networks," *IEEE Trans. Wireless Commun.*, vol. 16, no. 8, pp. 5001–5015, 2017.

[99] N. Zhao, X. Liu, Y. Chen, S. Zhang, Z. Li, B. Chen, and M. S. Alouini, "Caching D2D connections in small-cell networks," *IEEE Trans. Veh. Technol.*, vol. 67, no. 10, pp. 12 326–12 338, 2018.

[100] Z. Chen, J. Lee, T. Q. Quek, and M. Kountouris, "Cooperative caching and transmission design in cluster-centric small cell networks," *IEEE Trans. Wireless Commun.*, vol. 16, no. 5, pp. 3401–3415, 2017.

[101] S. Zhang, P. He, K. Suto, P. Yang, L. Zhao, and X. Shen, "Cooperative edge caching in user-centric clustered mobile networks," *IEEE Trans. Mobile Comput.*, vol. 17, no. 8, pp. 1791–1805, 2018.

[102] S. Zhang, N. Zhang, P. Yang, and X. Shen, "Cost-effective cache deployment in mobile heterogeneous networks," *IEEE Trans. Veh. Technol.*, vol. 66, no. 12, pp. 11 264–11 276, 2017.

[103] J. Xu, K. Ota, and M. Dong, "Saving energy on the edge: In-memory caching for multi-tier heterogeneous networks," *IEEE Commun. Mag.*, vol. 56, no. 5, pp. 102–107, 2018.

[104] X. Zhao, P. Yuan, H. Li, and S. Tang, "Collaborative edge caching in context-aware device-to-device networks," *IEEE Trans. Veh. Technol.*, vol. 67, no. 10, pp. 9583–9596, 2018.

[105] W. Song and W. Zhuang, "Packet assignment under resource constraints with D2D communications," *IEEE Network*, vol. 30, no. 5, pp. 54–60, 2016.

[106] O. Semiari, W. Saad, M. Bennis, and B. Maham, "Caching meets millimeter wave communications for enhanced mobility management in 5G networks," *IEEE Trans. Wireless Commun.*, vol. 17, no. 2, pp. 779–793, 2018.

[107] M. Ji, G. Caire, and A. F. Molisch, "Wireless device-to-device caching networks: Basic principles and system performance," *IEEE J. Sel. Areas Commun.*, vol. 34, no. 1, pp. 176–189, 2016.

[108] N. Giatsoglou, K. Ntontin, E. Kartsakli, A. Antonopoulos, and C. Verikoukis, "D2D-aware device caching in mmwave-cellular networks," *IEEE J. Sel. Areas Commun.*, vol. 35, no. 9, pp. 2025–2037, 2017.

[109] Y. Zhong, T. Q. Quek, and X. Ge, "Heterogeneous cellular networks with spatio-temporal traffic: Delay analysis and scheduling," *IEEE J. Sel. Areas Commun.*, vol. 35, no. 6, pp. 1373–1386, 2017.

[110] S. Singh, R. Mudumbai, and U. Madhow, "Interference analysis for highly directional 60-GHz mesh networks: The case for rethinking medium access control," *IEEE/ACM Trans. Netw.*, vol. 19, no. 5, pp. 1513–1527, 2011.

[111] G. R. MacCartney and T. S. Rappaport, "Rural macrocell path loss models for millimeter wave wireless communications," *IEEE J. Sel. Areas Commun.*, vol. 35, no. 7, pp. 1663–1677, 2017.

[112] S. M. Yu and S. L. Kim, "Downlink capacity and base station density in cellular networks," in *Proc. IEEE WiOpt*, 2013, pp. 119–124.

[113] M. Haenggi, J. G. Andrews, F. Baccelli, O. Dousse, and M. Franceschetti, "Stochastic geometry and random graphs for the analysis and design of wireless networks," *IEEE J. Sel. Areas Commun.*, vol. 27, no. 7, pp. 1029–1046, 2009.

[114] S. Srinivasa and M. Haenggi, "Distance distributions in finite uniformly random networks: Theory and applications," *IEEE Trans. Veh. Technol.*, vol. 59, no. 2, pp. 940–949, 2010.

List of Publications

[1]. W. Wu, N. Cheng, N. Zhang, P. Yang, W. Zhuang, and X. Shen, "Fast mmwave beam alignment via correlated bandit learning," *IEEE Trans. Wireless Commun.*, under revision.

[2]. W. Wu, N. Zhang, N. Cheng, Y. Tang, K. Aldubaikhy, and X. Shen, "Beef up mmWave dense cellular networks with D2D-assisted cooperative edge caching," *IEEE Trans. Veh. Technol.*, to appear.

[3]. W. Wu, N. Cheng, N. Zhang, P. Yang, and X. Shen, "Performance analysis and enhancement of 802.11ad MAC for mmWave beamforming training," manuscript.

[4]. W. Wu, Q. Shen, M. Wang, and X. Shen, "Performance analysis of IEEE 802.11.ad downlink hybrid beamforming," in *Proc. IEEE ICC*, 2017.

[5]. W. Wu, Q. Shen, K. Aldubaikhy, N. Cheng, N. Zhang and X. Shen, "Enhance the edge with beamforming: Performance analysis of beamforming-enabled WLAN," in *Proc. IEEE WiOpt*, 2018.